

8-10-2005

New Ruddlesden-Popper Perovskites Obtained by Topochemical Methods

Doinita Neiner
University of New Orleans

Follow this and additional works at: <https://scholarworks.uno.edu/td>

Recommended Citation

Neiner, Doinita, "New Ruddlesden-Popper Perovskites Obtained by Topochemical Methods" (2005).
University of New Orleans Theses and Dissertations. 306.
<https://scholarworks.uno.edu/td/306>

This Dissertation is protected by copyright and/or related rights. It has been brought to you by ScholarWorks@UNO with permission from the rights-holder(s). You are free to use this Dissertation in any way that is permitted by the copyright and related rights legislation that applies to your use. For other uses you need to obtain permission from the rights-holder(s) directly, unless additional rights are indicated by a Creative Commons license in the record and/or on the work itself.

This Dissertation has been accepted for inclusion in University of New Orleans Theses and Dissertations by an authorized administrator of ScholarWorks@UNO. For more information, please contact scholarworks@uno.edu.

NEW RUDDLESDEN-POPPER PEROVSKITES OBTAINED BY
TOPOCHEMICAL METHODS

Submitted to the Graduate Faculty of the
University of New Orleans
in the partial fulfillment of the
requirements for the degree of

Doctor of Philosophy
in
The Department of Chemistry

by
Doinita Neiner

B.S., University of Bucharest, 1997
M.S., University of Bucharest, 1998

August 2005

Acknowledgments

I would like to thank my advisor Professor John B. Wiley for his support and patience and for providing everything that made this research possible. He was always willing to hear my questions and problems and offer constantly pertinent answers or alternatives. Dr. Wiley allowed me to choose my own path and imparted the guidance for preventing me from going in circles. I am very much indebted to Dr. Wiley for his help and assistance in the preparation of this manuscript. He is the best advisor one can hope for and I cannot thank him enough for it.

I would also like to thank my committee members: Edwin Stevens, Scott Whittenburg, Steve Rick and Jiye Fang. Chronologically speaking, I first need to acknowledge Professor Scott Whittenburg for his help with the band structure calculation programs. Without his help, compiling these programs (LMTO and YAEHMOP) under Linux would have been impossible for me. He was also very willing to answer my questions during the preparation of my literature seminar.

I am grateful to Professor Jinke Tang for his time, valuable discussions on Solid-State Physics and for the occasional use of his XRD.

I am greatly indebted to Professor Ray Sweany for his help with IR/RAMAN/UV-VIS and Reflectance measurements. He always took time to listen to my questions and provide me with valuable information and hints.

I am very grateful to the Advanced Materials Research Institute and their very helpful personnel. I had numerous discussions on physical property measurements and data interpretation with Dr. Vladimir Golub and especially with Professor Leonard Spinu.

In addition, Professor Charles O'Connor helped me understand the concept of a "spin glass" and the type of measurements suitable to provide evidence of such a state.

My thanks go to Professor Matt Tarr, for his help with the ICP measurements. Along, the same lines, I need to thank one of my very best friends, Gabriela Blagoi, for initialization in ICP, standardization and data interpretation.

I do not think that there is anybody in the Chemistry Dept. that I do not owe a thank you.

I would like to express my gratitude to all of my group members: Dr. Tapas Mandal, Dr. Liliana Viciu, Xiao Zhang, Elisha Josepha, for motivating me and sharing their experience with me.

Finally yet importantly, I need to thank my parents for their continual moral and financial support that got me where I am now.

I also need to thank my "Romanian gang" along with what used to be "The French Connection", among which I need to mention Maria, Coco, Gabriela, Liliana, Mihai, Ela, Fred, Celine and Sebastian. I could not have done all of this without them being here.

At the end, I would like to thank "the Baby" (Patrick Nichols) for his patience and continual support. Whenever, I wanted to quit, he was always there encouraging me and loving me, without me even noticing that.

Table of Contents

List of Tables	viii
List of Figures	ix
Abstract	xiii
Chapter 1 Introduction and Background	1
1.1 Overview	1
1.2 Perovskites and Layered Perovskites	3
1.3 Solid-state Synthetic Methods	6
1.4 Elemental Analysis: Energy Dispersive Spectrometry and Inductively Coupled Plasma	8
1.5 Crystal Structure and Rietveld Refinement	10
1.6 Magnetic Properties	22
1.7 Heat Capacity and ac/dc Magnetic Susceptibility Methods	28
1.8 Electronically Driven Effects in Layered Perovskites. Second Order Jahn Teller Effect	35
1.9 Electronic Band Structure Calculations	35
1.10 References	39
Chapter 2 Synthesis and Characterization of the New Layered Perovskite, $\text{Na}_{0.1}(\text{VO})_{0.45}\text{LaTiO}_4$	43
2.1 Introduction	43
2.2 Experimental	44
2.2.1 Synthesis	44
2.2.2 Characterization	45
2.3 Results	47
2.3.1 Synthesis	47
2.3.2 Structure	47
2.3.3 Thermal Analysis	51
2.3.4 IR Data	52
2.3.5 EPR and Magnetic Data	52

2.4 Discussion	54
2.5 Conclusions	56
2.6 References	57
Chapter 3 The Structure and Properties of Mixed Valence Titanates, (Li _x VO)La ₂ Ti ₃ O ₁₀	59
3.1 Introduction	59
3.2 Experimental	60
3.2.1 Synthesis	60
3.2.2 Characterization	61
3.3 Results	62
3.3.1 Structure	62
3.3.2 EPR and Magnetic Measurements	67
3.3.3 Band Structure Calculations	69
3.4 Discussion	72
3.5 References	75
Chapter 4 Structural and Magnetic Investigation of Li _{0.3} Ni _{0.85} La ₂ Ti ₃ O ₁₀	77
4.1 Introduction	77
4.2 Experimental	78
4.2.1 Synthesis	78
4.2.2 Characterization	78
4.3 Results	80
4.3.1 Synthesis	80
4.3.2 Structure	80
4.3.3 Thermal Behavior	83
4.3.4 Band Structure Calculations and Transport Measurements	85
4.3.5 Magnetic Behavior and Heat Capacity	86
4.4 Discussion	91
4.5 References	95
Chapter 5 Lithium intercalation in Li _{0.3} Ni _{0.85} La ₂ Ti ₃ O ₁₀	96
5.1 Introduction	96
5.2 Experimental	97

5.2.1 Synthesis	97
5.2.2 Characterization	98
5.3 Results.....	98
5.3.1 Structure.....	98
5.3.2 DC and ac magnetic susceptibility measurements.....	99
5.3.3 Band Structure Calculations	107
5.4 Discussion.....	108
5.5 References.....	110
Chapter 6 Vanadyl insertion and lithium intercalation in the single layered RP	
Perovskite NaGdTiO ₄	111
6.1 Introduction.....	111
6.2 Experimental	112
6.2.1 Synthesis	112
6.2.2 Characterization	113
6.3 Results.....	114
6.3.1 Synthesis	114
6.3.2 Structure.....	115
6.3.3 Thermal Analysis.....	118
6.3.4 IR Data.....	118
6.3.5 Magnetic Data.....	119
6.4 Discussion.....	122
6.5 References.....	124
Chapter 7 Concluding Remarks	125
Appendix 1 The insertion of a transition metal layer between the perovskite	
blocks, Mn _{0.8} La ₂ Ti ₃ O ₁₀	128
A.1.1 Introduction.....	128
A.1.2 Experimental	129
A.1.2.1 Synthesis	129
A.1.2.2 Characterization	130
A.1.3 Results.....	130
A.1.3.1 Synthesis	130

A.1.3.2 Structure	132
A.1.3.3 Thermal behavior	132
A.1.3.4 Band structure and transport measurements	134
A.1.3.5 Magnetic behavior and heat capacity	136
A.1.4 Discussion	140
A.1.5 References	142
Appendix 2 Vanadyl insertion in the double and triple layered RP, $\text{K}_2\text{SrTa}_2\text{O}_7$ and $\text{Na}_2\text{Gd}_2\text{Ti}_2\text{MnO}_{10}$	143
A.2.1 Introduction	143
A.2.2 Experimental	144
A.2.2.1 Synthesis	144
A.2.2.2 Characterization	145
A.2.3 Results	145
A.2.3.1 Synthesis	145
A.2.3.2 Structure	147
A.2.3.3 IR Data	150
A.2.4 Discussion	151
A.2.5 References	152
Appendix 3 The insertion of a transition metal layer between the perovskite blocks, $\text{Fe}_{0.62}\text{La}_2\text{Ti}_3\text{O}_{10}$	153
A.3.1 Introduction	153
A.3.2 Experimental	153
A.3.2.1 Synthesis	153
A.3.2.2 Characterization	154
A.3.3 Results	155
A3.3.1 Synthesis	155
A.3.3.2 Structure	155
A.3.3.3 Magnetic behavior.....	157
A.3.4 Discussion	159
A.3.7 References	159
Vita.....	161

List of Tables

Table 1.1	Description of the 14 Bravais lattices among the seven crystal systems	12
Table 1.2	Interplanar spacings for the seven Bravais lattices	15
Table 1.3	The measurement and the expected magnetic behavior.....	34
Table 2.1	Refined unit cell parameters for NaLaTiO ₄ and Na _{0.1} (VO) _{0.45} LaTiO ₄	48
Table 2.2	Crystallographic data for Na _{0.1} (VO) _{0.45} LaTiO ₄	50
Table 2.3	Selected bond distances for Na _{0.1} (VO) _{0.45} LaTiO ₄	50
Table 3.1	Cell parameters based on a tetragonal symmetry for K ₂ La ₂ Ti ₃ O ₁₀ , (VO)La ₂ Ti ₃ O ₁₀ and the series (Li _x VO)La ₂ Ti ₃ O ₁₀	64
Table 3.2	Crystallographic data for (Li _{1.8} VO)La ₂ Ti ₃ O ₁₀	65
Table 3.3	Selected bond lengths in Å for (Li _{1.8} VO)La ₂ Ti ₃ O ₁₀	65
Table 3.5	Orbital parameters used in the YAEHMOP calculations.....	70
Table 4.1	The variation of the unit cell parameters and volume for all of the investigated materials.....	81
Table 4.2	Crystallographic data for Li _{0.3} Ni _{0.85} La ₂ Ti ₃ O ₁₀	82
Table 4.3	Bond lengths and bond angles for Li _{0.3} Ni _{0.85} La ₂ Ti ₃ O ₁₀	83
Table 5.1	Cell parameters based on a tetragonal symmetry for NiLa ₂ Ti ₃ O ₁₀ and (Li _x Ni)La ₂ Ti ₃ O ₁₀	100
Table 6.1	Refined unit cell parameters for NaGdTiO ₄ , Na _{0.05} (VO) _{0.48} GdTiO ₄ and Li _{1.056} Na _{0.05} (VO) _{0.48} GdTiO ₄	117
Table 6.2	Crystallographic data for Na _{0.05} (VO) _{0.48} GdTiO ₄	118
Table A.1.1	Unit cells for Li ₂ La ₂ Ti ₃ O ₁₀ , Na ₂ La ₂ Ti ₃ O ₁₀ and Mn _{0.8} La ₂ Ti ₃ O ₁₀	133
Table A.2.1	Unit cells for Na ₂ Gd ₂ Ti ₂ MnO ₁₀ and (VO)Gd ₂ Ti ₂ MnO ₁₀	149
Table A.2.2	EDAX for Na ₂ Gd ₂ Ti ₂ MnO ₁₀ +VOSO ₄	151
Table A.3.1	Refined unit cell parameters for Li ₂ La ₂ Ti ₃ O ₁₀ , Na ₂ La ₂ Ti ₃ O ₁₀ and Fe _{0.62} La ₂ Ti ₃ O ₁₀	156

List of Figures

Figure 1.1 The perovskite structure	3
Figure 1.2 Triple layered Ruddlesden-Popper perovskite structure, $A_2Ln_2M_3O_{10}$	4
Figure 1.3 The structure of the double layered Dion-Jacobson, $ALn_2M_2O_7$	5
Figure 1.4 Miller indices.....	11
Figure 1.5 Ewald sphere of reflection.....	14
Figure 1.6 Schematic representations for a paramagnetic, ferromagnetic and antiferromagnetic arrangements of spins	23
Figure 1.7 Susceptibility versus temperature data for an ideal Curie-Weiss paramagnet with a spin 1/2.....	24
Figure 1.8 The reverse susceptibility versus temperature for an ideal paramagnet $\theta = 0$, a ferromagnet $\theta > 0$ and an antiferromagnet $\theta < 0$	24
Figure 1.9 The magnetization versus temperature (left) and the reverse susceptibility versus temperature for a ferromagnet.	25
Figure 1.10 The magnetization versus field for a ferromagnet presenting a hysteresis loop	26
Figure 1.11 Susceptibility versus temperature and reciprocal susceptibility versus temperature for an antiferromagnet emphasizing the Néel temperature, the transition to the antiferromagnetic state.....	27
Figure 1.12 Examples of geometrically frustrated systems: a) the triangular lattice; b) unfrustrated square planar systems; c) frustrated square plaquette.	28
Figure 1.13 DOS for $Na_2La_2Ti_3O_{10}$	39
Figure 2.1 Powder X-ray diffraction patterns for (a) $NaLaTiO_4$ and (b) $Na_{0.1}(VO)_{0.45}LaTiO_4$	49
Figure 2.2 Rietveld refinement of $Na_{0.1}(VO)_{0.45}LaTiO_4$	49
Figure 2.3 The DSC curves for $(Na_{0.1}VO_{0.45})LaTiO_4$ in oxygen, and argon.	51
Figure 2.4 The DSC curve for $(Na_{0.1}VO_{0.45})LaTiO_4$ in hydrogen.	52
Figure 2.5 EPR spectra for $Na_{0.1}(VO)_{0.45}LaTiO_4$	53

Figure 2.6 Temperature dependence of magnetic susceptibility at 1000 Oe	54
Figure 3.1 X-ray powder pattern for: a) $K_2La_2Ti_3O_{10}$; b) $(VO)La_2Ti_3O_{10}$; c) $(Li_{0.83}VO)La_2Ti_3O_{10}$; d); e) $(Li_{1.4}VO)La_2Ti_3O_{10}$; f) $(Li_{1.8}VO)La_2Ti_3O_{10}$	63
Figure 3.2 Results of Rietveld refinements for the structure of $(Li_{1.8}VO)La_2Ti_3O_{10}$	64
Figure 3.3 The structure of $(Li_{1.8}VO)La_2Ti_3O_{10}$	66
Figure 3.4 IR spectra for: a) $K_2La_2Ti_3O_{10}$; b) $(VO)La_2Ti_3O_{10}$; c) $(Li_{1.8}VO)La_2Ti_3O_{10}$	67
Figure 3.5 X-band EPR spectra for $(VO)La_2Ti_3O_{10}$, $(Li_{1.4}VO)La_2Ti_3O_{10}$, $(Li_{1.8}VO)La_2Ti_3O_{10}$ and for comparison $VOSO_4$	68
Figure 3.6 Magnetic behavior for $(Li_xVO)La_2Ti_3O_{10}$	69
Figure 3.7 Band structure for $(Li_{1.8}VO)La_2Ti_3O_{10}$	71
Figure 3.8 The density of states (DOS) for $(Li_{1.8}VO)La_2Ti_3O_{10}$	71
Figure 4.1 Comparison of the X-ray powder patterns for a) $Li_2La_2Ti_3O_{10}$ b) $Li_{0.3}Ni_{0.85}La_2Ti_3O_{10}$	81
Figure 4.2 X-ray powder patterns for the Rietveld refinements of $Li_{0.3}Ni_{0.85}La_2Ti_3O_{10}$	82
Figure 4.3 DSC curves in argon and oxygen for $Li_{0.3}Ni_{0.85}La_2Ti_3O_{10}$	84
Figure 4.4 Comparison of the XRD for $Li_{0.3}Ni_{0.85}La_2Ti_3O_{10}$ in Ar	84
Figure 4.5 The band structures and the DOS for $Li_{0.3}Ni_{0.85}La_2Ti_3O_{10}$	85
Figure 4.6 The magnetic behavior of $Li_{0.3}Ni_{0.85}La_2Ti_3O_{10}$	87
Figure 4.7 Heat capacity for $Li_2La_2Ti_3O_{10}$ and $Li_{0.3}Ni_{0.85}La_2Ti_3O_{10}$	88
Figure 4.8 The magnetic contribution at the specific heat for $Li_{0.3}Ni_{0.85}La_2Ti_3O_{10}$	89
Figure 4.9 In field heat capacity data for $Li_{0.3}Ni_{0.85}La_2Ti_3O_{10}$	89
Figure 4.10 The ac susceptibility at 100, 1000 and 10,000 Hz for $Li_{0.3}Ni_{0.85}La_2Ti_3O_{10}$	90
Figure 4.11 In field ac susceptibility at 1000 and 10,000 Hz for $Li_{0.3}Ni_{0.85}La_2Ti_3O_{10}$	91
Figure 5.1 X-ray powder pattern for $Li_{0.3}Ni_{0.85}La_2Ti_3O_{10}$ and $(Li_xNi)La_2Ti_3O_{10}$	100
Figure 5.2 Susceptibility versus temperature in 100Oe field and hysteresis loop at 5 K for $Li_{1.1}NiLa_2Ti_3O_{10}$	101
Figure 5.3 The magnetic behavior of $Li_{2.01}NiLa_2Ti_3O_{10}$	102
Figure 5.4 The real part of the ac susceptibility versus temperature in 0 Oe field for $Li_{1.1}NiLa_2Ti_3O_{10}$	103
Figure 5.5 The imaginary part of the ac susceptibility versus temperature in 0 Oe field for $Li_{2.01}NiLa_2Ti_3O_{10}$	103

Figure 5.6 The real part of the ac susceptibility versus temperature in 0, 100 and 1000 Oe field for $\text{Li}_{1.1}\text{NiLa}_2\text{Ti}_3\text{O}_{10}$.	104
Figure 5.7 The imaginary part of the ac susceptibility versus temperature in 0, 100 and 1000 Oe field for $\text{Li}_{1.1}\text{NiLa}_2\text{Ti}_3\text{O}_{10}$.	104
Figure 5.8 The real part of the ac susceptibility versus temperature in 0 Oe dc field for $\text{Li}_{2.01}\text{NiLa}_2\text{Ti}_3\text{O}_{10}$.	105
Figure 5.9 The imaginary part of the ac susceptibility versus temperature in 0 Oe dc field for $\text{Li}_{2.01}\text{NiLa}_2\text{Ti}_3\text{O}_{10}$.	106
Figure 5.10 The real part of the ac susceptibility versus temperature in 100 Oe dc field for $\text{Li}_{2.01}\text{NiLa}_2\text{Ti}_3\text{O}_{10}$.	106
Figure 5.11 The DOS for $\text{Li}_{1.1}\text{NiLa}_2\text{Ti}_3\text{O}_{10}$ and $\text{Li}_{2.01}\text{NiLa}_2\text{Ti}_3\text{O}_{10}$.	107
Figure 6.1 Idealized crystal structure for $\text{Na}_{0.05}(\text{VO})_{0.48}\text{GdTiO}_4$.	115
Figure 6.2 XRD powder patterns for NaGdTiO_4 and $\text{Na}_{0.05}(\text{VO})_{0.48}\text{GdTiO}_4$.	116
Figure 6.3 Rietveld refinement of $\text{Na}_{0.05}(\text{VO})_{0.48}\text{GdTiO}_4$.	117
Figure 6.4 Calculated, observed powder patterns for $\text{Li}_{1.056}\text{Na}_{0.05}(\text{VO})_{0.48}\text{GdTiO}_4$ and for $\text{Na}_{0.05}(\text{VO})_{0.48}\text{GdTiO}_4$.	119
Figure 6.5 The magnetic behavior of $\text{Na}_{0.05}(\text{VO})_{0.48}\text{GdTiO}_4$.	120
Figure 6.6 The magnetic behavior of $\text{Li}_{1.056}\text{Na}_{0.05}(\text{VO})_{0.48}\text{GdTiO}_4$.	121
Figure 6.7 Hysteresis loop for $\text{Li}_{1.056}\text{Na}_{0.05}(\text{VO})_{0.48}\text{GdTiO}_4$ at 2 K.	122
Figure A.1.1 X-ray powder patterns for $\text{Mn}_{0.8}\text{La}_2\text{Ti}_3\text{O}_{10}$.	133
Figure A.1.2 Calculated versus observed powder patterns for $\text{Mn}_{0.8}\text{La}_2\text{Ti}_3\text{O}_{10}$.	134
Figure A.1.3 DSC curves in argon and oxygen for $\text{Mn}_{0.8}\text{La}_2\text{Ti}_3\text{O}_{10}$.	135
Figure A.1.4 X-ray powder patterns for $\text{Mn}_{0.8}\text{La}_2\text{Ti}_3\text{O}_{10}$ after TGA in oxygen.	135
Figure A.1.5 The band structures and the DOS for $\text{Mn}_{0.8}\text{La}_2\text{Ti}_3\text{O}_{10}$.	136
Figure A.1.6 Molar susceptibility versus temperature for $\text{Mn}_{0.8}\text{La}_2\text{Ti}_3\text{O}_{10}$.	137
Figure A.1.7 Hysteresis loop for $\text{Mn}_{0.8}\text{La}_2\text{Ti}_3\text{O}_{10}$.	137
Figure A.1.8 Heat capacity for $\text{Mn}_{0.8}\text{La}_2\text{Ti}_3\text{O}_{10}$.	138
Figure A.1.9 Heat capacity and entropy variation as a function of temperature for $\text{Mn}_{0.8}\text{La}_2\text{Ti}_3\text{O}_{10}$.	138
Figure A.1.10 Linear behavior of C/T versus T for $\text{Mn}_{0.8}\text{La}_2\text{Ti}_3\text{O}_{10}$.	139
Figure A.1.11 The <i>ac</i> susceptibility data for $\text{Mn}_{0.8}\text{La}_2\text{Ti}_3\text{O}_{10}$.	140

Figure A.2.1 The double and triple layered RP	148
Figure A.2.2 X-ray powder patterns for $\text{K}_2\text{SrTa}_2\text{O}_7$ and $(\text{VO})\text{SrTa}_2\text{O}_7$	149
Figure A.2.3 X-ray powder patterns for $\text{Na}_2\text{Gd}_2\text{Ti}_2\text{MnO}_{10}$ and $(\text{VO})\text{Gd}_2\text{Ti}_2\text{MnO}_{10}$	150
Figure A.3.1 X-ray powder patterns for $\text{Na}_2\text{La}_2\text{Ti}_3\text{O}_{10}$ and $\text{Fe}_{0.62}\text{La}_2\text{Ti}_3\text{O}_{10}$	156
Figure A.3.2 Calculated versus observed powder patterns for $\text{Fe}_{0.62}\text{La}_2\text{Ti}_3\text{O}_{10}$	157
Figure A.3.3 Molar susceptibility versus temperature for $\text{Fe}_{0.62}\text{La}_2\text{Ti}_3\text{O}_{10}$	158
Figure A.3.4 Hystereis loop for $\text{Fe}_{0.62}\text{La}_2\text{Ti}_3\text{O}_{10}$	158

Abstract

Topotactic routes have been used to produce new materials with tunable electronic and magnetic properties. The host materials were the single and triple layered Ruddlesden-Popper compounds, NaLnTiO_4 ($\text{Ln} = \text{La}$ and Gd) and $\text{A}_2\text{La}_2\text{Ti}_3\text{O}_{10}$ ($\text{A} = \text{Li}$ and K). These compounds consist of $[\text{LnTiO}_4]^-$ and $[\text{La}_2\text{Ti}_3\text{O}_{10}]^{2-}$, respectively, perovskite layers interleaved with two alkali metal ion strata. The topotactic routes used in this research were ion exchange and intercalation. Ion exchange was used to replace the cations in the interlayer space with a cationic unit: vanadyl or the transition metal ion, nickel. This ion exchange route opens the structure to further chemistry because each alkali metal ion is replaced by a divalent ion and a vacancy. In these vacancies other atoms can be inserted. Reductive intercalation with alkali metals is of special interest due to their propensity for forming mixed valence compounds. Mixed valency is usually correlated with semiconductive, metallic or superconductive behaviors, and unusual magnetic properties (CMR).

$\text{Na}_{0.1}(\text{VO})_{0.45}\text{LaTiO}_4$, $\text{Na}_{0.05}(\text{VO})_{0.48}\text{GdTiO}_4$ and $\text{Li}_{0.3}\text{Ni}_{0.85}\text{La}_2\text{Ti}_3\text{O}_{10}$ have been obtained by ion exchange reactions. Also, the reactivity of $\text{Na}_{0.05}(\text{VO})_{0.48}\text{GdTiO}_4$, $(\text{VO})\text{La}_2\text{Ti}_3\text{O}_{10}$ and $\text{Li}_{0.3}\text{Ni}_{0.85}\text{La}_2\text{Ti}_3\text{O}_{10}$ is probed by an intercalation reaction with $n\text{-BuLi}$. Lithium insertion between the perovskite blocks reduces the titanium in the perovskite sheets and produces new mixed valence titanates. Lithium intercalation in the vanadyl compounds, $\text{Na}_{0.05}(\text{VO})_{0.48}\text{GdTiO}_4$, as well as $(\text{VO})\text{La}_2\text{Ti}_3\text{O}_{10}$ gives rise to new magnetic properties. The crystal structures, thermal behavior, electronic and magnetic properties of these new compounds will be discussed.

Chapter 1

Introduction and Background

1.1. Overview

Layered oxides with perovskite related structures have the general formula $A_m[A'_{n-1}B_nO_{3n+1}]$, where $A'_{n-1}B_nO_{3n+1}$ is the perovskite strata, A is an interlayer cation usually an alkali metal, B is a transition metal and A' is an alkaline or rare earth metal. When $m = 2$ the phase is called a Ruddlesden-Popper layered perovskite. In the Ruddlesden-Popper series, $K_2La_2Ti_3O_{10}$ is a catalyst for the water splitting process, $La_{2-x}Ba_xCuO_4$ and Sr_2RuO_4 are superconductive, $Sr_4V_3O_{9.7}$ and $La_4Ni_3O_{10}$ are metallic and $La_{2-2x}Sr_{1+2x}Mn_2O_7$ is colossal magnetoresistive.^[1-3] Traditionally these materials are prepared by high temperature ceramic methods. In terms of chemical reactivity, it has been shown that the interlayer cations can be exchanged with other cations or cationic units by low temperature, topochemical reactions.^[4] Low temperatures ($T < 500\text{ }^\circ\text{C}$) offer the potential for making new compounds with targeted properties. Topochemical reactions are driven by the crystal structure rather than by the chemical nature of the reactants. In this manner, the basic crystal structure of the parent phase remains the same, except for the corresponding changes in the lattice parameters necessary to accommodate the new species. Topochemical methods include ion exchange, intercalation/deintercalation, exfoliation and dehydration/condensation reactions. These methods provide access to a wide variety of metastable phases that cannot be formed by traditional solid-state reactions.

This research was focused on such topotactic routes to produce new materials with tunable electronic and magnetic properties. In this work the host materials are the single, the double, and triple layered Ruddlesden-Popper compounds, $NaLnTiO_4$ ($Ln = La$ and Gd),

$\text{K}_2\text{SrTa}_2\text{O}_7$, $\text{A}_2\text{La}_2\text{Ti}_3\text{O}_{10}$ ($\text{A} = \text{Li}, \text{Na}, \text{K}$), and $\text{Na}_2\text{Gd}_2\text{Ti}_2\text{MnO}_{10}$. NaLnTiO_4 ($\text{Ln} = \text{La}$ and Gd) and $\text{A}_2\text{La}_2\text{Ti}_3\text{O}_{10}$ ($\text{A} = \text{Li}, \text{Na}, \text{K}$) consist of $[\text{Ln}_2\text{Ti}_3\text{O}_{10}]^{2-}$ perovskite layers interleaved with two alkali metal ion strata. $\text{K}_2\text{SrTa}_2\text{O}_7$ has $[\text{SrTa}_2\text{O}_7]^{2-}$ layers interleaved with two K ion sheets. The topotactic routes used in this research are ion exchange and intercalation. Ion exchange was used to replace the cations at the interlayer space with a cationic unit, vanadyl or with a divalent transition metal ion, such as nickel, manganese and iron. In addition, the ion exchange route opens the structure to further chemistry. When the monovalent alkali metals are replaced with divalent ions or cationic units, in order for the charge balance to be maintained, one divalent unit replaces two monovalent ions. Therefore, the interlayer space in the ion exchanged product has empty sites. On these empty sites, an alkali metal can be inserted. Intercalation of alkali metals is of special interest due to their propensity for forming mixed valence compounds. Mixed valency is usually correlated with semiconductive, metallic or superconductive behaviors, and unusual magnetic properties (e. g. CMR). Herein, will be presented the structural and physical characterization of $\text{Na}_{0.1}(\text{VO})_{0.45}\text{LaTiO}_4$, $\text{Na}_{0.05}(\text{VO})_{0.48}\text{GdTiO}_4$, $\text{Li}_{0.3}\text{Ni}_{0.85}\text{La}_2\text{Ti}_3\text{O}_{10}$, $\text{Mn}_{0.8}\text{La}_2\text{Ti}_3\text{O}_{10}$, and $\text{Fe}_{0.62}\text{La}_2\text{Ti}_3\text{O}_{10}$ obtained by ion exchange reactions. Also, the reactivity of $\text{Na}_{0.05}(\text{VO})_{0.48}\text{GdTiO}_4$, $(\text{VO})\text{La}_2\text{Ti}_3\text{O}_{10}$ and $\text{Li}_{0.3}\text{Ni}_{0.85}\text{La}_2\text{Ti}_3\text{O}_{10}$ is probed by an intercalation reaction with n-BuLi. Lithium insertion between the perovskite blocks reduces the titanium in the perovskite sheets and produces new mixed valence titanates. The magnetic and electronic properties of these materials are discussed in correlation with the amount of intercalated lithium, which is ultimately related to the $\text{Ti}^{4+}/\text{Ti}^{3+}$ ratio.

1.2. Perovskites and Layered Perovskites

The perovskite oxides of a general formula ABO_3 , where A is an alkali, alkaline transition metal or rare earth metal and B is usually a transition metal, represent one of the most important classes of solid-state materials. The perovskite structure is shown in Figure 1.1. It can be described as a three dimensional network of corner sharing BO_6 octahedra. In this geometry the A cations are at the body center of the cubic cell, surrounded by twelve oxygen anions. The significance of this class of materials arises from their compositional diversity. In addition, they have very interesting and varied electric, magnetic and optical properties.^[5]

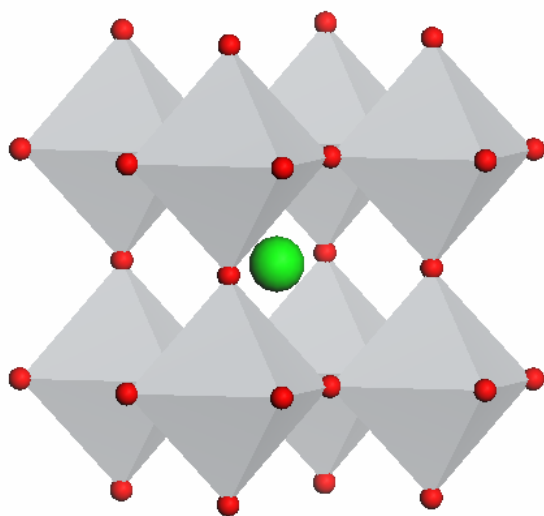


Figure 1.1 The perovskite structure. The octahedra are BO_6 units. The red atoms are oxygen and in the middle of the eight corner sharing octahedra, the A cation is represented in green.

Although the ideal perovskite is cubic, the majority of ABO_3 compounds exhibit distortions resulting from: a) rotation or tilting of the BO_6 distortion-free polyhedra; b) first and second order Jahn-Teller distortion of the BO_6 octahedra, reflecting mixing of molecular orbitals coupled or not with lone pair effects.^[5] This distortion changes the bond lengths for the A-O

and/or B-O connectivity, and causes the ideal perovskite symmetry to lower from cubic to tetragonal or orthorhombic.

These compounds constitute an active area of research, in the recent discovery of high temperature superconductivity in the layered perovskites, $\text{La}_{2-x}\text{BaCuO}_4$ and Sr_2RuO_4 (1986, 1994), followed by the colossal magneto-resistance effect in $\text{La}_{2-2x}\text{Sr}_{1+2x}\text{Mn}_2\text{O}_7$ (1993).^[1-3] Important examples of other classes of layered perovskites include the Dion-Jacobson series and Ruddlesden-Popper phases.^[6-8] These compounds are best thought of as intergrowth structures of perovskite strata interleaved with cationic units. The triple layered Ruddlesden-Popper oxide (Figure 1.2) and double layered Dion-Jacobson (Figure 1.3) compounds are represented below.

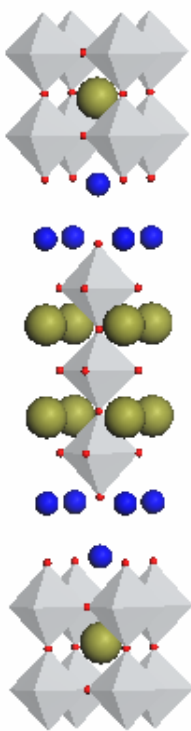


Figure 1.2 Idealized triple layered Ruddlesden-Popper perovskite structure, $\text{A}_2\text{Ln}_2\text{M}_3\text{O}_{10}$.

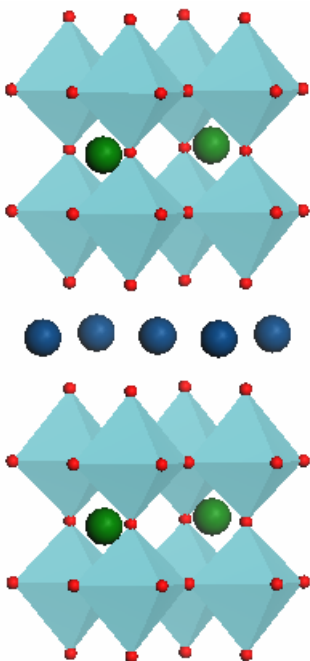


Figure 1.3 The structure of the double layered Dion-Jacobson, $\text{AlN}_2\text{M}_2\text{O}_7$.

Ruddlesden-Popper (RP) and Dion-Jacobson (DJ) oxides have the general formulas $\text{A}_2[\text{A}'_{n-1}\text{B}_n\text{O}_{3n+1}]$ and $\text{A}[\text{A}'_{n-1}\text{B}_n\text{O}_{3n+1}]$, where A can be an alkali metal, A' an alkaline or a rare earth metal and B a transition metal cation.^[7, 8] The basic difference between the two is that the RP oxides have a higher charge density as compared to the DJ series. The interest in these compounds has increased since the discovery that the interlayer space alkali cations can be replaced with other cations or cationic units while maintaining the layered perovskite structure. Such a reaction is governed by the crystal structure and is called topotactic. These routes allow the maintenance of the basic crystal structure of the parent phase and provide access to a wide variety of phases that cannot be formed by traditional solid-state reactions. Examples of topotactic reactions are ion exchange, reductive (oxidative) intercalation (deintercalation), condensation and exfoliation.^[9 - 14]

The main goal of this research was to extend the use of such soft chemistry methods to produce new compounds with tunable properties as a function of chemical composition. Another ambition of this exploration was to establish structure-properties relationships that would help in the rational design of a variety of compounds.

1.3. Solid State Synthetic Methods

Solid-state materials are traditionally synthesized using high temperature “heat and beat” solid-solid reactions, hydrothermal techniques or sol-gel methods.^[15] The oldest but still the most widely used synthetic method is to mix the powder reactants and fire them at high temperatures for long periods. A very good mixing is required in this case, because solid-solid reactions are diffusion limited. For instance, in the synthesis of MgAl_2O_4 , the precursors, MgO and Al_2O_3 , should be weighted in the appropriate amounts and then intimately grinded. The effect of grinding is to ensure a high surface area of contact between the reactants. Also, it is sometimes useful to use intermediate grindings to bring fresh surfaces of reactants into contact.^[15]

Some of the desired structural features of a material, such as a specific sequence of atoms, are very difficult to control thermodynamically. Soft chemistry offers an alternative for controlling these features at the kinetic level.^[16] In the RP and DJ series, the interlayer cations can easily be exchanged at low temperatures. This leads to the formation of new phases that can be either layered or three dimensionally bonded. The enormous number of new compounds synthesized has demonstrated the success of ion exchange reactions. Ion exchange reactions have lead to new metastable triple layered RP phases, such as $\text{MLa}_2\text{Ti}_3\text{O}_{10}$ ($\text{M} = \text{VO}, \text{Ca}, \text{Li}, \text{Co}, \text{Cu}, \text{Zn}$) and $\text{H}_2\text{La}_2\text{Ti}_3\text{O}_{10}$.^[17-21] In our group, using a two-step low temperature route (ion exchange

and then reductive intercalation), mixed valence RP compounds with semiconducting behavior such as $\text{Na}_{1-x+y}\text{Ca}_{x/2}\text{LaTiO}_4$ and $\text{Na}_{2-x+y}\text{Ca}_{x/2}\text{La}_2\text{Ti}_3\text{O}_{10}$ have been obtained.^[22,23]

In the case of RP and DJ compounds, usually the lithium compound cannot be synthesized by direct methods. It can only be obtained by a molten state reaction between one of the bigger alkali metal homologues and lithium nitrate in a very big molar excess.^[19] Similarly, by using eutectic mixtures of KCl and MCl ($M = \text{Co}, \text{Cu}, \text{Zn}$), new members of the single and triple RP series $\text{M}_{0.5}\text{LaTiO}_4$ and $\text{MLa}_2\text{Ti}_3\text{O}_{10}$ have been prepared.^[20,24] Another approach is an aqueous solution reaction. This method allowed the synthesis of many compounds such as the vanadyl analogue, $(\text{VO})\text{La}_2\text{Ti}_3\text{O}_{10}$, the calcium compound $\text{CaLa}_2\text{Ti}_3\text{O}_{10}$, and the hydrogen forms of the triple and the double RP perovskites, $\text{H}_2\text{La}_2\text{Ti}_3\text{O}_{10}$ or $\text{H}_2\text{SrTa}_2\text{O}_7$.^[17,18,21,25] These hydrogen forms can condensate to the defective perovskite phases $\text{La}_2\text{Ti}_3\text{O}_9$ and SrTa_2O_6 by eliminating one water molecule.^[21,25]

A very elegant way to synthesize new materials is to introduce in a structure new atoms into vacant sites (intercalation) or to selectively remove certain atoms (deintercalation) while keeping the same basic structure.^[15] Most of these intercalation/deintercalation reactions involve the addition or removal of ions, and therefore, in order to maintain the charge balance, electrons must be added or removed. The importance of intercalation reactions is represented by lithium intercalation in anatase (TiO_2). This compound changes from an insulator into a superconductor upon lithium intercalation.^[15] In the RP oxybromide, $\text{Sr}_2\text{CuO}_2\text{Br}_2$, lithium intercalation produced a superconductor.^[24] Graphite is probably the classic example where its structure is very open to intercalation chemistry. Graphite can intercalate alkali cations, halide anions, ammonia, amines, oxysalts and metal halides.^[15]

RP oxides can be transformed by ion exchange such that their structure opens up to cationic or anionic intercalation chemistry. Using a two-step low temperature route (divalent ion exchange and then reductive intercalation), mixed valence RP compounds, with semiconducting behavior, such as $\text{Na}_{1-x+y}\text{Ca}_{x/2}\text{LaTiO}_4$ and $\text{Na}_{2-x+y}\text{Ca}_{x/2}\text{La}_2\text{Ti}_3\text{O}_{10}$ can be obtained.^[22,23] The essence of this method is the formation of a volatile compound that can migrate and eventually absorb itself into the stationary phase. The volatile compound can be an alkali metal, an azide or a hydride of an alkali metal, a halogen, and oxygen. In the case of the alkali metal, the reaction is performed in a sealed tube at 100-200 °C, having the powder at one end of the tube and the metal at the other end. The reaction works best if a temperature gradient exists in the tube, such that the volatilization and the intercalation of the alkali are facilitated.^[15] Another approach is to use a reducing organometallic combination, such as n-BuLi in an inert atmosphere. In this case stirring and heating can help the reaction proceed faster.^[15] Lithium insertion can also be carried out electrochemically. This method has the advantage of a very good control of lithium content.^[15,24]

1.4. Elemental Analysis: Energy Dispersive Spectrometry and Inductively Coupled Plasma

In examining a solid, it is worthwhile to look at the powder at higher magnification. For such purposes, one can use an optical microscope (down to a few micrometers), a SEM (scanning electron microscope, for 10^{-2} to 10^2 μm), a HREM (high-resolution electron microscope, for atomic scale information) or a TEM (transmission electron microscopy). The basic principle for microscopy is to have an electronic beam emitted from a tungsten filament and accelerated through a high voltage (50-200 kV) hit the sample. When this happens, X-rays

and secondary electrons are emitted. The first are used in elemental analysis and the second build an image of the sample surface.^[15] SEM is a very powerful technique in giving valuable information about particle size and morphology, sample texture and even crystal defects. Some SEM and TEM instruments also provide an elemental analysis of the sample. SEM coupled with EDS (energy dispersive spectrometry), allows not only a visual inspection of the sample but also an elemental analysis of it. The elements present in the sample can be semiquantitatively or even quantitatively (if standards are used) determined. When the sample is placed under the microscope and bombarded with high-energy electrons, they generate the X-rays. These are characteristic emission lines for the elements present. By scanning their dispersive energy, one can identify and quantify elements, starting with sodium and heavier elements.

For lighter elements, other techniques are available, such as Auger spectroscopy, electron energy loss spectroscopy (EELS) or inductively coupled plasma emission spectroscopy (ICP).^[15] In this study ICP and SEM/EDS were used. The analytical principle used in the ICP systems is optical emission spectroscopy. A liquid is nebulized and then vaporized in the Argon plasma. The atoms and ions contained in the plasma vapor are excited into a state of radiated light (photon) emission. The radiation emitted can be passed to the spectrometer optics, where it is dispersed into its spectral components. From the specific wavelengths emitted by each element, the most suitable line for the application is measured by means of a charge coupled device (CCD). The radiation intensity, which is proportional to the concentration of the element in the sample, is recalculated internally from a stored set of calibration curves and can be shown directly as percent or measured concentration. The principal accomplishment of the ICP spectroscopy is that it makes possible the analysis of all of the elements and even combinations

of elements. The main drawback, especially for solid-state chemistry, is that sometimes the samples are only partially soluble in the most common solvents.

1.5. Crystal Structure and Rietveld Refinement

The most important step in characterizing a new solid-state material is to determine its crystal structure. The arrangement of atoms in the configuration that minimizes the electrostatic interaction or maximizes the symmetry is the crystal structure.^[26,27] The simplest repeating unit that shows the whole symmetry of a crystal is a unit cell. The determination of the unit cell involves the unit cell dimensions and the fractional coordinates of the atoms present in the crystal. The various types of three dimensional unit cells are named after August Bravais (1811-1863) a French crystallographer who first described them mathematically.^[26,27] A three dimensional Bravais lattice consists of all points with position vectors, R , of the form:

$$R = n_1 a_1 + n_2 a_2 + n_3 a_3 \quad (1)$$

If the unit cell has one equivalent point at each corner, then it is called primitive, P. If there is an additional point in the middle of each cell, then a body centered lattice is formed, I. When the cell has equivalent points at each corner and in the middle of each face, the cell is called face centered, F. There are seven crystal systems, which make up fourteen Bravais lattices and they are listed in Table 1.1. Translating a point through the vectors of any Bravais lattice, 230 different symmetry groups can be obtained.^[26-28] The points in a Bravais lattice that are the closest to a given point are called the nearest neighbors. Because of the periodicity of the lattice, each point has the same number of neighbors. A volume of space that, when translated through all of the vectors in a Bravais lattice, fills the space without overlapping or leaving voids, is

called the primitive cell of the lattice. A conventional cell can also be chosen, though they are usually bigger than the unit cell. Another type of primitive cell is the Wigner-Seitz cell; this has the full symmetry of the Bravais lattice.^[26,27] To describe various directions and distances, it is necessary to imagine a set of parallel planes identified by integers called Miller indices. Figure 1.4 presents an example of a unit cell and the face (111) that cuts all three axes at 1 unit length has the parameters $1a$, $1b$, $1c$. Inverting these, results in $1/1$, $1/1$, $1/1$ to give the Miller index (111). The square face that cuts the positive a axis, has the parameters $1a$, ∞b , ∞c . Inverting these becomes $1/1$, $1/\infty$, $1/\infty$ to give the Miller Index (100). The face on the back of the crystal that cuts the negative a axis has the parameters $-1a$, ∞b , ∞c . Therefore, its Miller index is ($\bar{1}$ 11). A negative intercept is indicated by putting a minus sign above the index. Thus, the other 4 faces seen on this crystal would have the Miller Indices (001), ($00\bar{1}$), (010), and ($0\bar{1}0$).^[26,27]

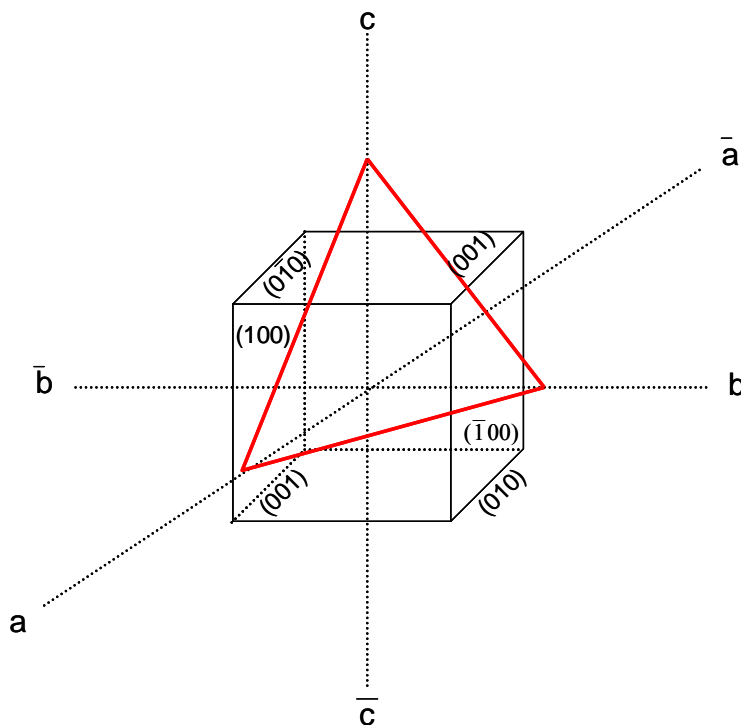


Figure 1.4 Miller indices.

Table 1.1 Description of the 14 Bravais lattices among the seven crystal systems.

Crystal System	No.	Unit Cell	Coordinate Description
Triclinic	1	Primitive	$\mathbf{a} \neq \mathbf{b} \neq \mathbf{c}$ $\alpha \neq \beta \neq \gamma$
Monoclinic	2	Primitive	$\mathbf{a} \neq \mathbf{b} \neq \mathbf{c}$
	3	Body Centered	$\alpha = \beta = 90^\circ \neq \gamma$
Orthorhombic	4	Primitive	
	5	Base Centered	$\mathbf{a} \neq \mathbf{b} \neq \mathbf{c}$
	6	Body Centered	$\alpha = \beta = \gamma = 90^\circ$
	7	Face Centered	
Tetragonal	8	Primitive	$\mathbf{a} = \mathbf{b} \neq \mathbf{c}$
	9	Body Centered	$\alpha = \beta = \gamma = 90^\circ$
Trigonal	10	Primitive	$\mathbf{a} = \mathbf{b} = \mathbf{c}$ $\alpha = \beta = \gamma < 120^\circ, \neq 90^\circ$
Hexagonal	11	Primitive	$\mathbf{a} = \mathbf{b} \neq \mathbf{c}$ $\alpha = \beta = 90^\circ, \gamma = 120^\circ$
Cubic	12	Primitive	
	13	Body Centered	$\mathbf{a} = \mathbf{b} \neq \mathbf{c}$
	14	Face Centered	$\alpha = \beta = \gamma = 90^\circ$

There are, at this time, two techniques capable of providing phase recognition and these are X-rays and neutron diffraction data. X-rays are scattered by electrons that surround the atomic nuclei and neutrons by the atomic nuclei. The scattering power for the X-rays is proportional to the electron density in the sample. The heavier the element, the better it will diffract. X-rays are short wavelength (comparable with atomic distances), high-energy electromagnetic radiation. They are produced when matter is irradiated with a beam of high energy electrons or photons. A 40 kV electron beam from a heated tungsten filament hits a copper anode target. The incoming beam ionizes the Cu 1s (K shell) electrons. An electron from

2p or 3p falls on the vacant 1s orbital, and the energy released is the X-ray radiation.^[15,26,27] If the transition is from 2p to 1s, then Cu K_α line is emitted. If the electron drops from 3p in 1s then Cu K_β is emitted. K_α transitions occur more frequently than K_β and they are more intense. The wavelength of the emitted X-rays is related to the atomic number, Z , of the metal target (Cu) by Moseley's law.

$$\lambda^{-1/2} = C(Z - \sigma) \quad (2)$$

When X-rays irradiate a periodic array of atoms, diffraction occurs in a multitude of directions. The scattered waves propagate in space until they meet each other. This interference can be constructive at some angles or destructive at other angles depending on the distance between the scatterers and the wavelength of the radiation. P. Ewald developed the most pictorial method of describing the diffraction phenomenon.^[26] Ewald's method is based purely on geometrically considerations and the reciprocal space. Ewald sphere is depicted in Figure 1.5. Instead of using the d_{hkl} vectors, the correspondent vectors in the reciprocal space, d_{hkl}^* , should be used, with $d_{hkl}^* = 1 / d_{hkl}$.^[26] Considering a cross section around a real crystal through an imaginary sphere (Figure 1.5) of a radius $1/\lambda$, where λ is the wavelength of the X-ray radiation. The reciprocal lattice of this crystal is tangent to the sphere at the point where the X-ray beam enters, from the left, passes through the crystal, and exists on the right. Rotating the sample (in the middle) in the beam, one plane of atoms will be brought in the contact with the sphere.

$$CO = \frac{1}{\lambda} \text{ and } OA = \frac{d_{hkl}^*}{2} \text{ therefore } \sin \theta = \frac{OA}{CO} = \frac{d_{hkl}^*/2}{1/\lambda} \text{ or rearranged } \lambda = 2d \sin \theta \quad (3)$$

Many materials in nature are found in a polycrystalline form or a powder. A powder consists of a large number of tiny crystallites in all possible orientations. When a powder is placed in an X-ray beam, diffraction from each plane will occur at its characteristic θ . If the

experimental angle θ , is changed to 2θ , all of the possible peaks arising from differently oriented crystallites will be produced. Each crystallite has its own reciprocal space with a specific orientation in the X-ray beam. The diffracted intensity will originate at the crystallites in the center of the sphere and project outward producing a cone of diffracted intensity. These cones will intersect a film placed normal to the beam and produce a set of concentric circles called Debye rings each associated with a single (hkl) .^[26-29]

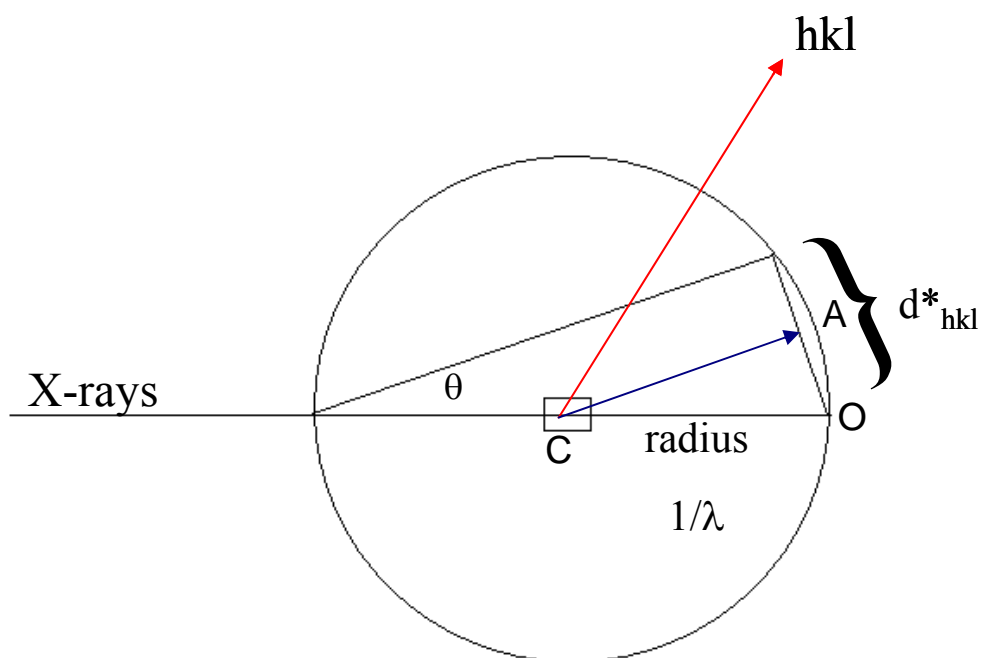


Figure 1.5 Ewald sphere of reflection.

These planes are characterized by certain interplanar distances d_{hkl} , which are a function of the size and the shape of the unit cell. The interplanar spacings for the seven Bravais lattices are given in Table 1.2. Other factors that influence a powder pattern are the atomic numbers and the positions of the atoms in the cell.^[27]

Therefore, a powder pattern has two characteristic features, the d spacings of the lines, which are characteristics of the unit cell, and their intensities, which are characteristic for the arrangement of atoms in a specific unit cell.

Table 1.2 Interplanar spacings for the seven Bravais lattices.

Unit cell	Interplanar spacing
Cubic	$1/d^2 = (h^2 + k^2 + l^2) / a^2$
Tetragonal	$1/d^2 = [(h^2 + k^2) / a^2] + l^2 / c^2$
Orthorhombic	$1/d^2 = (h^2 / a^2) + (k^2 / b^2) + (l^2 / c^2)$
Hexagonal	$1/d^2 = 4/3[(h^2 + hk + k^2) / a^2] + l^2 / c^2$
Monoclinic	$1/d^2 = (1 / \sin^2 \beta)[(h^2 / a^2) + (k^2 \sin^2 \beta / b^2) + (l^2 / c^2) - (2hl \cos \beta / ac)]$
Triclinic	$1/d^2 = 1/V^2[h^2 b^2 c^2 \sin^2 \alpha + k^2 a^2 c^2 \sin^2 \beta + l^2 a^2 b^2 \sin^2 \gamma + 2hkabc^2 (\cos \alpha \cos \beta - \cos \gamma) + 2kla^2 bc (\cos \beta \cos \gamma - \cos \alpha) + 2hlab^2 c (\cos \alpha \cos \gamma - \cos \beta)]$

The intensity of a diffraction peak depends on a number of independent phenomena such as electron and atomic scattering, interference effects, anomalous scattering and thermal motion of atoms. The intensity scattered by an electron is given by:

$$I = \frac{I_0}{r^2} \left[\frac{e^2}{m_e c^2} \right]^2 \frac{1 + \cos^2(2\theta)}{2} \quad (4)$$

where I_0 is the intensity of the incident beam; e is the electron charge; m_e is the mass of the electron; c is the light speed and r is the distance from the scattering electron to the detector.

Because the atomic dimensions are of the same order of magnitude with the wavelength of the radiation used in diffraction experiments, interferences occur. For a powder, the phase shift makes the interference partially destructive. To describe this phenomenon a quantity f_0 ,

called the atomic scattering factor, is used. At $\theta = 0$, f_0 will be the number of electrons surrounding any atom. Because the phase difference depends on the wavelength and the angle of view, f_0 will be a function of $(\sin\theta)/\lambda$. Another correction is anomalous scattering.^[26,27] This needs to be employed only when the wavelength of the scattered X-ray is near an absorption edge. Anomalous scattering is caused by a lag between the emitted photon (coming from a transition to a state with energy near the absorption edge) and a normal scattered photon.^[27] This produces an interference effect that appears as an anomalous change in the scattered intensity. The next correction involves an atom vibrating around a lattice site.^[27] This gives rise to large interference effects because the atom will be virtually larger. This is described by B, the Debye-Waller temperature factor, where $B = 8\pi^2 U^2$, and U^2 is the mean square amplitude for the vibration of the atom. The effect of the atom vibration on the atomic structure factor f is:

$$f = f_0 \exp\left(\frac{-B \sin^2 \theta}{\lambda^2}\right) \quad (5)$$

If the surroundings of the atom have cubic symmetry, B will be isotropic. Most atoms in solids have special directions along which they can vibrate, so B in this case will be anisotropic. The net scattering from all of the atoms in the unit cell is the vector sum of the individual atomic scattering vectors, f_j , and is called the structure factor, F_{hkl} .

$$F_{hkl} = \sum_{j=1}^m f_j \exp[2\pi i(hx_j + ky_j + lz_j)] \quad (6)$$

where m is the number of atoms in the unit cell. The observed intensity for any Bragg reflection is $|F_{hkl}|^2$. Translational symmetry generates phase relationships between the scatterings coming from symmetry related atoms, causing certain classes of reflections to have exactly zero intensity. These impose systematic extinction conditions on the h, k, l indices that are

characteristic for a certain Bravais lattice. Before calculating the diffraction pattern, one will need to correct for the multiplicity of the Bragg planes, the Lorentz factor, extinction, absorption and monochromator polarization.^[26-28]

In a structure determination, an important step is the data collection. In general, one needs a minimum of 50 lines for a complete identification and as many as possible at low angles. A scan with an instrument that uses Cu K α radiation should begin about $2\theta = 5^\circ$ and end above $2\theta = 80^\circ$. For well-crystallized materials, the step size is $2\theta = 0.02^\circ$. Once the data collection is finished, a smoothing and a background subtraction may be necessary prior to the indexing of the diffraction pattern. Once the unit cell has been found, the associated space group must be determined, starting from the most symmetric with a continual reduction in symmetry until a good agreement is reached. Only after having a good unit cell and the right space group, one can proceed to the actual determination of the structure. The final and probably the most time consuming step is the completion of the structure determination, which is the Rietveld refinement.^[26] The Rietveld method introduced in the late 60's, is a least squares refinement that minimizes the difference between an observed and a calculated profile. Originally designed for neutron data, this method is widely used today in both synchrotron and laboratory X-ray data.^[26] Though the Rietveld method is a very powerful tool in refining crystal structures, it requires a good starting model in order to converge successfully, and does not constitute a crystal structure determination method by itself.

It is sometimes useful to treat the profile of the diffracted peaks separate from the structure. This is achieved by employing a Le Bail algorithm. If the structure is unknown, then no calculated structure factors can be generated and the simplest thing to assume is that all of the integrated intensities are initially equal. The Le Bail method is a recursive version of the Rietveld

algorithm that allows calculating iteratively peak areas in the absence of a structural model. The method is very useful in refining the initial values for profile functions and background that are then used in a Rietveld refinement in the presence of a structural model. For N-peak overlap, the iteration can be written mathematically as: ^[27]

$$A_m^{r+1}(obs) = \sum_i \frac{A_m^r(obs) \times q_m(i)}{\left(\sum_{n=1}^N A_n^{(r)}(obs) \times q_n(i) \right)} (obs(i) - back(i)) \quad (7)$$

where $A_n^{(r=1)}(obs) = 1$ and $n = \overline{1, N}$. The popularity of Le Bail method has increased since it has been incorporated in Rietveld refinement codes such as GSAS and Fullprof.

The quantity minimized in a Rietveld refinement is the weighted difference between the observed $y(obs)$ and the calculated $y(calc)$ diffraction patterns, called the Rietveld residual, S_y . ^[28]

$$S_y = \sum_i w_i (y_i(obs) - y_i(calc)) \quad (8)$$

Many reflections contribute to the observed intensity, $y_i(obs)$ at any point in the diffraction pattern. ^[29] The calculated intensities $y_i(calc)$ are computed from $|F_K|^2$ values determined from the structural model by summing the contributions from neighboring reflections plus the background:

$$y_i(calc) = s \sum_K L_K [F_K]^2 \phi(2\theta_i - 2\theta_K) P_K A + y_i(background) \quad (9)$$

where s = scale factor; K = Miller indices h, k, l ; L_K = contains Lorentz polarization and multiplicity factors; ϕ = the reflection profile function; P_K = preferred orientation; A = absorption factor; F_K = the structure factor for the K th reflection; $y_i(background)$ = the background intensity at the i th step.

The least squares minimization leads to a set of equations involving derivatives of the calculated intensities with respect to some adjustable parameters x_j, x_k .

$$M_{jk} = -\sum_i 2w_i \left[(y_i - y_i(calc)) \frac{\partial^2 y_i(calc)}{\partial x_j \partial x_k} - \left(\frac{\partial y_i(calc)}{\partial x_j} \right) \left(\frac{\partial y_i(calc)}{\partial x_k} \right) \right] \quad (10)$$

After the deletion of the first term, an m by m matrix needs to be solved, where m is the number of adjustable parameters. The residual function is not linear, the solution must be found by an iterative procedure, which produces the shifts Δx_k that are subsequently used to produce an improved model and the procedure is then repeated. The relationship between the adjustable parameters and the intensities is not linear, and therefore the starting model must be as close as possible to the true model or else the least squares global minimum will not be reached.^[29]

One of the most popular refinement programs is GSAS, Generalized Structure Analysis System, developed at Los Alamos National Laboratory by A. Larson and R. B. Von Dreele. The program allows for the selection of one of the four peak profile functions Gaussian, Pseudo-Voigt, Thompson-Cox-Hastings modified Pseudo-Voigt (Mod-TCH-pv) and a modified version of the last function that includes anisotropic strain broadening.^[30] A Pseudo-Voigt function is a linear combination of a Gaussian with a Lorentzian of the form:

$$P(t) = \eta L(t, \Gamma) + (1 - \Gamma) G(t, \Gamma) \quad (11)$$

where the mixing factor is given as a function of the total full width at half maximum (FWHM), Γ and the Lorentzian coefficient, γ .^[30]

$$\eta = 1.36603 \left(\frac{\gamma}{\Gamma} \right) - 0.47719 \left(\frac{\gamma}{\Gamma} \right)^2 + 0.1116 \left(\frac{\gamma}{\Gamma} \right)^3 \quad (12)$$

and Γ is a function of the Gaussian FWHM (Γ_G) and γ .^[30] If the tails of the peaks are too long for instance, there is too much Lorentzian character, therefore a wider range will be required than for peaks with more Gaussian character. Caglioti,^[31] has modeled the dependence of the breadth of the reflection profiles, Γ :

$$\Gamma^2 = U \tan^2 \theta + V \tan \theta + W \quad (13)$$

where U, V, W are refinable parameters. For TCH-pv, the breadth of the Gaussian has the following form:

$$\Gamma_G^2 = U \tan^2 \theta + V \tan \theta + W + \frac{P}{\cos^2 \theta} \quad (14)$$

Generally, the Gaussians (U, V, W, P) model the peak breadth while the Lorentzians (X, Y) model the peak shape. The Lorentzians are also related with the peak breadth, Γ by:

$$\Gamma_L = X \tan \theta + \frac{Y}{\cos \theta} \quad (15)$$

The profile functions also include corrections for the sample transparency, sample height and zero shift correlated in a 2θ mismatch expression. Care must be taken in this case due to the high correlation between the profile functions *shift* and *transparency*, and the instrument parameter, *zero*.

$$\Delta 2\theta = \text{zero} + \text{shift}(\cos \theta) + \text{transparency}(\sin 2\theta) \quad (16)$$

Finally, the profile functions allow correction for the asymmetry of the peaks and for the strain anisotropy. GSAS also allows for the background, unit cell, scale and preferred orientation to be refined.

Typically, a refinement starts with the background, followed by the unit cell and profile and scale. It is worth noticing that a global minimum with powder data is much shallower than with single crystal data, and false minima are more prevalent in this case.^[28] Therefore, a refinement is done in sets of 3 to 10 cycles at a time and it needs continuous monitoring. Also, profile plots are more informative than R-values. The plots are allowed via a graphical interface called powplot, which monitors the observed and calculated patterns in different colors and the difference map. The difference plots can indicate whether the large R-values are due to a profile

problem (differences in the in the peak forms) or to the chosen structural model (intensities do not match). Changes in atomic positions within the cell causes the relative peak intensities to change, while thermal displacements emphasize the high angle data (small thermals) or deemphasize it (large thermals). In a structural refinement it is always advisable to start refining the heavy atom positions first. The scale, occupancy and thermal parameters are highly correlated^[28], therefore, it is advisable whenever possible, to constrain the thermal parameters for the same type of atoms to be the equal. This reduces the number of thermals required. Occupancies are very hard to refine, and it is better in the case of X-ray powder data to use constraints. Refinement of the profile with the structure is recommended until the structure converges; the maximum shift/e.d.s should be no more than 0.1.^[28] The most commonly used criteria of fit used by refinement programs are the R-factors presented below.

$$R_F = \frac{\sum |(I_K(obs))^{1/2} - (I_K(calc))^{1/2}|}{\sum (I_K(obs))^{1/2}} \quad (17)$$

$$R_B = \frac{\sum |(I_K(obs)) - (I_K(calc))|}{\sum (I_K(obs))} \quad (18)$$

Here I_K is the intensity of the Kth Bragg reflection. The structure factor, R_F , and the Bragg factor, R_B , are always biased by the model being used. From a mathematical point of view the most meaningful residual, R , is the R_{wp} , the weighted pattern, since it has on the numerator the quantity being minimized.

$$R_{wp} = \left\{ \frac{\sum w_i (y_i(obs) - y_i(calc))^2}{\sum w_i (y_i(obs))^2} \right\}^{1/2} \quad (19)$$

$$R_p = \frac{\sum |y_i(obs) - y_i(calc)|}{\sum y_i(obs)} \quad (20)$$

The goodness of fit χ^2 is perhaps the most popular indicator.

$$\chi^2 = \frac{R_{wp}}{R_{exp}} \quad (21)$$

R_{exp} is the expected R value, and reflects the quality of the collected data.

$$R_{exp} = \left[\frac{N - P}{\sum_i^N w_i (y_i(obs))^2} \right]^{1/2} \quad (22)$$

Here N is the number of observations and P is the number of parameters. For a good refinement, the χ^2 should be between 1.3% and 1.7%, and the R_{wp} and R_p as low as possible (5% - 20%).

1.6. Magnetic Properties

Magnetic property studies on transition metal ion complexes were initiated in the 1930's by Pauling.^[32] The main quantity in this field of research is the response of a sample to an applied magnetic field quantified by the magnetic susceptibility. Magnetic susceptibility, χ , is the extent to which a material becomes magnetized when placed in a magnetic field. Generally, a material can respond to a magnetic field in two ways. If they repel the field they are called diamagnetic (negative χ) and if they attract the field (positive χ) they are called paramagnetic. In addition to that, some paramagnetic materials, at a certain temperature, have interactions that allow them to exist in a more ordered state that can be either ferromagnetic or antiferromagnetic.^[32] They are presented schematically in the Figure 1.6, along with their characteristic susceptibilities. More complex behaviors can arise from the existence of spins in a certain structural arrangement. This results in geometric magnetic frustration, which was first

introduced by Toulouse in 1977.^[33] Magnetically frustrated systems are spin glasses, spin ices and spin liquids. Below a certain temperature, called the freezing point, T_f , in a magnetic glass, the spins freeze in random orientation. Spin glasses are systems that are characterized by disorder and frustration.

The density of force lines in the sample is called the magnetic induction, B . In a magnetic field, H , the induction B is defined as a function of the μ_0 , the permeability of free space, μ , the permeability and M is the magnetic moment of the sample.

$$B = \mu H = \mu_0 H + \mu_0 M \quad (23)$$

And the magnetic susceptibility is defined as:

$$\chi = \frac{\partial M}{\partial H} \quad (24)$$

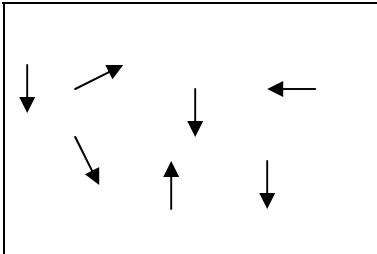
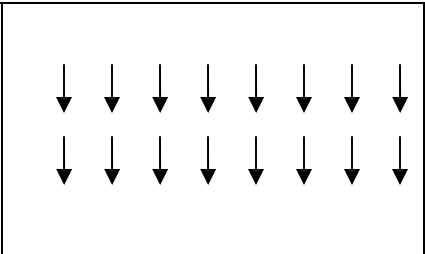
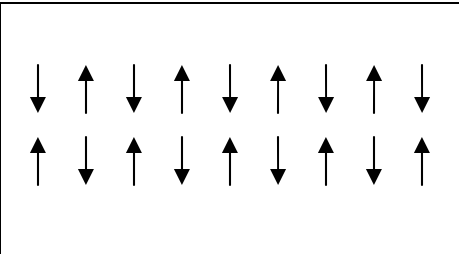
		
<p>PARAMAGNETIC χ is small and positive</p>	<p>FERROMAGNETIC χ is greater than 1</p>	<p>ANTIFERROMAGNETIC χ is smaller than for paramagnets</p>

Figure 1.6 Schematic representations for a paramagnetic, ferromagnetic and antiferromagnetic arrangement of spins.

The susceptibilities of magnetic materials are distinguished by their magnitude and their

temperature dependence. Ideal paramagnets follow the Curie law, $\chi = \frac{C}{T}$ or, when there is a

predisposition for a certain interaction between the adjacent spins, the Curie-Weiss law,

$\chi = \frac{C}{T - \theta}$. Figure 1.7 presents the molar susceptibility and reciprocal susceptibility versus

temperature for an ideal paramagnet. Figure 1.8 presents the reciprocal susceptibility versus

temperature for an antiferromagnet, $\theta < 0$, for a ferromagnet, $\theta > 0$, in comparison an ideal paramagnet, $\theta = 0$.

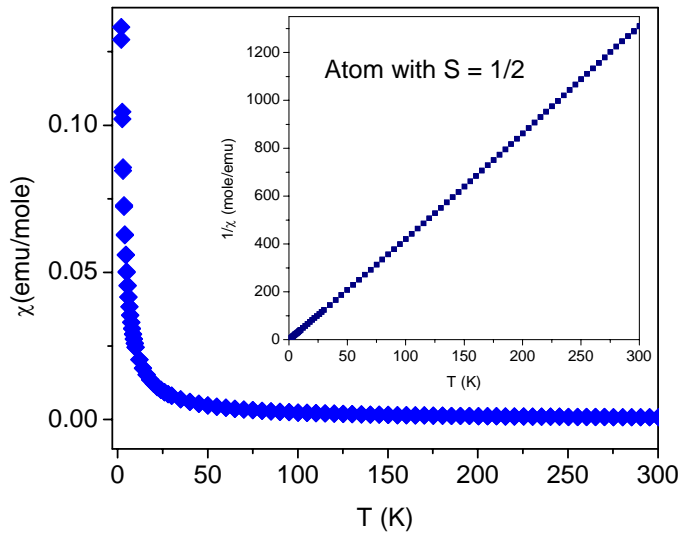


Figure 1.7 Susceptibility versus temperature data for an ideal Curie-Weiss paramagnet with a spin 1/2. The reverse susceptibility versus temperature showing a linear behavior.

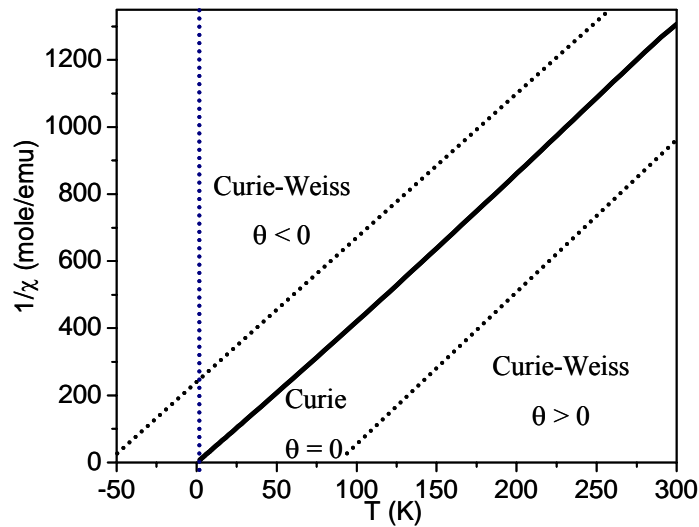


Figure 1.8 The reverse susceptibility versus temperature for an ideal paramagnet $\theta = 0$, a ferromagnet $\theta > 0$ and an antiferromagnet $\theta < 0$.

In paramagnetic substances that show a predilection towards ferromagnetism, the value of θ , the Weiss constant, coincides with the ferromagnetic Curie temperature, T_C , the temperature at which the susceptibility becomes infinite. This behavior is presented in Figure 1.9. Ferromagnets have also a distinctive magnetization (M) versus applied field (H) dependence below and above their critical temperature, T_C . The curve is not linear, and the behavior is not reversible (hysteresis). A computer simulated hysteresis loop is presented in Figure 1.10. When the field increases, the magnetization in the sample reaches a maximum, called the saturation magnetization M_s . As the field is reduced back to zero, M follows a different path and does not return to zero when the field is zero.

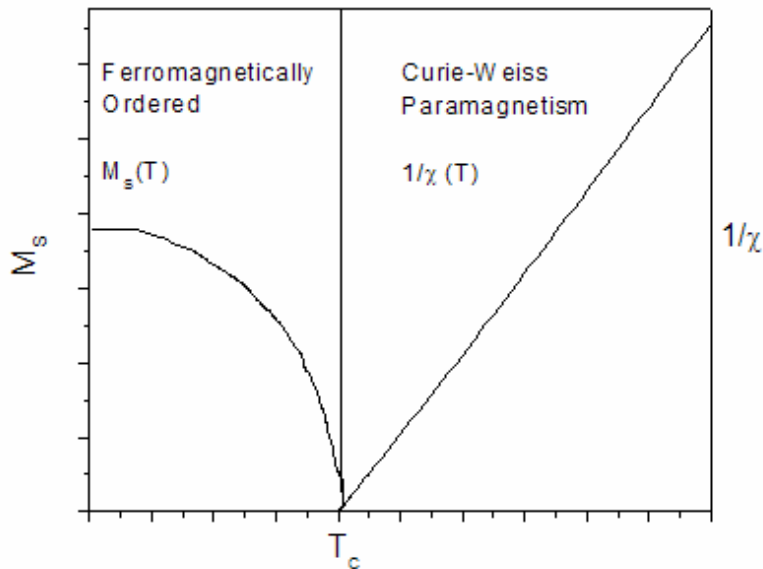


Figure 1.9 The magnetization versus temperature (left) and the inverse susceptibility versus temperature for a ferromagnet. The Curie point is shown.

The magnetization still present in the material after the field has been turned off is called remanent magnetization, M_{rem} . Materials with large remanent magnetization are called hard ferromagnets while materials with small M_{rem} are called soft ferromagnets. Hard ferromagnets are needed for applications like magnetic recording, while soft ferromagnets are useful for magnetic transformer cores.^[32]

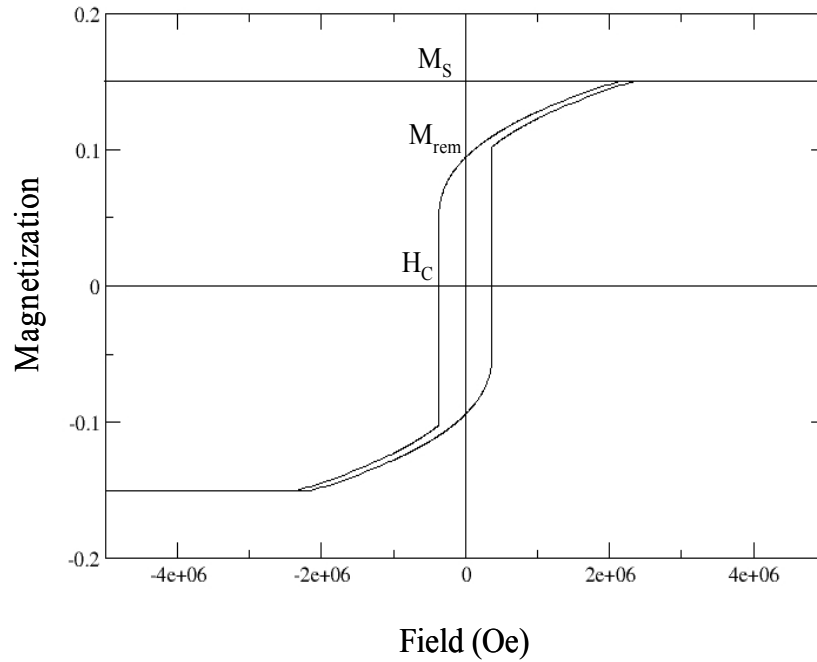


Figure 1.10 The magnetization versus field for a ferromagnet presenting a hysteresis loop.

In paramagnets with a negative Weiss constant, $\theta < 0$, antiferromagnetic order is established under a certain temperature called the Néel temperature. The susceptibility and the reciprocal susceptibility versus temperature for an antiferromagnet are presented in Figure 1.11.

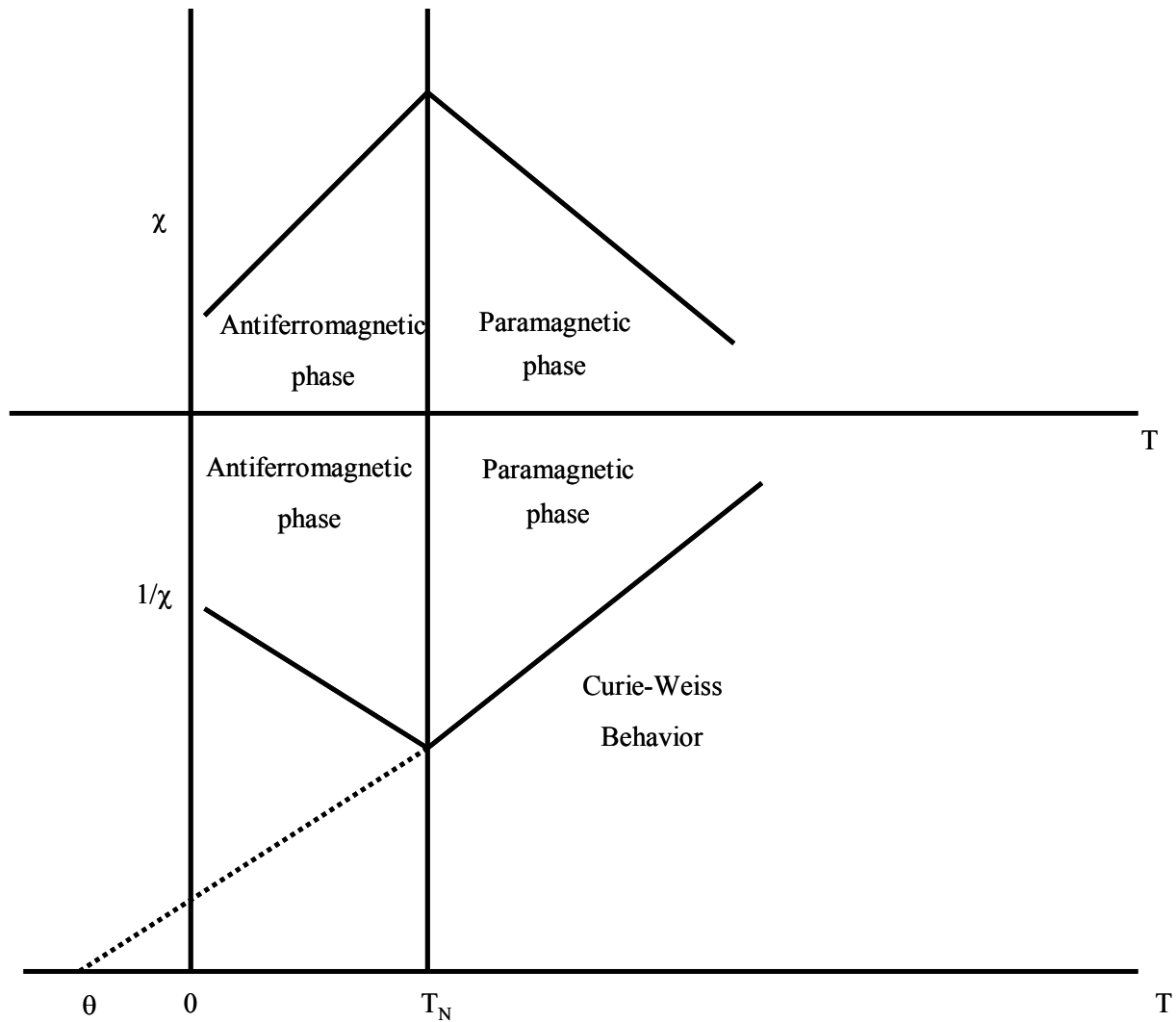


Figure 1.11 Susceptibility versus temperature and reciprocal susceptibility versus temperature for an antiferromagnet emphasizing the transition temperature below which the spins are aligned antiferromagnetically (T_N - Néel temperature).

Other types of magnetic materials are spin glasses, spin liquids and spin ices.

Microscopically, the glass state corresponds to a configuration of spins frozen in a random pattern. In this respect, they have been called “cooperative paramagnets”.^[33, 34] These materials experience a phenomenon called magnetic frustration. Frustration appears when a large fraction of the magnetic sites in a lattice are subject to competing constraints.^[33] A few examples of frustrated lattices are shown in the Figure 1.12. In the case of a triangular lattice characterized by

an antiferromagnetic arrangement of the spins, if two spins adopt an antiparallel alignment, then the third will not be able to be antiferromagnetically coupled with both of its neighbors. A similar situation is generated in the case of a tetrahedral arrangement of spins, as illustrated in Figure 1.12 b. Even a square plaquette can be frustrated when the next-neighbor (nn) and next-near-neighbor (nnn) interactions are comparable (Figure 1.12 c). Below a certain temperature, called the freezing point, T_f , the spins are locked in a random orientation and the material is in the glassy phase. ^[33,34]

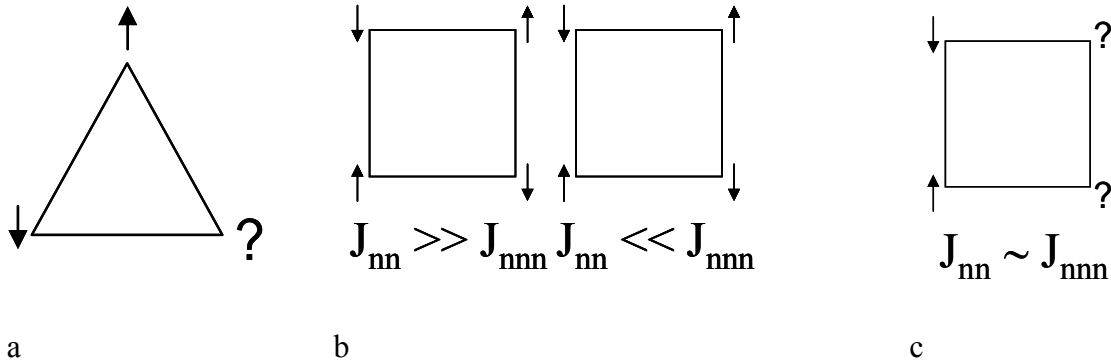


Figure 1.12 Examples of geometrically frustrated systems: a) the triangular lattice; b) unfrustrated square planar systems; c) frustrated square plaquette.

1.7. Heat Capacity and ac/dc Magnetic Susceptibility Methods

In the investigation of a magnetic system, one important measurement is the specific heat at low temperatures.^[32] Thermal effects give evidence of magnetic ordering. An order-disorder transition, such as paramagnetic to ferromagnetic or paramagnetic to antiferromagnetic, can be investigated by heat capacity measurements at low temperatures. For simple one-component systems, the equilibrium state can be described by two variables (like temperature and pressure). In the case of a magnetic system, there is an additional variable, the magnetic field. Therefore, the first law of thermodynamics can be written as:

$$dQ = dU - HdM \quad (25)$$

This states that the heat added to the system, dQ , is equal to the algebraic sum of the increase in the internal energy, dU , and the work done on the system in order to change the magnetization, HdM . In the absence of an applied magnetic field $dQ = dU = TdS = C_p dT$. This makes possible the determination of the entropy associated with the magnetic transition. The change in entropy is simply the integrated area underneath the C_p/T versus T curve.^[32] The simple integration process is complicated by lattice vibrations, short range interactions, zero field splitting and electronic contributions to the specific heat.^[32] All of these effects need to be subtracted out, in order to calculate the magnetic contribution to the heat capacity. A very good method to account for all of these effects is to find a non-magnetic equivalent, measure its specific heat and compare it to the specific heat of the magnetic system. This procedure relies on the correspondent states law, which in this case states that specific heat of similar substances will be similar, if weighted by the differences in their molecular weights.^[32] If such a non-magnetic equivalent is not available, one can use high temperature series expansions to calculate the lattice specific heat with the addition of other terms to account for short range interactions.^[32]

$$C(T) = aT + bT^3 + cT^5 + dT^7 + e/T^2 \quad (26)$$

where a, b, c, d, e are adjustable parameters. The last term represents the short-range interaction contribution to the heat capacity. In principle, more terms can be added or respectively removed from the series. In a specific heat measurement, the maxima located at low temperatures in the shape of the letter lambda represent second order magnetic transitions. Because they represent transitions to a long range order, they can be either ferromagnetic or antiferromagnetic. Heat capacity alone cannot decide whether it is one or the other. In an applied field, a ferromagnetic

transition will shift to higher temperatures. The opposite is seen for an antiferromagnetic transition.^[32]

Magnetic properties can be followed by susceptibility measurements. One of the most commonly used methods to determine the response of a material to the applied magnetic field is the direct current magnetic susceptibility, particularly zero field cooled – field cooled (ZFC/FC). In the zero field cooled experiment, the sample is cooled at low temperatures, typically 5 K, then a magnetic field is applied and the magnetization is monitored as the sample is warming up in field. In the field cooled measurement, a field is applied at room temperature, the sample is cooled with the field at 5 K and then the magnetization is monitored as the sample warms up. If the curves of magnetization versus temperature for these two experiments, ZFC/FC, do not differ, and no inflection points are present at any temperatures, then the magnetic behavior is paramagnetic. If maxima are present, then the compound shows a transition to a long-range or short-range ordered phase. Moreover, if the two curves, ZFC/FC split, then the transition to a long range order needs further investigation. This usually can be a sign of a ferromagnetic or ferrimagnetic kind of interaction. To clarify the nature of a magnetic transition, it is sometimes helpful to draw a magnetic moment versus temperature plot. The magnetic moment can be obtained from the magnetic susceptibility using ^[32]:

$$\mu = \sqrt{7.99 \chi T} \quad (27)$$

If the magnetic moment decreases with decreasing the temperature, down to the magnetic transition, then the interaction between the different magnetic ions is antiferromagnetic. If the magnetic moment increases, then the interaction is ferromagnetic. Another indication for the nature of the magnetic transition is the sign and magnitude of the Weiss constant, θ , obtained from a reciprocal susceptibility versus temperature plot, for the high temperature region,

typically above the transition or above 10^{-4} K. A positive χ (a negative χ) indicates ferromagnetic interactions (antiferromagnetic interactions). For a positive χ , one can do a hysteresis loop measurement above and below the magnetic transition. In this kind of measurement, a high magnetic field is applied to the sample at a certain temperature, and the magnetization is monitored as a function of applied magnetic field. This dc measurement is appropriate for ferromagnets, ferrimagnets, canted and weak ferromagnets. Ferromagnetism has two distinguished features, one is the parallel alignment of the magnetic moments and another one is the formation of domains. In the absence of an applied magnetic field, ferromagnetic and antiferromagnetic order cannot be clearly separated. Therefore, alternating current (ac) susceptibility measurements help distinguish between the two.^[35]

The dc magnetometer and the ac susceptometer are two different tools for investigating magnetic phenomena. Both of these measurements rely on sensing coils to measure the variation in the magnetic flux due to a magnetized sample. The difference relies in how the flux variation is achieved. In a dc experiment, the sample is magnetized by a static magnetic field arising from a superconducting magnet (for a SQUID instrument). The sample is moved to a detection coil that measures variations in flux due to the magnetization of the sample by the magnetic field. In an ac measurement, the sample is centered within a coil while driven with an external ac field. This produces a time dependent magnetization that a second detection coil can measure. In an ac susceptibility measurement, the sample is placed within a coaxial set of coils and a low frequency signal is applied.^[36-38] The change in mutual inductance between the coils is proportional to the magnetic susceptibility. The ac method has several advantages over the dc measurement. The applied magnetic field can be very small (a few oersteds). Because the induced sample moment is time dependent, ac measurements give information about

magnetization dynamics, which cannot be obtained by dc methods. The measurement is very sensitive to small changes in the magnetization as a function of applied frequency. In the low frequency limit, the ac and dc measurements are similar. The magnetic moment of the sample follows the magnetization as a function of field curve. For small ac fields:

$$M_{AC} = (dM / dH) \bullet H_{AC} \sin(\omega t) \quad (28)$$

where H_{AC} is the amplitude of the driving field, ω is the driving frequency, and

$$\chi = (dM / dH) \quad (29)$$

At higher applied frequencies, the ac moment does not follow the dc magnetization curve, due to dynamic processes in the sample. In this case, the magnetization may lag behind the field, therefore ac susceptibility measurements yield to two quantities: the magnitude of the susceptibility, χ and the phase shift φ .^[36-38] This can be thought of as having an in-phase or real component, χ' , and an out-of-phase or an imaginary component, χ'' . The imaginary component indicates dissipative processes in the sample.^[36-38]

$$\chi' = \chi \cos \varphi \quad (30)$$

$$\chi'' = \chi \sin \varphi \quad (31)$$

$$\chi = \sqrt{\chi'^2 + \chi''^2} \quad (32)$$

$$\varphi = \arctan(\chi'' / \chi') \quad (33)$$

The average field inside a material is the only relevant field for a paramagnet or an antiferromagnet. This is not true for a ferromagnet because of the demagnetizing effects, due to their very high internal field. Since an applied magnetic field causes domain wall movement, domains grow larger and align with the field. This can be seen in the ac susceptibility data. In the real part for high applied frequencies, the domain walls are not able to follow the ac field. A

strong frequency dependence of the T_C is observed in the real part of the ac susceptibility (see Table 1.4). The T_C frequency dependence follows an Arrhenius law.^[35]

$$\nu = \nu_0 \exp\left[-E_a / k_B T_f\right] \quad (34)$$

Here, E_a is the potential barrier separating two easy orientations of the spin clusters and ν is the driving frequency of the ac measurement. In addition, there is a signal in the imaginary part around T_C indicating irreversible domain wall movement or absorption due to a permanent moment. This does not happen in an antiferromagnet. An antiferromagnet does not show a frequency dependence of the real part nor a signal in the imaginary part of the ac susceptibility.

Unfortunately, a spin glass resembles in very many respects a ferromagnet. Spin glasses show a maximum at the freezing temperature, T_f , in the real component of the ac susceptibility. In addition, relaxation and irreversibility in spin glasses give rise to a non-zero signal in the out of phase component. The freezing point in a spin glass is also frequency dependent, but it follows a Vogel-Fulcher law.^[35]

$$\nu = \nu_0 \exp\left[-E_a / k_B (T_f - T_0)\right] \quad (35)$$

Here, T_0 is an adjustable phenomenological parameter accounting for inter-cluster interactions. In an applied magnetic field, a spin glass transition should round with small fields and even disappear in higher fields. This is not the case for a ferromagnetic transition. The freezing point in a spin glass cannot be seen in heat capacity data, which distinguishes a ferromagnet from a spin glass. At temperatures well above T_f , the spins are in a paramagnetic state. As the temperature is reduced, the spins experiencing the strongest exchange interactions can couple to form small magnetic entities. Further reduction allows more spins to couple and entities of different sizes and relaxation times would form. Thus, a dynamical growth of such “islands” with a distribution of sizes and relaxation times prevails and therefore the behavior of the system will

depend on the time constant of a particular experiment. In a reentrant spin glass, within these “islands” the spins are ferromagnetically arranged, but the interactions between these clusters are via antiferromagnetic frustrated bonds. It is still unclear if the clusters, that are uncoupled in the ferromagnetic phase, can couple in the spin glass phase so that the entropy T_f the spin glass state is lowered relative to the ferromagnetic state.^[35] A summary of the aforementioned magnetic and heat capacity analysis is given in the Table 1.3.

Table 1.3 The measurement and the expected behavior for the most common magnetic behaviors.

Measurement	Paramagnetic PM	Spin Glasses SG	Antiferromagnetic AFM	Ferromagnetic FM
Heat Capacity	Schottky anomaly if anisotropy is present	Linear C/T and if short range interactions	λ - anomaly at T_N	λ - anomaly at T_C
DC χ	ZFC/FC do not split	ZFC/FC split at the freezing point, T_f	ZFC/FC do not split Neel transition, $\theta < 0$	ZFC/FC split Curie transition, $\theta > 0$
AC χ' Measures the magnetic moment	nothing	Freezing point, T_f varies with frequency (Vogel-Fulcher)	Neel transition No frequency dependence	Curie transition Very large dependence on frequency (Arrhenius law)
AC χ'' Dissipative processes – eddy currents	nothing	Frequency dependent (1-2%)	Nothing	Highly frequency dependent (8-10%)
In field ac	nothing	Round up even with small fields	Nothing	They do not round

1.8. Electronically Driven Effects in Layered Perovskites. Second Order Jahn Teller Effect

Some layered perovskites are stabilized by the presence of a d^0 transition metal in the B site of perovskite slabs. The stabilization comes from a second order Jahn Teller effect consisting of out of center distortions of the BO_6 octahedra. It is believed that this effect has an electronic origin. The second order Jahn Teller effect consists of out of center distortions of the TiO_6 octahedra, which generates unsymmetrical B – O – B distances. For highly charged and small sized ions, the HOMO-LUMO gap is lowered and permits the mixing between the 2s, 2p orbitals on the oxygen with the d orbitals on the transition metal ion, such that the occupied states are stabilized at the expense of the unoccupied states. The distortion is suppressed by increasing the number of electrons on the transition metal ion, so the effect increases with the acidity of the B site metal.^[39,40] Alternatively, if a vibration lowers the symmetry, here it could go from octahedral to a square pyramidal, and then this allows the mixing of two levels of different symmetry.^[41]

1.9. Electronic Band Structure Calculations

The study of any solid would not be complete without a good knowledge of its electronic properties. Many of the characteristic properties of a solid emerge directly from the behavior of the electrons in them. Electrical conduction, optical properties, magnetic properties and surface properties, are only a few of examples.^[39]

There are approximations one can use to calculate the electronic properties of a solid. The methods used can be divided into *ab initio* and *semiempirical*. There are advantages and disadvantages associated with the both. While *ab initio* methods are generally more accurate, they also are very computationally demanding. One also needs to consider the crystal structures, which consist of a large number of atoms per unit cell. Semiempirical methods are less accurate but they can yield realistic results in a more reasonable amount of time for large unit cells.

Yet Another Extended Hückel Molecular Orbital Package (YAEHMOP) is a semiempirical package that allows electronic structure calculations and visualization of the results. YAEHMOP is based on a tight-binding approximation called the extended Hückel method. The program was developed at Cornell University in Prof. Roald Hoffmann's group.^[41,42] The tight binding approximation or the linear combination of atomic orbitals method (LCAO) is appropriate for cases in which the overlap of atomic wavefunctions is large enough to require corrections to the isolated atom picture but not so large to require band theory. Therefore, the method is useful for describing the electronic structure of insulators, and partially filled d-shells in transition metal compounds. The Hamiltonian for the system is the atomic Hamiltonian with a correction for the periodicity of the lattice. The orbitals used in the calculations are Slater orbitals.^[42-44]

$$H = H_{at} + \Delta U(r) \quad (36)$$

The diagonal elements of the Hamiltonian are the ionization potentials. The other necessary matrix elements are calculated by the extended Hückel method.^[42-44] The overlap, $S_{\beta\alpha}$, between the atomic orbitals α and β , on adjacent atoms is used to find the off-diagonal elements of the Hamiltonian as described in the following equation.

$$\langle \beta | H | \alpha \rangle = GS_{\beta\alpha} (\varepsilon_{\beta} + \varepsilon_{\alpha}) / 2 \quad (37)$$

Here G is a scale factor, usually 1.75.^[44] If $|\alpha\rangle$ is an eigenstate of the Hamiltonian, with the eigenvalue ε_α then, $H|\alpha\rangle = \varepsilon_\alpha|\alpha\rangle$ and then for $\alpha = \beta$

$$\langle\alpha|H|\beta\rangle = \langle\beta|\varepsilon_\alpha|\alpha\rangle = \varepsilon_\alpha\langle\beta|\alpha\rangle = \varepsilon_\alpha S_{\beta\alpha} \quad (38)$$

An average value is used instead of just ε_α for the case $\alpha \neq \beta$.

These matrix elements are substituted in the Hamiltonian matrix, and then the matrix is diagonalized to solve the following eigenvalue equation.^[44]

$$\sum_i H_{ij} u_{ij} - E u_j = 0 \quad (39)$$

One of the biggest drawbacks of this method is that electrostatic repulsions between electrons are treated in an approximate way (they are included as an average potential). When the atomic overlap is small, narrow bands are formed and the effects of electron-electron repulsion become predominant. This is when both the band theory and the LCAO method break down.^[43,44] A full treatment of electron-electron interaction is very difficult, even when dealing with simple compounds, e. g. NiO. A successful approach is the Hubbard model. In this model, a gross approximation is made from the beginning. The model considers that the only important interaction between electrons is for the electrons residing on the same atom (the repulsion between electrons on different atoms is neglected). Assuming that the overlap between the orbitals on adjacent atoms is small, then the energy required to remove an electron from one atomic orbital (I , the ionization potential) and placing it on a site already occupied by another electron (A , the electron affinity) gives the repulsion energy between the two electrons (the Hubbard, U).

$$U = I - A \quad (40)$$

The effect of electron repulsion is to create sub-bands, each holding one electron, and therefore open a gap in the electronic states at the Fermi level. Two parameters are important in the Hubbard model, the bandwidth, W , and the repulsion parameter, U . When the overlap between the atoms is predominant $W > U$, the LCAO and band theory will work. As the orbital overlap diminishes, $W < U$, the repulsion effect takes over and progressively localizes the electrons on individual atoms. Unfortunately, the Hubbard model must be embedded within another method to yield realistic results. YAEHMOP does not support this option at the moment.^[39,43,44] For most of our systems, the extended Hückel model is appropriate because of the large bandgap and extreme localization (small or lack of conductivity). These properties preclude a large interatomic overlap.^[39]

The electronic structure for the triple layered Ruddlesden-Popper, $A_2La_2Ti_3O_{10}$, is presented in Figure 1. 13. The density of states are calculated with YAEHMOP.^[42] This compound, as the entire precursor materials used in this research, is an insulator with a direct band gap of ~ 4 eV. In this compound, $Na_2La_2Ti_3O_{10}$, Ti is in its maximum oxidation state, +4, so constitutes a d^0 electronic system. Titanium is in an octahedral coordination, so its d levels will split in t_{2g} (they have π symmetry) and e_g (they have σ symmetry). The Fermi level is located at -14.55 eV. Below the Fermi level, the valence band is formed of Ti^{4+} s p states mixed with O^{2-} s p states that form a σ band. Right below the Fermi level t_{2g} orbitals on the transition metal mix with the O p_π orbitals to form a π bonding combination. Above the Fermi level the antibonding π^* band is found in the conduction band.

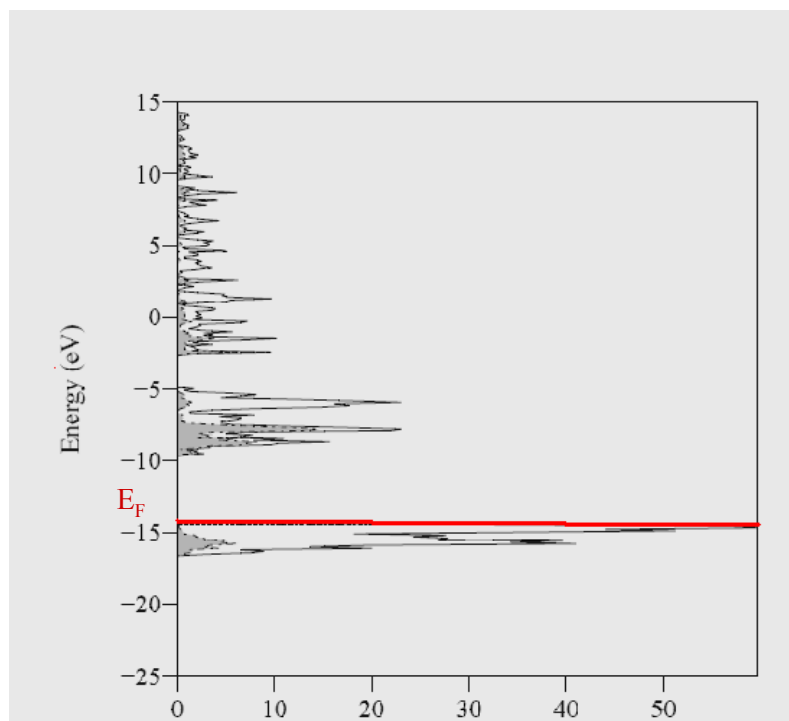


Figure 1.13 DOS for $\text{Na}_2\text{La}_2\text{Ti}_3\text{O}_{10}$

1.10. References

- [1] Bednorz, J. G. and Muller, K. A., *Z. Phys. B* **1986**, 64, 189.
- [2] Hashimoto, Y. M.; Yoshida, K.; Nishizaki, S.; Fujita, T.; Bednorz, J. G. and Lichtenberg, F., *Nature* **1994**, 372, 532.
- [3] Takata, T.; Shinohara, K.; Tanaka, A.; Hara, M.; Kondo, J. N.; Domen, K., *J. of Photochemistry and Photobiology, A Chemistry* **1997**, 106 (1-3), 45.
- [4] Gong, W; Xue, J. S.; Greedan, J. E., *Journal of Solid State Chemistry* **1991**, 91(1), 180.
- [5] Roger H. Mitchell *Perovskites Modern and Ancient*, Almaz Press Inc., Ontario, Canada, 2002.

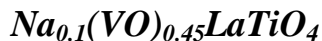
- [6] a) Seshadri, R.; Martin, C.; Domenges, B.; Raveau, B.; *Chem. Matter.* **1997**, *9*, 1778; b) Seshadri, R.; Martin, C.; Raveau, B.; *Chem. Matter.* **1997**, *9*, 270.
- [7] a) Dion, M.; Ganne, M.; Tournoux, M.; *Mater. Res. Bull.* **1981**, *16*, 1429; b) Jacobson, A. J.; Johnson, J. W.; Lewandowski, J. T.; *Inorg. Chem.* **1985**, *24*, 37.
- [8] Ruddlesden, S. N. and Popper, P.; *Acta Crystallogr.* **1957**, *10*, 538.
- [9] Gopalakrishnan, J.; Uma, S.; Bhat, V.; *Chem. Mater.* **1993**, *5*, 132.
- [10] Cushing, B. L.; Wiley, J. B.; *Mater. Res. Bull.* **1999**, *34*, 271.
- [11] Jones, R.; McKinnon, W. R.; *Solid State Ionics* **1991**, *45*, 173.
- [12] Gomez-Romero, P.; Palacin, M. R.; Casan, N.; Fuerts, A., *Solid State Ionics* **1993**, *424*, 63.
- [13] Armstrong, A. R.; Anderson, P. A.; *Inorg. Chem.* **1994**, *33*, 4366.
- [14] Fang, M.; Mallouk, T. E.; *Chem. Mater.* **1999**, *11*, 1519.
- [15] West A. R.; *Solid State Chemistry and its Applications*; John Wiley & Sons Ltd., 1984.
- [16] Schaak, R. E.; Mallouk, T. E.; *Chem. Mater.* **2002**, *14*, 1455.
- [17] Gopalakrishnan, J.; Sivakumar, T.; Ramesha, K.; Thangadurai, V.; Subanna, G. N.; *J. Am. Chem. Soc.* **2000**, *122*, 6237.
- [18] a) Lalena, John N.; Wiley, John B., Book of Abstracts, 215th ACS National Meeting, Dallas, March 29-April 2 **1998** and b) Schaak, Raymond E.; Afzal, Dawood; Schottenfeld, Joshua A.; Mallouk, Thomas E, *Chemistry of Materials* **2002**, *14*(1), 442.
- [19] Toda, K.; Watanabe, J.; Sato, M., *Mat. Res. Bull.* **1996**, *31*, 1427.
- [20] Hyeon, K. A. and Byeon, S. H., *Chem. Mater.* **1999**, *11*, 352.
- [21] Gopalakrishnan, J.; Bhat, V., *Inorganic Chemistry* **1987**, *26*(26), 4299.
- [22] McIntyre, R.A.; Falter, A. U.; Li, S.; Simmons, W. B; O'Connor, C. J.; Wiley, J. B. *J. Am. Chem. Soc.* **1998**, *120*, 217.

- [23] Lalena, J.N.; Cushing, B.L.; Falster, A.U.; Simmons, W.B.; Seip, C.T.; Carpenter, E.E.; O'Connor, C.J. and J.B. Wiley, *Inorg. Chem.* **1998**, *37*, 4484.
- [24] Byeon, S. H. J.; Yoon, J.; Lee, S. O. *J. Solid State Chem.* **1996**, *127*, 119.
- [25] a) Crosnier-Lopez, M. P.; Le Berre, F.; Fourquet, J. L. *Journal of Materials Chemistry* **2001**, *11*(4), 1146; b) Ollivier, P. J.; Mallouk, T. E., *Chemistry of Materials* **1998**, *10*, 10.
- [26] R. Jenkins and R. L. Snyder, *Introduction to X-ray Powder Diffraction*, John Wiley & Sons Ltd., **1996**.
- [27] David, W. I. F.; Shankland, K.; McCusker, L.B. and Baelocher, Ch. *Structure Determination from Powder Diffraction Data*; Oxford University Press, **2002**.
- [28] McCusker, L. B.; Von Dreele, R. B.; Cox, D. E.; Louër, D. and Scardi, P. *J. Appl. Cryst.*, **1999**, *32*, 36.
- [29] Young, R. A. *The Rietveld Method*, Oxford University Press, **1993**.
- [30] Thompson, P.; Cox, D. E; Hastings, J. B. *J. Appl. Cryst.* **1987**, *20*, 79.
- [31] Caglioti, G.; Paoletti, A. ; Ricci, F. P. *Nucl. Instrum. Method*, **1958**, *35*, 223.
- [32] Carlin, R. L. *Magnetochemistry*, Springer-Verlag Berlin Heidelberg, **1986**.
- [33] Greedan, J. E. *J. Mater. Chem.* **2001**, *11*, 37.
- [34] Villain, J. Z. *Phys. B* **1979**, *33*, 31.
- [35] Moortjani, K.; Coey, J. M. D. *Magnetic glasses*, Elsevier Science Publishers B. V., **1984**.
- [36] Lee, L. P.; Chark, M. S.; Zaharchuk, G. *Appl. Phys. Lett.* **1991** *59*, 3051.
- [37] Gomory, F. *Supercond. Sci Technol.* **1997** *10*, 523.
- [38] Couach, M. and Khoder, A. F. *Magnetic Susceptibility of Superconductors and Other Spin Systems* ed. R. a. Hein, T. . Francavilla and D. H. Liebenberg, Plenum, New York, **1992**.
- [39] Cox, P. A. *The electronic structure and chemistry of solids*, Oxford University Press, **1987**.

- [40] Bhuvanesh, N. S. P. and Gopalakrishnan, J.; *J. Mater. Chem.* **1997**, 7(12), 2297.
- [41] Hofmann, R. *Solids and Surfaces. A Chemist's View of Bonding in Extended Structures*, VCH Publishers, Inc. **1988**.
- [42] Yet Another Extended Hückel Molecular Orbital Package (YAEHMOP),
<http://yaehmop.sourceforge.net/>.
- [43] Ashcroft, N. W. and Mermin, N. D. *Solid State Physics*, Holt Rinehart and Winston, **1976**.
- [44] Harrison, W. A. *Electronic Structure and the Properties of Solids. The Physics of Chemical Bond*, Dover Publications, Inc., New York, **1989**.

Chapter 2

Synthesis and Characterization of the New Layered Perovskite,



2.1 Introduction

Layered perovskites of the Dion-Jacobson (DJ), $\text{A}'[\text{A}_{m-1}\text{B}_m\text{O}_{3m+1}]$, and Ruddlesden-Popper (RP), $\text{A}'_2[\text{A}_{m-1}\text{B}_m\text{O}_{3m+1}]$, families, where A' = alkali or alkali earth metal, A = rare earth or alkali earth metal, B = transition metal, m goes from 1 to infinity, contain perovskite strata interleaved with A' ion-exchangeable cations. The reactivity of the A' cations makes these compounds effective precursors to new low temperature phases via topochemical routes. In the case of the triple layered RP compounds monovalent ion exchange has led to $\text{Li}_2\text{La}_2\text{Ti}_3\text{O}_{10}$ and the acidic form $\text{H}_2\text{La}_2\text{Ti}_3\text{O}_{10}$, while by divalent ion exchange $\text{MLa}_2\text{Ti}_3\text{O}_{10}$ with $\text{M} = \text{Ca}, \text{Co}, \text{Zn}, \text{Cu}$ have been obtained.^[1,2] Gopalakrishnan and coworkers investigated the triple-layered perovskite, $\text{K}_2\text{La}_2\text{Ti}_3\text{O}_{10}$ and reported initial studies on the ion exchange of vanadyl species.^[3] Ion exchange reactions with the single-layered perovskite, NaLaTiO_4 , have also resulted in a series of new compounds. Monovalent exchange has produced KLaTiO_4 , AgLaTiO_4 (α and β forms) and HLaTiO_4 and divalent exchange has resulted in alkaline earth, $\text{Ca}_{0.5}\text{LaTiO}_4$, and transition metal, $\text{M}_{0.5}\text{LaTiO}_4$ ($\text{M} = \text{Cu}, \text{Co}, \text{Zn}$) RP oxides.^[4-6] The exchange behavior of other RP phases has also been studied. These include the double and triple-layered perovskites. Herein we expand on this approach with a detailed study on the synthesis and characterization of the new single-layered perovskite, $\text{Na}_{0.1}(\text{VO})_{0.45}\text{LaTiO}_4$.

2.2 Experimental

2.2.1. Synthesis

NaLaTiO₄ was synthesized by conventional solid-state reaction with a method similar to that of Toda et al.^[7,8] Initially, La₂O₃ (Alfa Aesar, 99.99%) was preheated before use to 1000 °C for 16 hrs. to remove any hydroxide and carbonate contaminants. Then stoichiometric amounts of La₂O₃ and TiO₂ (Alfa Aesar, 99.99%) were combined with a 40% molar excess of Na₂CO₃ (Alfa Aesar, 99.99%) and heated in an alumina crucible at 950 °C for 30 minutes. After the reaction, to remove unreacted Na₂CO₃, the sample was washed with warm water. The sample was then rinsed with acetone and dried at 150 °C overnight. Phase purity for NaLaTiO₄ was confirmed by X-ray powder diffraction (XRD). The sample was indexed on the tetragonal unit cell $a = 3.7730(1)$ Å and $c = 13.0220(2)$, which is in agreement with the values reported in the literature.^[8]

Ion exchange was used to substitute the Na ions in NaLaTiO₄ with vanadyl ions, (VO)²⁺. The source of the vanadyl unit was vanadyl sulfate hydrate (VOSO₄·nH₂O, Alfa Aesar, 99.99%). NaLaTiO₄ (0.2737 g, 0.1 mmole) was mixed in a 1:2 molar ratio with VOSO₄ (0.2375 g) in 100 ml water. The solution was heated for two days between 50 – 65 °C with continuous stirring. The sample was isolated after one day and combined with a fresh solution of vanadyl sulfate. The final product was dark green in color. The exchange reaction between NaLaTiO₄ and vanadyl sulfate dehydrated was also studied in a sealed evacuated Pyrex tube; below 150 °C, the solids do not react and above 200 °C vanadyl sulfate decomposes.

2.2.2 Characterization

The product phase could not be completely dissolved in a variety of strong acids. So to analyze the extent of exchange, the exchange solution after reaction was analyzed for the sodium byproduct and unreacted vanadyl. The analysis was carried out by inductively coupled plasma spectrometry (ICP). Standard solutions were prepared from Specpure Alfa Aesar 10,000 µg/ml for sodium and vanadium. All the standards and the samples were analyzed in a 5% HNO₃ solution (vol./vol.). Energy dispersive spectroscopy (EDS) was carried out on a JEOL (model JSM-5410) scanning electron microscope (SEM) equipped with an EDAX (DX-PRIME) microanalytical system.

X-ray powder diffraction studies were carried out on a Phillips X'Pert System (Cu K α radiation $\lambda=1.5418$ Å) equipped with a graphite monochromator. Data were collected in a step scan mode between 2 and 95° 2 θ with a step size of 0.02° and a counting time of 10 s. Structural refinement was done by the Rietveld method with the GSAS package of programs.^[9] Thirty-nine parameters were varied including background, peak shape, cell, atom positions, thermal parameters and occupancies. In the beginning of the refinement, the Le Bail method^[10] was employed for the background and peak shape parameters. The R-factor (R_p), the weighted R-factor (wR_p), and the goodness of fit, χ^2 , are defined as: $R_p = \sum[y_{io}-y_{ic}]/\sum y_{io}$, $wR_p = [\sum w_i(y_{io} - y_{ic})^2/\sum w_i(y_{io})^2]^{1/2}$, $R_F = \sum[|I_k(\text{obs})|^{1/2} - |I_k(\text{calc})|^{1/2}|/[\sum I_k(\text{obs})]^{1/2}$, and $\chi^2 = [wR_p/R_{\text{exp}}]^2$, where $R_{\text{exp}} = [(N - P)/\sum w_i y_{io}^2]^{1/2}$ and y_{io} and y_{ic} are the observed and the calculated intensities, w_i is the weighting factor, N is the total number of observed intensities when the background is refined, and P is the number of adjusted parameters.

Infrared spectroscopy (IR) was performed on a Perkin Elmer 2000 FT-IR; the samples were analyzed as pellets in a 1:100 molar ratio with dry KBr. For the electron paramagnetic resonance (EPR) measurements, an EMX X-band Bruker spectrometer was used.

Magnetic measurements were performed on a Quantum Design MPMS-5S Superconducting Quantum Interference Device (SQUID) magnetometer between 2 and 300 K at 1000 Oe.

Thermal behavior was studied on a TGA 51 thermogravimetric analyzer and a Netzsch 404 S differential scanning calorimeter (DSC); measurements were performed in oxidizing, inert and reducing atmospheres between room temperature and 800 °C by heating samples at 10 °C/min in H₂ (8% hydrogen in argon), O₂ and Ar, respectively.

2.3 Results

2.3.1. Synthesis

Ion exchange reactions were performed between NaLaTiO₄ and aqueous vanadyl sulfate solutions. XRD indicated that the reaction was complete after two days when carried out between 50 – 65 °C. Heating at temperatures higher than 70 °C leads to the formation of a LaVO₄ impurity phase. In all cases a small amount of white flocculant was observed on the solution surface of the reaction mixture even under mild reaction conditions. EDS analysis showed that the flocculant contained La, Ti, and O indicating that it is most likely exfoliated perovskite layers.^[11] Longer reaction times or a larger excess of VOSO₄ leads to a greater amount of flocculant. The latter is expected to be

related to the acidity of the VOSO_4 solution ($\text{pH} \sim 2$). Elemental analysis of the final product by ICP showed a composition of $\text{Na}_{0.10 \pm 0.02}(\text{VO})_{0.45 \pm 0.01}\text{LaTiO}_4$, corresponding to a 90% exchange.

2.3.2. Structure

Ion exchange takes place in a topotactic manner in that the structure of the perovskite host is maintained. Figure 2.1 shows a comparison of the X-ray powder diffraction patterns before and after exchange. Table 2.1 shows the variation in unit cell parameters and cell volume. There is about an 8 % reduction in cell volume on exchange with the greatest change occurring in the c direction (contraction $\sim 0.7 \text{ \AA}$). This contraction can be understood knowing that two sodium ions are replaced with one vanadyl cationic unit.

Structural refinement of $\text{Na}_{0.1}(\text{VO})_{0.45}\text{LaTiO}_4$ was carried out by Rietveld methods. The starting model was based on NaLaTiO_4 , where the atomic positions of lanthanum, titanium and oxygen were kept the same except that sodium was replaced with vanadium at $2c (0\ 0\ z)$ with 45 % occupancy. The occupancy for vanadium was maintained constant at 45% during the Rietveld refinement. While this model produced reasonable agreement factors and most of the atoms were well behaved, the vanadium thermal parameter and the χ^2 were unreasonably large. It was found that the relative intensities of 001, 102, 111 and 105 reflections are very sensitive to vanadium position. In the parent, sodium ions are nine coordinated to the neighboring oxygens and the smaller vanadium may not be suitable for such a position.^[4] When the vanadium was moved from the sodium site, $2c$, to $2a (0\ 0\ 0)$, a better fit was obtained. The observed,

calculated and difference plots for the refinement are shown in Figure 2.2 and the structural information is provided in Table 2.2. Selected bond distances are presented in Table 2.3. Although this model seemed to accommodate vanadium much better, the thermal parameter for vanadium is still rather high ($U_{\text{iso}} = 0.39$). On disordering vanadium over the two sites, 2a and 2c, the thermal parameters showed no significant improvement. A more general position 8i, (0 y z), was also examined, this showed only a slight reduction in the vanadium thermal parameter ($U_{\text{iso}} = 0.33$). It is worth noting that no matter where the vanadium was positioned, all of the other atoms in the crystal structure were well behaved. These results indicate that the vanadyl unit is likely disordered between the perovskite layers, possibly over several sites.

Table 2.1 Refined unit cell parameters for NaLaTiO_4 and $\text{Na}_{0.1}(\text{VO})_{0.45}\text{LaTiO}_4$.

Compounds	Unit cell parameters		Cell volume
	a (Å)	c (Å)	V (Å ³)
NaLaTiO_4 this work	3.7730(1)	13.0220(2)	185.37
$\text{Na}_{0.1}(\text{VO})_{0.45}\text{LaTiO}_4$	3.7197(4)	12.2973(2)	170.14

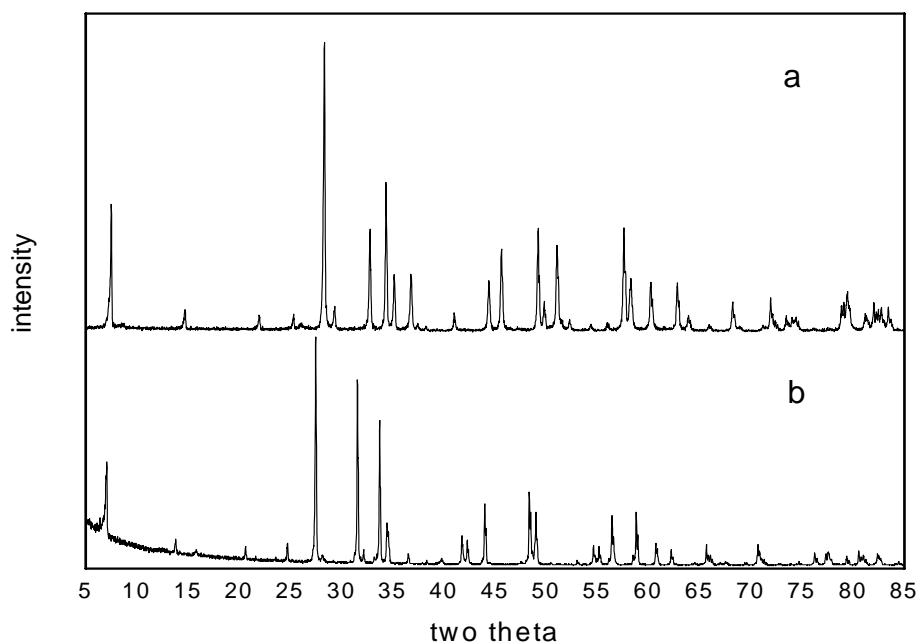


Figure 2.1 Powder X-ray diffraction patterns for (a) NaLaTiO_4 and (b) $\text{Na}_{0.1}(\text{VO})_{0.45}\text{LaTiO}_4$

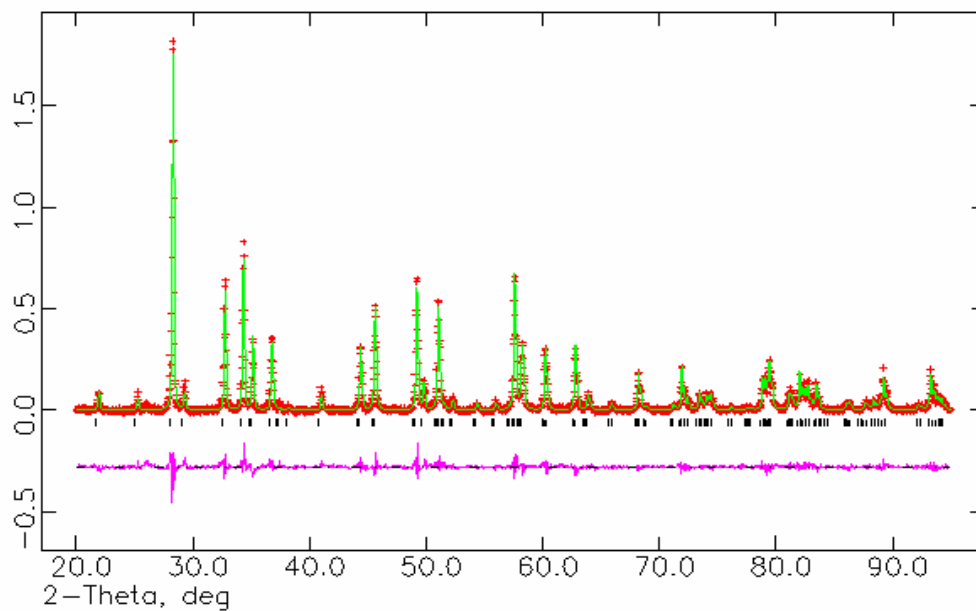


Figure 2.2 Rietveld refinement of $\text{Na}_{0.1}(\text{VO})_{0.45}\text{LaTiO}_4$. Observed data is indicated with crosses, calculated pattern as a solid line, and the difference is indicated at the bottom.

Table 2.2 Crystallographic data for Na_{0.1}(VO)_{0.45}LaTiO₄^a

Atom	Site	x	y	z	g	U _{iso}
La	2c	0.75	0.75	0.3815(1)	1.001(2)	0.012(2)
Ti	2c	0.75	0.75	0.2031(2)	1.030(7)	0.016(1)
O 1	4f	0.75	0.25	0.7596(6)	0.990(2)	0.026(3)
O 2	2c	0.75	0.75	0.5821(1)	1.040(2)	0.015(3)
O 3	2c	0.75	0.75	0.9426(1)	1.070(2)	0.028(3)
V	2a	0.25	0.75	0.0000	0.45	0.390(1)

^a P4/nmm (2nd choice of origin); Z = 2, R_p = 11.91 %, R_{wp} = 16.13 %, χ^2 = 1.599, R_F² = 5.906 %.

Table 2.3 Selected bond distances for Na_{0.1}(VO)_{0.45}LaTiO₄.

Bond	Length (Å)
La – O1(x 4)	2.540(3)
La – O2(x 4)	2.667(3)
La – O2(x 1)	2.460(3)
Ti – O1(x 4)	1.914(2)
Ti – O2(x 1)	2.637(6)
Ti – O3(x 1)	1.797(6)
V – O3(x 4)	1.989(6)

2.3.3. Thermal Analysis

The stability of $\text{Na}_{0.1}(\text{VO})_{0.45}\text{LaTiO}_4$ was studied as a function of temperature in oxygen, argon and hydrogen. The material loses weight in inert atmosphere from room temperature up to 130 °C. This was attributed to the presence of water in the interlayer. Thermogravimetric analysis showed that the sample is hydrated with approximately 0.6 water molecules per formula unit. Similar behavior was observed in the case of the triple layered Ruddlesden-Popper compound, $(\text{VO})\text{La}_2\text{Ti}_3\text{O}_{10}$.^[3] Above 200 °C, $\text{Na}_{0.1}(\text{VO})_{0.45}\text{LaTiO}_4$ starts to degrade. XRD shows that LaVO_4 starts to form around 460 °C and at 700 °C constitutes the predominant phase (Figure 2.3). The same behavior was observed in oxidizing atmosphere. In reducing atmosphere, the material starts the formation of LaVO_3 above 220 °C, and this is the predominant phase up to 800 °C (Figure 2.4).

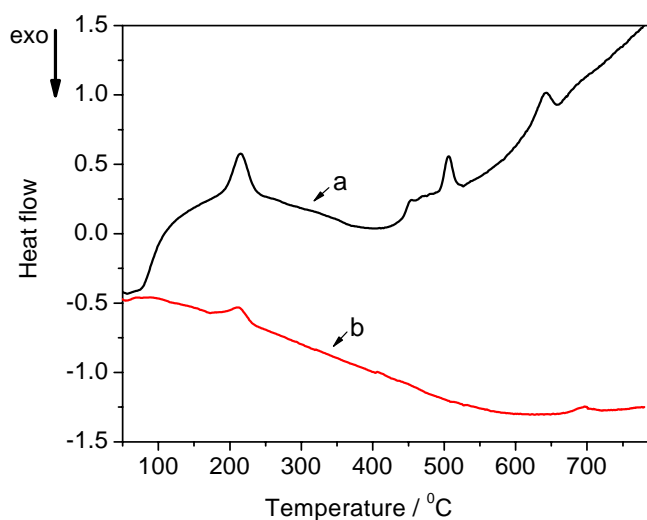


Figure 2.3 The DSC curves for $(\text{Na}_{0.1}\text{VO}_{0.45})\text{LaTiO}_4$ in a) oxygen and b) argon.

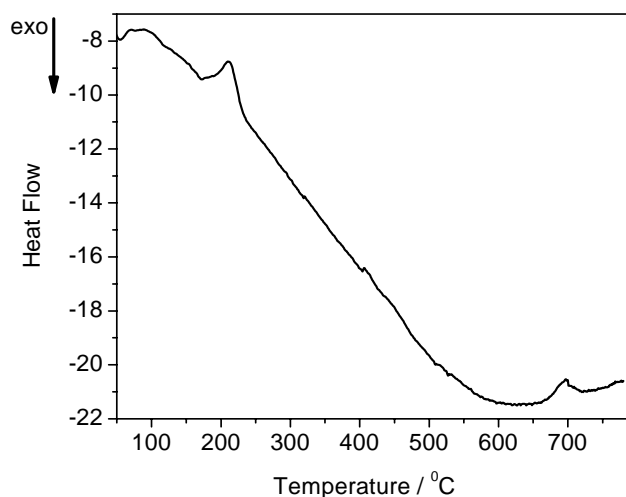


Figure 2.4 The DSC curve for $(\text{Na}_{0.1}\text{VO}_{0.45})\text{LaTiO}_4$ in hydrogen.

2.3.4. IR Data

The presence of the VO unit in the structure is supported by the IR spectra, which show the characteristic stretching band at around 1012 cm^{-1} . This is in agreement with the accepted range for a vanadyl stretch, $950 - 1035\text{ cm}^{-1}$.^[12] A comparable value was observed in the triple layered RP $(\text{VO})\text{La}_2\text{Ti}_3\text{O}_{10}$.^[5] IR also supports the presence of water in $\text{Na}_{0.1}(\text{VO})_{0.45}\text{LaTiO}_4$, showing the corresponding stretching bands of water around 1600 and 3400 cm^{-1} .

2.3.5. EPR and Magnetic Data

EPR data for the $\text{Na}_{0.1}(\text{VO})_{0.45}\text{LaTiO}_4$ exhibit a single resonance with a g value of around 2 (Figure 2.5). Magnetic susceptibility data for the compound are shown in Figure 2.6. Measurements were performed in a field of 1000 Oe as a function of temperature. The compound is paramagnetic above 140 K and exhibits Curie-Weiss

behavior (Figure 2.3, inset). The Curie-Weiss constant and magnetic moment calculated from the fitted data are $\theta = -126$ K and $\mu_{\text{eff}} = 1.72 \mu_{\text{B}}$ per formula unit of $\text{Na}_{0.1}(\text{VO})_{0.45}\text{LaTiO}_4$, respectively. The magnetic moment is in agreement with a spin-only magnetic moment expected for V^{4+} (d^1) in a $(\text{VO})^{2+}$ unit.^[13] It can be noted that a small reproducible inflection in the susceptibility is observed at around 50 K.

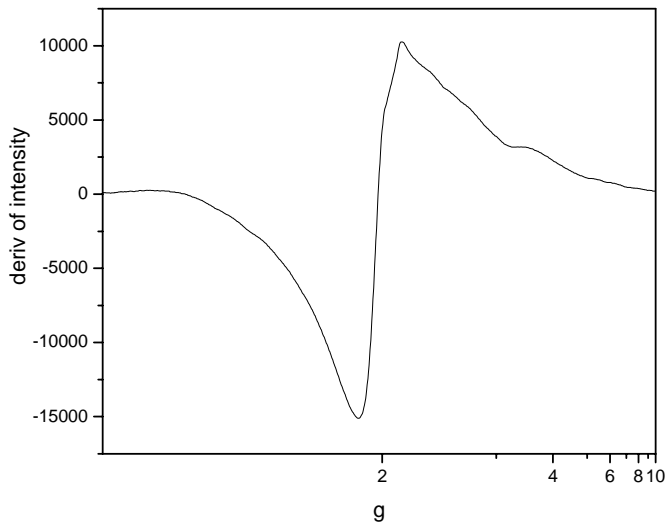


Figure 2.5 EPR spectra for $\text{Na}_{0.1}(\text{VO})_{0.45}\text{LaTiO}_4$.

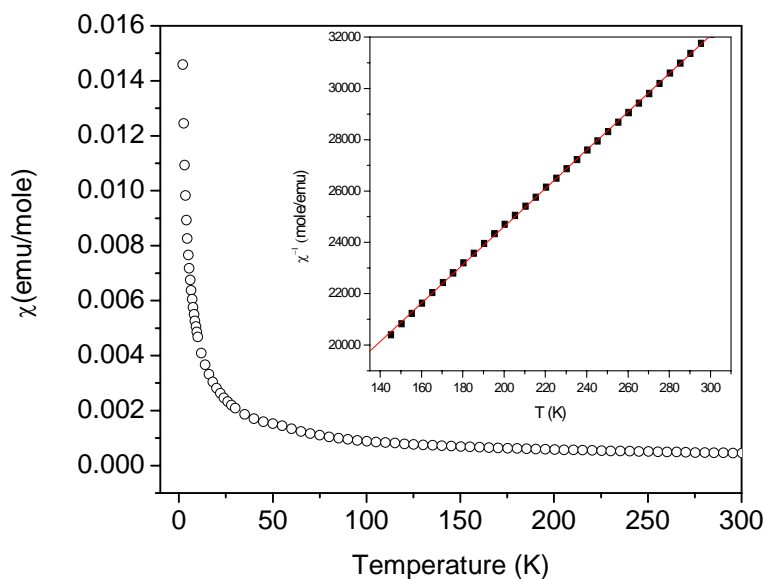


Figure 2.6 Temperature dependence of magnetic susceptibility at 1000 Oe, only ZFC curve is shown (ZFC/FC are identical). The inset represents the reciprocal susceptibility versus temperature in the range 140–300 K and the solid line is the result of the linear fit.

2.4 Discussion

The composition of the ion exchanged material was found to be $\text{Na}_{0.1}(\text{VO})_{0.45}\text{LaTiO}_4$. Complete ion exchange to lead to $(\text{VO})_{0.5}\text{LaTiO}_4$ was not observed even if the reaction time was prolonged and/or the molar ratio parent to vanadyl sulfate was increased. This upper limit in ion exchange may be related to a decrease in the interlayer spacing between perovskite slabs. As the layer distance decreases, it becomes more difficult for cations to enter and exit. In contrast, the complete ion exchange of transition metals to make $\text{M}_{0.5}\text{LaTiO}_4$ ($\text{M} = \text{Co}, \text{Cu}, \text{Zn}$) readily occurred.^[6] These reactions however were made at higher temperatures ($\geq 300^\circ\text{C}$) and the smaller size of the metal cations relative to the vanadyl unit may help favor complete exchange. It is

worth noting that incomplete exchange reactions (~90%) were observed in the replacement of sodium with calcium in NaLaTiO_4 ; while this reaction was carried out at temperatures similar to the transition metal reactions, the larger calcium cation might also have limited the degree exchange.^[14]

Thermal analysis shows that $\text{Na}_{0.1}(\text{VO})_{0.45}\text{LaTiO}_4$ is a low temperature phase. The compound loses water from room temperature to 130 °C, and above 200 °C starts degrading. The changes seen above 200 °C can be attributed to the instability of V^{4+} versus V^{5+} with increasing temperature. At 800 °C, LaVO_4 is the predominant crystalline phase in both inert and oxidizing atmospheres.

The IR stretching frequency of the vanadium oxygen double bond is 1012 cm^{-1} which is comparable with 1010 cm^{-1} found in $(\text{VO})\text{La}_2\text{Ti}_3\text{O}_{10}$.^[3] In both of these vanadyl substituted RP perovskites, the possibility of having $\text{V}=\text{O}---\text{V}=\text{O}$ chains can be ruled out.^[12] These kind of chains are often present in nonmolecular vanadyls such as VOSO_4 , $(\text{VO})_3(\text{PO}_4)_2$, VOMoO_4 , $(\text{VO})_2\text{P}_2\text{O}_7$, $(\text{VO})(\text{salen})$ and some organometallic phases.^[12, 15, 16] Usually the stretching frequency of the $\text{V}=\text{O}$ bond in these compounds is below 950 cm^{-1} . The absence of the vanadium oxygen chains in $\text{Na}_{0.1}(\text{VO})_{0.45}\text{LaTiO}_4$, as indicated by the IR frequency is consistent with a lack of order within the vanadyl layer. At the same time, this wavenumber is an indication of the retention of the strong double bond character within vanadyl $\text{V}-\text{O}$ bond.^[17] From the IR spectra water bands have also been seen; the presence of water is not unexpected since the reactions are carried out in aqueous solution. Further the vanadyl, $(\text{VO})\text{La}_2\text{Ti}_3\text{O}_{10}$, also forms a hydrate.

It was expected that the oxidation state of the d^1 vanadium (V^{4+}) cation in the vanadyl would be maintained on formation of $\text{Na}_{0.1}(\text{VO})_{0.45}\text{LaTiO}_4$. EPR studies on

isolated V^{4+} cations typically exhibit hyperfine structure (an octet) resulting from the interaction of the free electron with the magnetic nuclear moment of ^{51}V ($I = 7/2$). This behavior is observed in other vanadium oxides.^[12] The absence of a hyperfine structure and the presence of a broad signal in the EPR spectra centered on $g \approx 2$ is a characteristic of a V^{4+} in a dipolar interaction with the other vanadium ions present in the structure. This means that the vanadium ions in the structure are close enough to cause these dipolar interactions to suppress the hyperfine structure and make the EPR signal rather broad. Both room temperature electron resonance and magnetic data suggest that the vanadyl unit has a localized, non-interacting “free spin” electron. From the magnetic susceptibility data it can be seen that the susceptibility increases at lower temperatures with a very broad maximum around 50 K and a negative Weiss constant of $\theta = -126$ K. Similar behavior has been observed in other layered perovskites and is associated with antiferromagnetic interactions.^[18-20] Apparently, in spite of the low loading of vanadyl units ($V:Ti = 0.45:1.0$), weak magnetic coupling still occurs.

2.5 Conclusions

Ion exchange of vanadyl units is an effective method for co-inserting both vanadium cation and oxygen anion species. Though in this case isolated vanadyl anions were only observed, a similar approach might allow one to produce extended metal oxide layers into receptive hosts. The ability to create such layers might allow one to rationally direct the formation of technologically significant materials.

2.6 References

- [1] Toda, Kenji; Watanabe, Jun; Sato, Mineo, *Materials Research Bulletin* **1996**, 31(11), 1427.
- [2] Hyeon, Ki-An; Yoon, J. J.; Lee, S. O. *Solid State Chem.* **1996**, 127, 119.
- [3] Gopalakrishnan, J.; Sivakumar, T.; Ramesha, K.; Thangadurai, V.; Subanna, G. N. *J. Am. Chem. Soc.* **2000**, 122, 6237.
- [4] Kim, S. Y.; Oh, J. M.; Park, J. C.; Byeon, S. H. *Chem. Mater.* **2002**, 14, 1643.
- [5] Schaak R. E. and Mallouk, T. *J. Solid State Chemistry* **2001**, 161, 225.
- [6] Toda, K.; Kurita, S.; Sato, M. *Solid State Ionics* **1995**, 81, 267.
- [7] Blasse, G. *J. Inorg. Nucl. Chem.* **1968**, 30, 656.
- [8] Toda, K.; Kameo, Y.; Kurita, S.; Sato, M. *Journal of Alloys and Compounds* **1996**, 19, 234.
- [9] A. Larson, R. B. Von Dreele, GSAS: Generalized Structure Analysis System, Los Alamos National Laboratory: Los Alamos NM, **1994**.
- [10] Le Bail, A.; Duroy and Fourquet, *Mater. Res. Bull.* **1988**, 23 447.
- [11] Schaak, R. E.; Mallouk, T. E. *Chem. Mater.* **2000**, 12, 3427.
- [12] F. A. Cotton, G. Wilkinson, C.A. Murillo, M. Bochmann, *Advanced Inorganic Chemistry*, 6th Edition, Wiley and Sons Inc., **1999**.
- [13] Charles J. O'Connor, *Magnetochemistry - advances in theory and experimentation. Progress in Inorganic Chemistry* **1982**, 29, 203.
- [14] McIntyre, R. A.; Falster, A. U.; Sichu Li; Simmons, W. B.; O'Connor, C. J. and Wiley, J. B. *J. Am. Chem. Soc.* **1998**, 120, 217.

- [15] Lezama, L.; Villeneuve, G.; Marcos, M. D; Pizzaro, .J. L.; Haggemuller, P. *Solid State Communications* **1989**, 70, 899.
- [16] Shiozaki, I. *J. Phys Condens. Matter*, **1998**, 10, 9813.
- [17] Blasse, G.; Van Den Heuvel, G. P. M. *J. Solid State Chem.* **1974**, 10, 206.
- [18] Kodenkandath, T. A.; Lalena, J. N.; Weillie, L. Z.; Falster, A. U.; Carpenter, E. E.; Sangrerio, C.; Simmons, W. B., O'Connor, C. J. and Wiley, J. B *J. Am. Chem. Soc.* **1999**, 121,46.
- [19] Viciu, L.; Golub, V. O.; Wiley, J. B. *J. Solid State Chemistry* **2003**, 175, 88.
- [20] Viciu, L.; Koenig, J.; Spinu, L.; Zhou, W. L.; Wiley, J. B. *Chem. Mater.* **2003**, 7, 1480.

Chapter 3

The Structure and Properties of Mixed Valence Titanates, $(\text{Li}_x\text{VO})\text{La}_2\text{Ti}_3\text{O}_{10}$

3.1 Introduction

Layered perovskites such as Aurivillius phases, Dion-Jacobson and Ruddlesden-Popper compounds can intercalate alkali metal ions into their interlayer galleries. The insertion of these cations takes place in a topotactic manner where the basic structure is maintained. Choy et al.^[1], for example, have shown that the intercalation of Li in the Aurivillius phase, $\text{Bi}_4\text{Ti}_3\text{O}_{10}$, leads to $\text{Li}_2\text{Bi}_4\text{Ti}_3\text{O}_{10}$ with retention of the parent structure. Armstrong and Anderson^[2] have demonstrated a very elegant transformation on rubidium intercalation of $\text{RbLaNb}_2\text{O}_7$ to produce $\text{Rb}_2\text{LaNb}_2\text{O}_7$. In this system, the perovskite layers persist, while overall the compound is converted from the Dion-Jacobson structure type to Ruddlesden-Popper. Such reductive intercalation reactions are important for tuning the valency, and therefore the electronic and magnetic properties. For example, the mixed valence tantalate, $\text{Na}_2\text{Ca}_2\text{Ta}_3\text{O}_{10}$, can be obtained by reacting $\text{NaCa}_2\text{Ta}_3\text{O}_{10}$ with NaN_3 ,^[3,4] and similar intercalation reactions in the niobates to produce $\text{Li}_x\text{KCa}_2\text{Nb}_3\text{O}_{10}$ have been reported to produce superconductivity.^[5] The reductive intercalation method has also been extended to the oxysulfides, $\text{Y}_2\text{Ti}_3\text{O}_5\text{S}_2$.^[6] In these materials, the insertion of Na and Li lead to metallic properties. In our group it has been shown that using a two-step low temperature route (ion exchange and then reductive intercalation), mixed valence compounds with semiconducting behavior, such as $\text{Na}_{1-x+y}\text{Ca}_{x/2}\text{LaTiO}_4$ and $\text{Na}_{2-x+y}\text{Ca}_{x/2}\text{La}_2\text{Ti}_3\text{O}_{10}$, can be obtained.^[7,8]

Herein we describe the influence of lithium intercalation chemistry upon structure, electronic and magnetic properties of the triple layered Ruddlesden-Popper perovskite,

(VO)La₂Ti₃O₁₀. This compound was prepared from the triple layered Ruddlesden–Popper perovskite, K₂La₂Ti₃O₁₀,^[9] by ion exchange with the a divalent vanadyl (VO²⁺) unit.^[10] Similar to other divalent ion exchanges,^[7,8] this reaction opens the structure to further chemistry; two potassium ions are replaced by a vanadyl and a vacancy. Alkali metal ions can then be inserted on the sites left vacant by the ion exchange step. This paper presents a detailed description of the synthesis and characterization of this new series of compounds.

3.2 Experimental

3.2.1 Synthesis

The parent, K₂La₂Ti₃O₁₀, was prepared by a solid state reaction from K₂CO₃ (Alfa Aesar 99.997%), La₂O₃ (Alfa Aesar 99.99%), and TiO₂ (Alfa Aesar 99.995%) mixed in stoichiometric amounts.^[5] A 30% excess of K₂CO₃ was used to compensate for the loss due to volatilization. The reaction was performed in air at 550 °C for 12 hours and then at 1050 °C for 6 hours. Phase purity for K₂La₂Ti₃O₁₀ was confirmed by X-ray powder diffraction (XRD). The powder pattern was indexed in a tetragonal unit cell, $a = 3.876(1) \text{ \AA}$ and $c = 29.824(1) \text{ \AA}$, which is in agreement with literature values.^[9]

Ion exchange was used to substitute the K⁺ ions in K₂La₂Ti₃O₁₀ with vanadyl ions, (VO)²⁺.^[10] The source of the vanadyl unit was vanadyl sulfate hydrate (VOSO₄·nH₂O, Alfa Aesar, 99.99%). K₂La₂Ti₃O₁₀ was mixed in a 1:2 molar ratio with VOSO₄ in 100 ml water. The solution was heated under reflux for five days at 100 °C with continuous stirring. Phase purity for (VO)La₂Ti₃O₁₀ was confirmed by X-ray powder diffraction (XRD). The powder pattern was

indexed with tetragonal cell parameters, $a = 3.809(2) \text{ \AA}$ and $c = 27.410(1) \text{ \AA}$; these values are consistent with those in the literature.^[10]

Lithium intercalation was performed by reacting $(\text{VO})\text{La}_2\text{Ti}_3\text{O}_{10}$ and n-butyllithium (Aldrich 1.6 M in hexanes) in different molar ratios (1:1, 1:2 and 1:3) in inert atmosphere at 60 °C for three days. The final products were washed with anhydrous hexanes under Ar and then dried under vacuum. The intercalated samples have colors ranging from brown, for the lowest lithium content, to dark grey for the sample with the highest lithium content.

3.2.2 Characterization

The inductively coupled plasma emission spectroscopy (ICP) analysis was performed to determine lithium contents. The samples were dissolved in concentrated nitric acid. Standard solutions were prepared from Specpure Alfa Aesar 10,000 $\mu\text{g/ml}$ for lithium. All the standards and the samples were analyzed in a 5% HNO_3 solution (vol./vol.). The composition of the final products corresponded to the general formula $(\text{Li}_x\text{VO})\text{La}_2\text{Ti}_3\text{O}_{10}$, with $x = 0.83 \pm 0.02$, 1.41 ± 0.02 and 1.81 ± 0.03 .

X-ray powder diffraction studies were carried out on a Philips X'Pert System ($\text{Cu K}\alpha$ radiation $\lambda = 1.5418 \text{ \AA}$) equipped with a graphite monochromator. Data were collected in a continuous scan mode between 5 and 95° 2 θ . The lattice parameters were refined using POLSQ.^[12] Structural refinement of $(\text{Li}_{1.8}\text{VO})\text{La}_2\text{Ti}_3\text{O}_{10}$ was done by the Rietveld method with the GSAS package of programs.^[13] Thirty-nine parameters were varied including background, peak shape, cell, atom positions, and thermal parameters. In the beginning of the refinement, the Le Bail method^[14] was employed for the background and peak shape parameters.

Infrared spectroscopy (IR) was performed on a Perkin Elmer 2000 FT-IR; the samples were analyzed as pellets in a 1:100 molar ratio with dry KBr. For the electron paramagnetic resonance (EPR) measurements, an EMX X-band Bruker spectrometer was used. Magnetic measurements were carried out on a Quantum Design MPMS-5S superconducting quantum interference device (SQUID) magnetometer between 2 and 300 K at 1000 Oe.

3.3 Results

3.3.1 Structure

The intercalation of lithium in $(\text{VO})\text{La}_2\text{Ti}_3\text{O}_{10}$ takes place in a topotactic manner. The tetragonal unit cell shrinks along the c-axis and slightly increases along the a-axis with increasing lithium content.^[11] Figure 3.1 presents the X-ray powder patterns for the parent, $\text{K}_2\text{La}_2\text{Ti}_3\text{O}_{10}$, for the ion exchanged product, $(\text{VO})\text{La}_2\text{Ti}_3\text{O}_{10}$ and the lithium intercalated series $(\text{Li}_x\text{VO})\text{La}_2\text{Ti}_3\text{O}_{10}$. Table 3.1 presents the variation of the unit cell parameters and cell volume for all of the investigated samples. A structure refinement was carried out on $(\text{Li}_{1.8}\text{VO})\text{La}_2\text{Ti}_3\text{O}_{10}$. The observed, calculated and difference plots are shown in Figure 3.2, the atomic positions in Table 3.2, and the bond lengths in Table 3.3. The starting model for the refinement was based on $\text{CuLa}_2\text{Ti}_3\text{O}_{10}$ ($I4/mmm$),^[15] where the starting positions for the atoms were the same except that copper was replaced with vanadium. Lithium was not included in the refinement and the vanadyl oxygen could not be located. From the structure (Figure 3.3), it can be seen that the two-dimensional $[\text{La}_2\text{Ti}_3\text{O}_{10}]$ layers perpendicular to the c-axis are maintained. These layers are now separated by vanadium ions. These vanadiums are tetrahedrally coordinated to the four O3 oxygens from the perovskite sheets. To better understand the

structural changes that accompany the ion exchange and intercalation respectively, from $\text{K}_2\text{La}_2\text{Ti}_3\text{O}_{10}$ to $(\text{VO})\text{La}_2\text{Ti}_3\text{O}_{10}$ and finally to $(\text{Li}_x\text{VO})\text{La}_2\text{Ti}_3\text{O}_{10}$, IR spectroscopy has been employed. The IR spectra for the potassium and vanadyl precursors along with the lithium intercalated sample (only one of them is presented because they all look similar) are shown in Figure 3.4. There are three stretching frequencies corresponding to Ti-O bonds in $\text{K}_2\text{La}_2\text{Ti}_3\text{O}_{10}$ located at 580 cm^{-1} , 720 cm^{-1} and 900 cm^{-1} . In the vanadyl ion exchanged sample, the titanium-oxygen stretch at 900 cm^{-1} vanishes and another one at 1020 cm^{-1} corresponding to $\text{V}=\text{O}$ appears. In the intercalated materials, the vanadyl stretch at 1020 cm^{-1} disappears and another at 865 cm^{-1} appears. This could be an indication of V-O-V chains forming in the interlayer space between the perovskite strata. [9, 10]

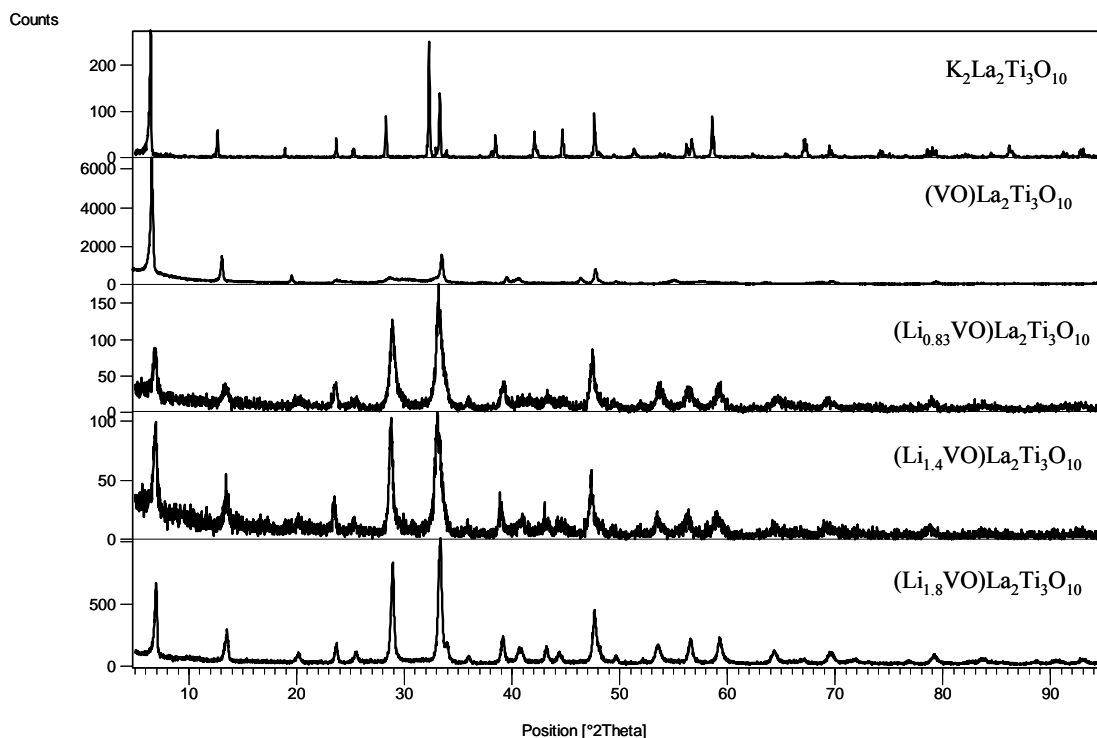


Figure 3.1 X-ray powder pattern for: $\text{K}_2\text{La}_2\text{Ti}_3\text{O}_{10}$; $(\text{VO})\text{La}_2\text{Ti}_3\text{O}_{10}$; $(\text{Li}_{0.83}\text{VO})\text{La}_2\text{Ti}_3\text{O}_{10}$; $(\text{Li}_{1.4}\text{VO})\text{La}_2\text{Ti}_3\text{O}_{10}$; and $(\text{Li}_{1.8}\text{VO})\text{La}_2\text{Ti}_3\text{O}_{10}$.

Table 3.1 Cell parameters based on a tetragonal symmetry for $\text{K}_2\text{La}_2\text{Ti}_3\text{O}_{10}$, $(\text{VO})\text{La}_2\text{Ti}_3\text{O}_{10}$ and the series $(\text{Li}_x\text{VO})\text{La}_2\text{Ti}_3\text{O}_{10}$.

Compound	a (Å)	c (Å)	V (Å ³)
$\text{K}_2\text{La}_2\text{Ti}_3\text{O}_{10}$	3.876(1)	29.824(1)	448.0(5)
$(\text{VO})\text{La}_2\text{Ti}_3\text{O}_{10}$	3.809(2)	27.410(1)	397.6(7)
$(\text{Li}_{0.83}\text{VO})\text{La}_2\text{Ti}_3\text{O}_{10}$	3.800(1)	27.134(1)	391.8(1)
$(\text{Li}_{1.4}\text{VO})\text{La}_2\text{Ti}_3\text{O}_{10}$	3.800(2)	26.878(1)	388.1(1)
$(\text{Li}_{1.8}\text{VO})\text{La}_2\text{Ti}_3\text{O}_{10}$	3.813(2)	26.562(1)	386.1(8)

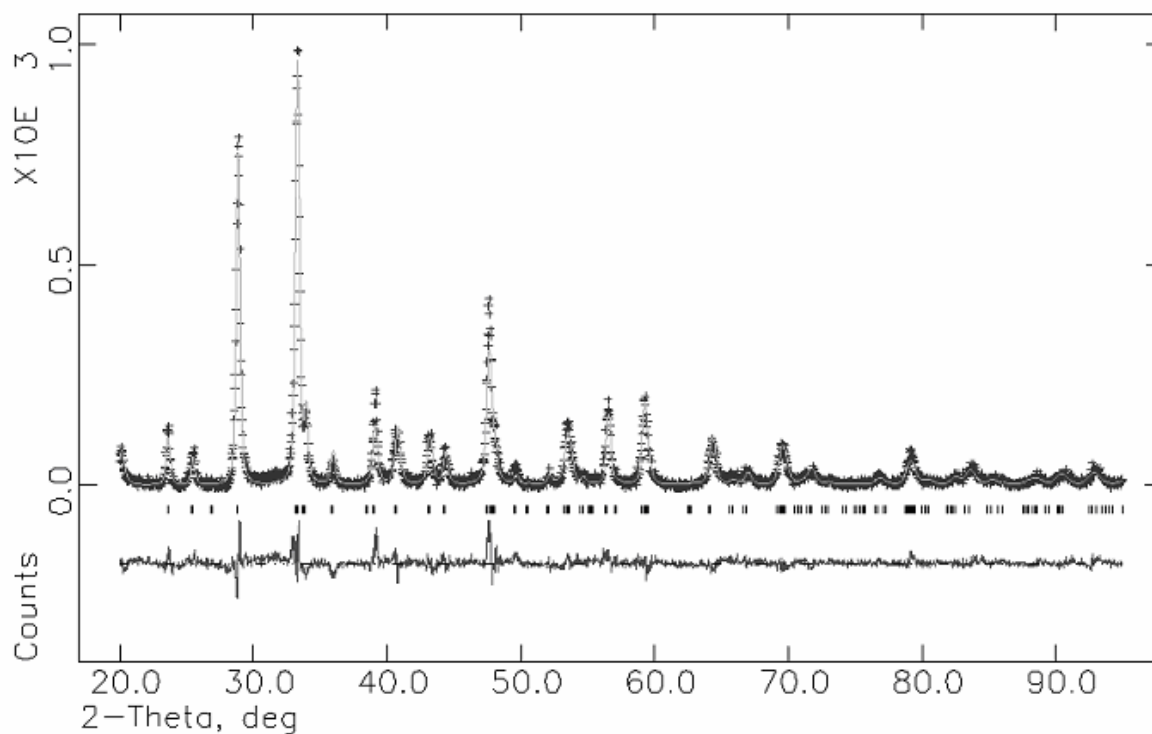


Figure 3.2 Results of Rietveld refinements for the structure of $(\text{Li}_{1.8}\text{VO})\text{La}_2\text{Ti}_3\text{O}_{10}$. The measured (crosses), calculated (line) profiles and the difference (lower line) profiles are shown.

Table 3.2 Crystallographic data for (Li_{1.8}VO)L_a2Ti₃O₁₀

(Li _{1.8} VO)L _a 2Ti ₃ O ₁₀	Atom	Site ^{a)}	g ^{b)}	x	y	z	U _{iso}
I4/mmm (No. 139)	V	4d	0.5	0	0.5	0.2500(0)	0.104(4)
a = 3.8501(1) Å	La	4e	1.0	0	0.0	0.4193(1)	0.022(1)
c = 26.7861(1) Å	Ti 1	2a	1.0	0	0.0	0.0000(0)	0.019(3)
V = 397.05(7) Å ³	Ti 2	4e	1.0	0	0.0	0.1567(2)	0.012(4)
R _{wp} = 18.73 %	O 1	4e	1.0	0	0.0	0.0745(8)	0.012(9)
R _p = 14.19 %	O 2	4c	1.0	0	0.5	0.0000(0)	0.011(8)
R _F = 8.47 %	O 3	4e	1.0	0	0.0	0.2319(5)	0.011(6)
χ ² = 1.802	O 4	8g	1.0	0	0.5	0.1425(1)	0.011(9)

a) Multiplicity and Wyckoff notation; b) Occupancy.

Table 3.3 Selected bond lengths in Å for (Li_{1.8}VO)L_a2Ti₃O₁₀

Bond type	Bond length (Å)
V – O 3 (X4)	1.985(5)
La – O 1 (X4)	2.727(2)
La – O 2 (X4)	2.893(2)
La – O 4 (X4)	2.540(1)
Ti 1 – O 1 (X2)	1.998(3)
Ti 1 – O 2 (X4)	1.925(1)
Ti 2 – O 1 (X1)	2.200(3)
Ti 2 – O 3 (X1)	2.016(2)
Ti 2 – O 4 (X4)	1.966(3)

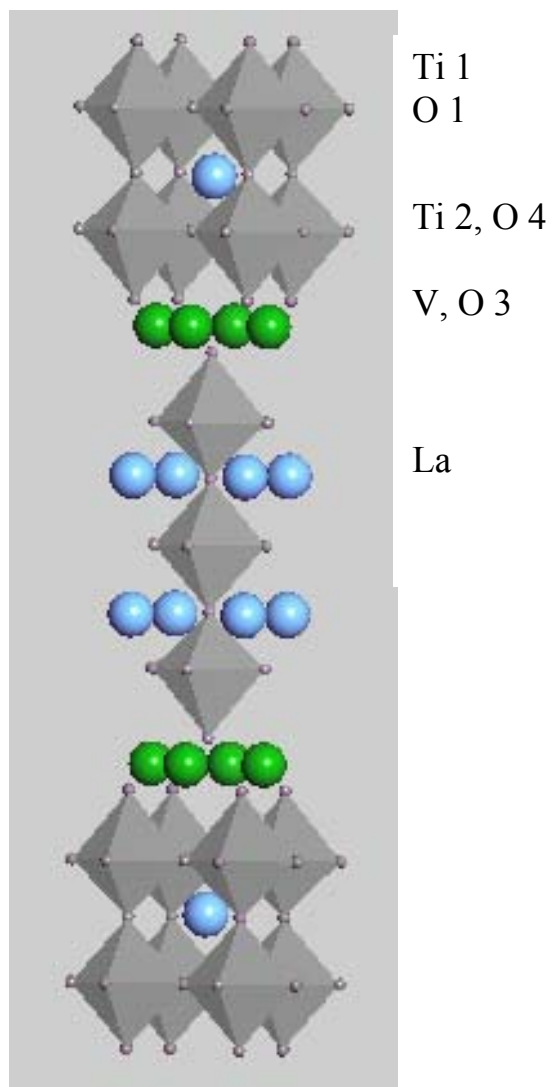


Figure 3.3 The structure of $(\text{Li}_{1.8}\text{VO})\text{La}_2\text{Ti}_3\text{O}_{10}$ showing the perovskite blocks and the vanadium atoms in the interlayer space (lithium atoms are not included).

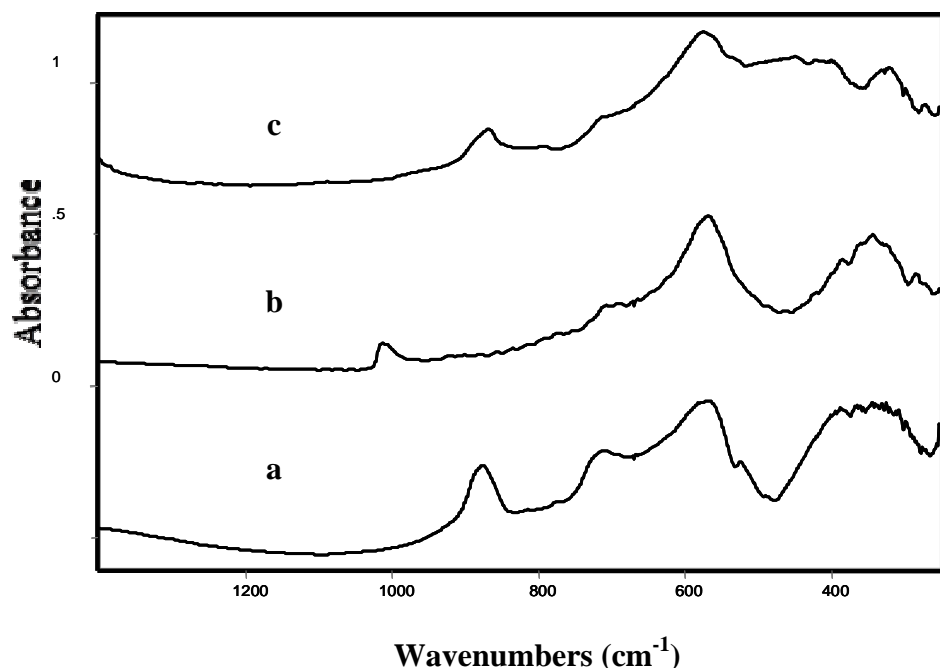


Figure 3.4 IR spectra for: a) $\text{K}_2\text{La}_2\text{Ti}_3\text{O}_{10}$; b) $(\text{VO})\text{La}_2\text{Ti}_3\text{O}_{10}$; c) $(\text{Li}_{1.8}\text{VO})\text{La}_2\text{Ti}_3\text{O}_{10}$. The samples were analyzed as pellets in a 1:100 molar ratio with dry KBr.

3.3.2 EPR and Magnetic Measurements

Electron spin resonance signals for both $(\text{VO})\text{La}_2\text{Ti}_3\text{O}_{10}$ and $(\text{Li}_x\text{VO})\text{La}_2\text{Ti}_3\text{O}_{10}$ are presented in Figure 3.5. EPR data for the $(\text{VO})\text{La}_2\text{Ti}_3\text{O}_{10}$ displays a single broad resonance with $g = 1.97\text{--}1.99$. This is attributed to an electron localized on the vanadium atom. For the lithium intercalated samples, a sharp peak is superimposed on the broad vanadyl signal. The resonance for this peak is at a g value of 2.00. The shape and the g factor suggest the presence of a delocalized electron in the intercalated samples.^[10]

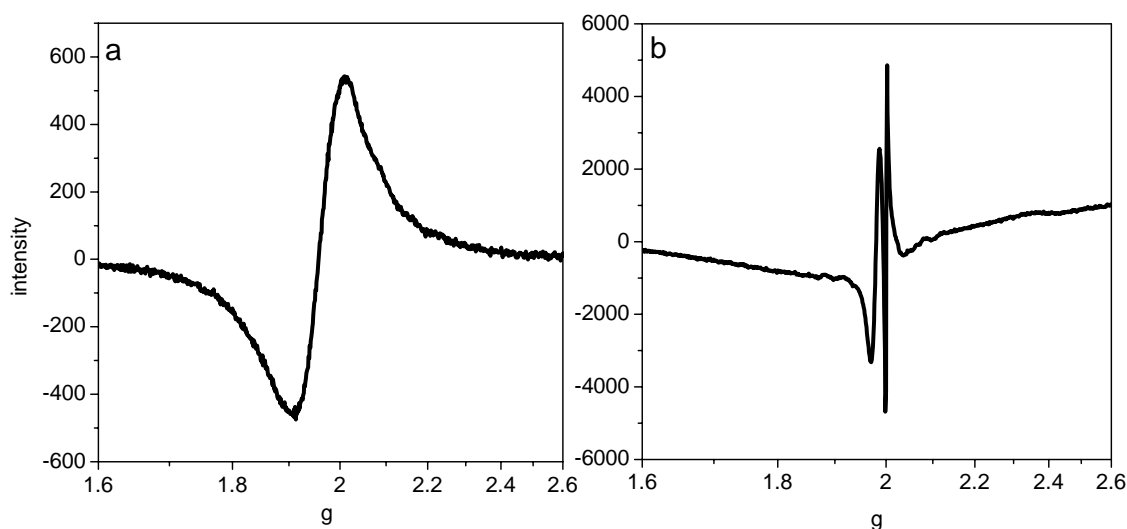


Figure 3.5 X-band EPR spectra for a) $(\text{VO})\text{La}_2\text{Ti}_3\text{O}_{10}$ and b) $(\text{Li}_{1.8}\text{VO})\text{La}_2\text{Ti}_3\text{O}_{10}$.

Magnetic measurements on the intercalated samples show that $(\text{Li}_x\text{VO})\text{La}_2\text{Ti}_3\text{O}_{10}$ with $x = 0.83$ and 1.4 are paramagnetic at room temperature and exhibit a Curie–Weiss behaviours. $(\text{Li}_{1.8}\text{VO})\text{La}_2\text{Ti}_3\text{O}_{10}$ instead is magnetically ordered over the whole studied temperature range. The magnetic susceptibilities as a function of temperature are shown in Figures 3.6a-c. Zero-field-cooled (ZFC) and field-cooled (FC) data are represented. The insets of Figures 3.6a and 3.6b show the linear fit of inverse susceptibility versus temperature. The calculated magnetic moment increases with increasing lithium content (Table 3.4). In Figure 3.6d the hysteresis loops at 50 K and 300 K for $(\text{Li}_{1.8}\text{VO})\text{La}_2\text{Ti}_3\text{O}_{10}$ are presented. For low lithium content, $x = 0.83$ and 1.4 , paramagnetic behavior is observed. The highest lithium content, $x = 1.81$, exhibits magnetic order.

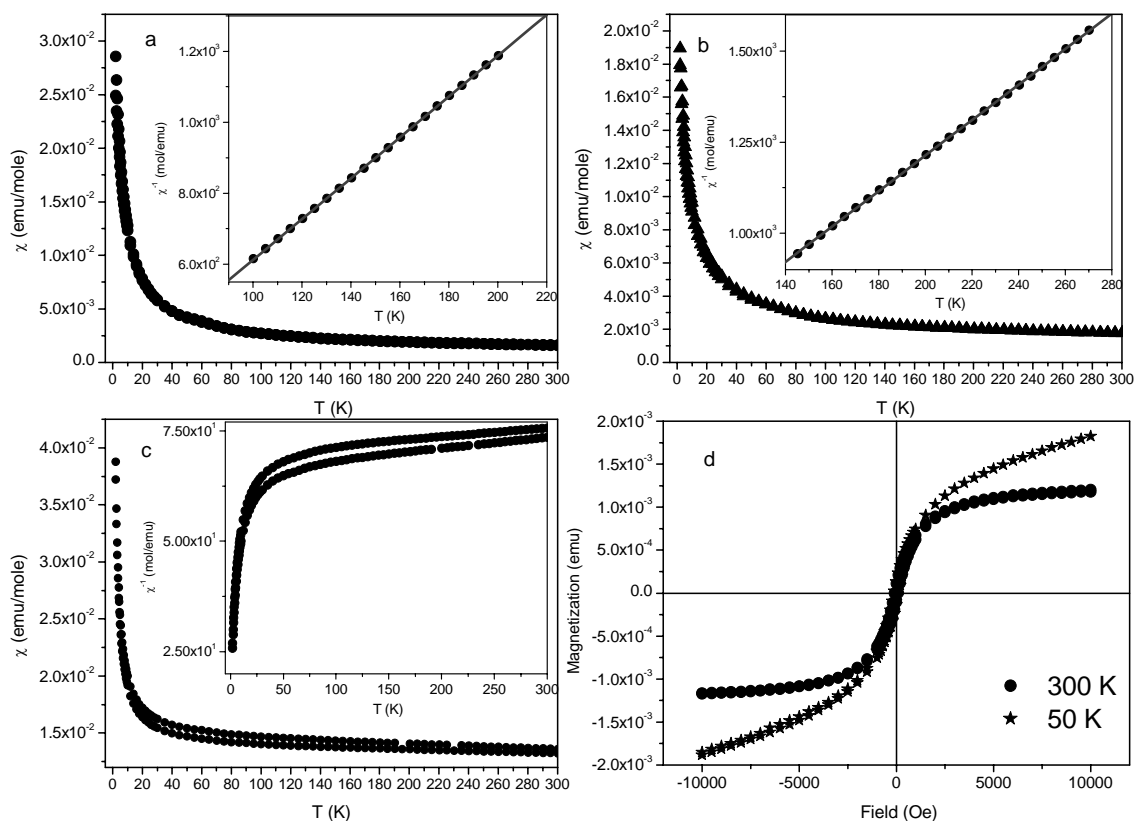


Figure 3.6 The magnetic susceptibilities as a function of temperature for: a) $(\text{Li}_{0.83}\text{VO})\text{La}_2\text{Ti}_3\text{O}_{10}$, b) $(\text{Li}_{1.4}\text{VO})\text{La}_2\text{Ti}_3\text{O}_{10}$ and c) $(\text{Li}_{1.8}\text{VO})\text{La}_2\text{Ti}_3\text{O}_{10}$. The insets represent the linear fit for the reciprocal susceptibility versus temperature curves. d) The hysteresis loops at 50 and 300 K for $(\text{Li}_{1.8}\text{VO})\text{La}_2\text{Ti}_3\text{O}_{10}$.

3.3.3 Band Structure Calculations

The changes that lithium content causes in $(\text{Li}_x\text{VO})\text{La}_2\text{Ti}_3\text{O}_{10}$ have been also followed by extended Hückel calculations performed using the YAEHMOP software package. Parameters are listed in Table 3.5.^[16]

Table 3.5 Orbital parameters used in the YAEHMOP calculations.

Atom	Orbital	H_{ii} (eV)	ξ_{11}	c_1	ξ_{12}	c_2
Ti	4s	-8.970	1.075			
	4p	-5.440	1.075			
	3d	-10.81	4.550	0.4206	1.4000	0.7839
V	4s	-8.810	1.300			
	4p	-5.520	1.300			
	3d	-11.000	4.750	0.4755	1.7000	0.7839
La	6s	-7.670	2.140			
	6p	-5.010	2.080			
	5d	-8.210	3.780	0.7765	1.3810	0.4586
O	2s	-32.30	2.275			
	2p	-14.80	2.275			

The three-dimensional band structures and the corresponding density of states (DOS) diagram are presented in Figures 3.7 and 3.8, respectively. The valence band is mainly occupied by oxygen states with approximately 10 % mixing of titanium states. The states at, and slightly above the Fermi level are antibonding combinations, π^* , resulting from the mixing of titanium t_{2g} with O 2p states and σ combinations and, from vanadium e_g orbitals with O 2sp states. The high-energy states around -6 eV, that correspond to La and V 4s, remain unoccupied. Lithium s states were considered very high in energy, as lithium donates its electron to the layered perovskite sheets and therefore lithium has not been included in the calculations. The intercalated electrons have been considered, according to the lithium content obtained from the ICP data.

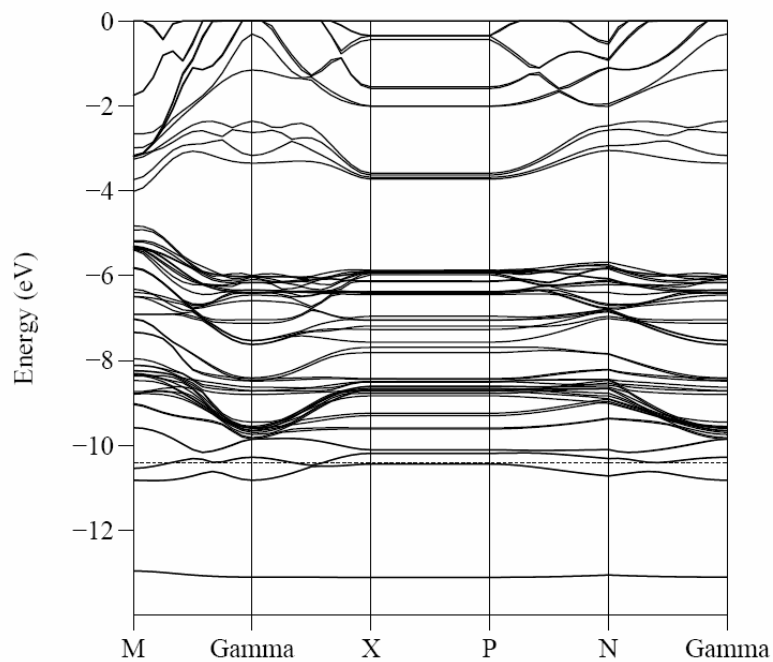


Figure 3.7 Band structure for $(\text{Li}_{1.8}\text{VO})\text{La}_2\text{Ti}_3\text{O}_{10}$. The Fermi level is indicated by the dashed horizontal line at -10.4118 eV.

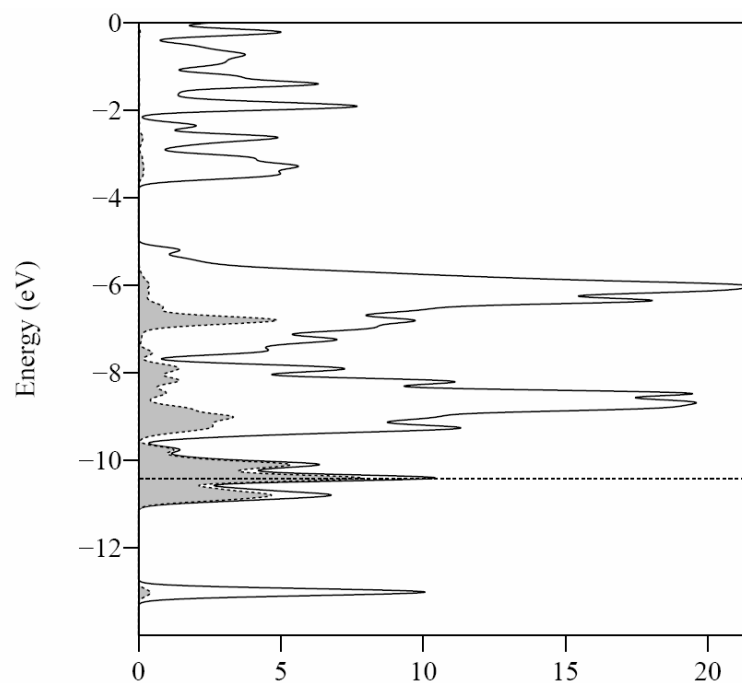


Figure 3.8 The density of states (DOS) for $(\text{Li}_{1.8}\text{VO})\text{La}_2\text{Ti}_3\text{O}_{10}$. The Fermi level is indicated by the dashed horizontal line at -10.4118 eV. The total DOS are represented by a solid line. The grey area represents vanadium and titanium DOS.

3.4 Discussion

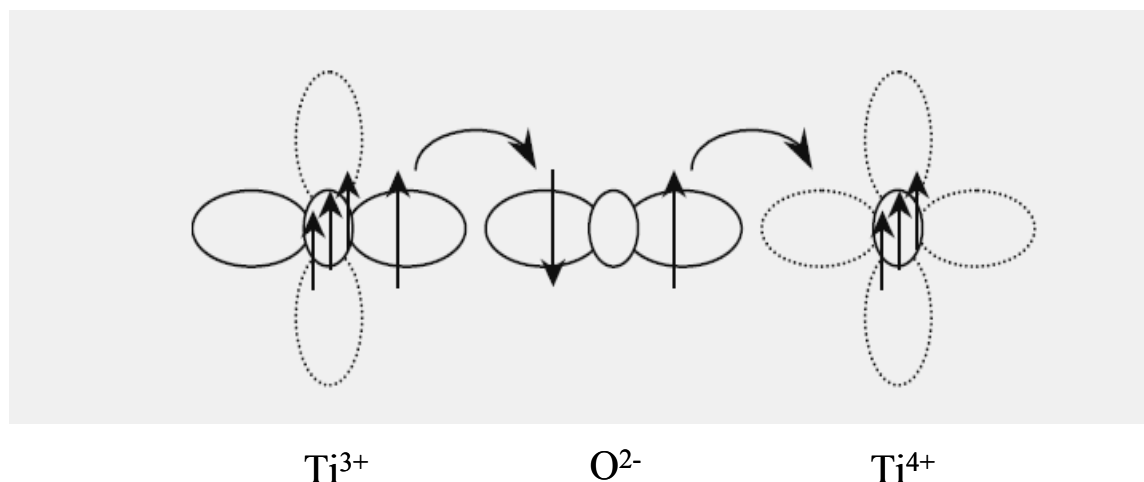
The structure of $(\text{Li}_{1.8}\text{VO})\text{La}_2\text{Ti}_3\text{O}_{10}$ is related to the structure of the parent, however two important differences can be noted. First, in the interlayer space between the perovskite blocks, vanadium is tetrahedrally coordinated with respect to the oxygens from the perovskite layers (see Figure 3.2). Upon intercalation, IR data shows the shift of the vanadyl stretch from 1020 cm^{-1} to 865 cm^{-1} . This change is associated with a lengthening of the vanadyl oxygen bond and it may be attributed to the formation of $\text{V} - \text{O} - \text{V}$ chains in the ab plane.^[18,19] IR data indicates that for $(\text{VO})\text{La}_2\text{Ti}_3\text{O}_{10}$, the vanadyl units are isolated with a very strong $\text{V} = \text{O}$ bond (1020 cm^{-1}) and the electron from V^{4+} (d^1) is localized on vanadium atom. For $(\text{Li}_{1.8}\text{VO})\text{La}_2\text{Ti}_3\text{O}_{10}$, the vanadyl units are connected to each other via $\text{V} - \text{O} - \text{V}$ chains, as the $\text{V} = \text{O}$ stretch shifts to lower wavenumbers (865 cm^{-1}).^[19] It can, then be inferred that when lithium is intercalated into the interlayer space it coordinates to the vanadyl oxygen, which consequently leads to a weakening of the vanadium oxygen bond.

Interestingly, ion exchange of $\text{K}_2\text{La}_2\text{Ti}_3\text{O}_{10}$ with vanadyl produces what appears to be a highly disordered compound,^[10,11] $(\text{VO})\text{La}_2\text{Ti}_3\text{O}_{10}$, and as the degree of intercalation increases, the compound regains its long range order.^[11] The poor crystallinity of the $(\text{VO})\text{La}_2\text{Ti}_3\text{O}_{10}$ prohibited structural refinement for this compound. However, the addition of lithium, apparently reestablishes order, allowing Rietveld refinement of $(\text{Li}_{1.8}\text{VO})\text{La}_2\text{Ti}_3\text{O}_{10}$.

Another new structural feature seen on intercalation is the increase in length of the titanium oxygen bond ($\text{Ti}2 - \text{O}3$) facing the interlayer space. This bond has a length of 1.75 \AA in $\text{K}_2\text{La}_2\text{Ti}_3\text{O}_{10}$.^[9] Structural refinement of $(\text{Li}_{1.8}\text{VO})\text{La}_2\text{Ti}_3\text{O}_{10}$ shows that this bond lengthens to 2.01 \AA . This change is also in agreement with what might be expected from purely size considerations because the ionic radii of Ti^{3+} (0.67 \AA) is greater than Ti^{4+} (0.61 \AA) for an

octahedral coordination.^[20] This could indicate that this titanium (Ti2) is the one that is reduced to Ti^{3+} , as Ti2 – O3 bond lengthens. Also, as lithium enters the structure and gives up its electron to the perovskite block, it is reasonable to assume that it coordinates with the oxygens available at the interlayer, which are O3 and the vanadyl oxygen. Therefore, both of these bonds, Ti2 – O3 and V=O are going to elongate in order to accommodate lithium.

Lithium intercalation reduces Ti^{4+} (d^0) to Ti^{3+} (d^1) forming a mixed-valence compound. The formal oxidation states on the titanium in the three samples are +3.73 for $(Li_{0.83}VO)La_2Ti_3O_{10}$, +3.53 for $(Li_{1.4}VO)La_2Ti_3O_{10}$ and +3.40 for $(Li_{1.8}VO)La_2Ti_3O_{10}$. The first two samples, with 27.6% to 46.6% Ti^{3+} per formula unit, do not show any magnetic ordering, behaving as Curie-Weiss paramagnets. A slight preference for an antiferromagnetic exchange is noted in the Curie-Weiss fit, as represented by a negative Weiss constant (Table 3.4). This antiferromagnetic tendency could potentially be due to the V-O-V chains. In $(VO)La_2Ti_3O_{10}$, the vanadyl units are isolated and the electron is localized on the vanadium atom. For the lithium-intercalated samples, we have seen in the IR the stretch at 865 cm^{-1} signaling the presence of V-O-V chains.^[18,19] For the highest lithium content sample $(Li_{1.8}VO)La_2Ti_3O_{10}$, magnetic order and a predisposition toward ferromagnetism is observed. The difference between the first two samples and the third resides mainly in the fraction of Ti^{3+} (d^1). $(Li_{1.8}VO)La_2Ti_3O_{10}$ has 60% Ti^{3+} , therefore a $Ti^{3+} - O - Ti^{4+}$ type of bond is possible in the corner sharing TiO_6 octahedra in the perovskite blocks. These bridges could permit the transfer of an electron from a Ti^{3+} ion to the central O^{2-} ion simultaneously with the transfer of an electron from the O^{2-} to the Ti^{4+} ion through a double exchange mechanism. This can be seen from the following scheme.



Zener showed that the lowest energy for such a system corresponds to a parallel alignment of the spins on the metal ions.^[21] The parallel alignment of the spins in this situation leads to an increase in the mobility of electrons between adjacent titaniums. Similar effects have also been observed in other oxide layered systems.^[22,23] The band structures and DOS presented in Figure 3.5 and Figure 3.6 support this assumption, showing that the system should be metallic. As it can be seen from the band structure picture, the bands are almost dispersionless, especially along the X – P – N, which is consistent with electronic isolation of the oxide layers along the c-axis. The states at and slightly above the Fermi level are antibonding combinations, π^* , resulting from the mixing of titanium t_{2g} with O 2p states. In this simple, rigid band model, the antibonding orbitals combinations, π^* , are the states that are occupied by the electrons introduced in the structure when Ti^{4+} is reduced to Ti^{3+} upon lithium intercalation.

In summary, a new series of mixed valence triple layered Ruddlesden-Popper titanates, $(\text{Li}_x\text{VO})\text{La}_2\text{Ti}_3\text{O}_{10}$, have been prepared by a two-step topotactic method. Combining such topotactic routes and applying them to appropriate layered materials hold the promise for future preparation of new compounds with tunable properties.

3.5 References

- [1] Choy, J. H.; Kim, J. Y.; Chung, I. *J. Phys. Chem. B* **2001**, *105*, 7908.
- [2] Armstrong, A. R.; Anderson, P. A. *Inorg. Chem.* **1994**, *33*, 4366.
- [3] Toda, K.; Teranishi, T.; Takahashi, M.; Ye, Z. G.; Sato, M. *Solid State Ionics* **1998**, *115*, 501.
Toda, K.; Teranishi, T.; Takahashi, M.; Ye, Z. G.; Sato, M.; Hinatsu, Y. *J. Mater. Chem.* **1999**, *9*, 799.
- [4] Toda, K.; Sato, M. *J. Eur. Ceram. Soc.* **1999**, *19*, 1525.
- [5] Hyett, G.; Rutt, O. J.; Gál, Z. A.; Denis, S. G.; Hayward, M. A.; Clarke, S. J. *J. Am. Chem. Soc.*, **2004**, *126*, 1980.
- [6] McIntyre, R.A.; Falter, A.U.; Li, S. Simmons Jr., W.B.; O'Connor, C.J.; Wiley, J. B. *J. Am. Chem. Soc.* **1998**, *120*, 217.
- [7] Lalena, J.N.; Cushing, B.L.; Falster, A.U.; Simmons, W.B. Jr.; Seip, C.T.; Carpenter, E.E.; O'Connor, C.J. and Wiley, J. B. *Inorg. Chem.* **1998**, *37*, 4484.
- [8] Toda, K.; Watanabe, J.; Sato, M. *Mat. Res. Bull.* **1996**, *31*, 1427.
- [9] Gopalakrishnan, J.; Sivakumar, T.; Ramesha, K.; Thangadurai, V.; Subanna, G. N. *J. Am. Chem. Soc.* **2000**, *122*, 6237.
- [10] Neiner, D. Sweany, R. L. Golub, V. and Wiley, J. B. in the Proceedings of the MRS Fall Meeting, Boston, MA, **2004**, 848 FF9.3.
- [11] Ibers, D. A. and J. A. Modified POLSQ, Department of Chemistry, Northwestern University, Evanston, IL, **1983**.
- [12] Larson, A.; Von Dreele, R. B. GSAS: Generalized Structure Analysis System, Los Alamos National Laboratory: Los Alamos NM, **1994**.

- [13] Le Bail, A. Duroy and Fourquet, *Mater. Res. Bull.* **1988**, 23, 447.
- [14] Hyeon, Ki-An and Byeon, Song-Ho *Chem. Mater.* **1999**, 11, 352.
- [15] Atkins, P. W. and Friedman, R. S. “*Molecular Quantum Mechanics*”, 3rd ed. Oxford University Press, **1997**, p. 98.
- [16] Landrum, G. and Hoffman, R. *Yet Another Extended Hückel Molecular Orbital Package (YAEHMOP)*, <http://yaehmop.sourceforge.net/>
- [17] Hughes, D. L.; Kleinkes, U.; Leigh, G. J.; Maiwald, M.; Sanders, J. R.; Sudbrake, C. *J. Chem. Soc., Dalton Transactions: Inorganic Chemistry* **1994**, 16, 2457-66, 1972.
- [18] Serrette, A.; Carroll P. J. and Swager, T. M. *J. Am. Chem. Soc.* **1992**, 114, 1887.
- [19] Shannon, R. D. and Prewitt, C. T. *Acta Cryst.* **1969**, B 25, 925.
- [20] Zener, C. *Phys. Rev.*, **1951**, 82, 403.
- [21] Park, M. S. and Min, B. I. *cond-mat/0212611*, <http://arXiv.org/abs/cond-mat/0212611>.
- [22] Hiroi, Z.; Azuma, M.; Fujihira, Y.; Saito, T.; Takano, M.; Izumi, F.; Kamiyama, T.; Ikeda, T. *J. Solid State Chem.* **1999**, 146, 369.

Chapter 4

Structural and Magnetic Investigation of $\text{Li}_{0.3}\text{Ni}_{0.85}\text{La}_2\text{Ti}_3\text{O}_{10}$

4.1 Introduction

The reactivity of the A' cations makes the Ruddlesden Popper compounds, $\text{A}_2'[\text{A}_{n-1}\text{B}_n\text{O}_{3n+1}]$, effective precursors to new low temperature phases via topochemical routes. One of the most effective topotactic routes is the replacement of the A' cations via an ion exchange reaction. These reactions can take place in either aqueous medium, molten salts or solid state. In addition, monovalent and divalent ions can be exchanged. Monovalent ion exchange has led to $\text{Li}_2\text{La}_2\text{Ti}_3\text{O}_{10}$ and acidic form, $\text{H}_2\text{La}_2\text{Ti}_3\text{O}_{10}$, from molten state and acidic aqueous solution, respectively.^[1,2] Divalent ion exchange $\text{MLa}_2\text{Ti}_3\text{O}_{10}$ with M= Co, Zn, Cu has been performed using an eutectic mixture of alkali metal chlorides and transition metal chlorides in sealed tubes.^[3]

This work constitutes an extension of such ion exchange reactions in the triple layered Ruddlesden-Popper series to obtain $\text{Li}_{0.3}\text{Ni}_{0.85}\text{La}_2\text{Ti}_3\text{O}_{10}$ by an aqueous solution reaction. This paper describes the synthesis, crystal structure, thermal behavior, magnetic, and electronic properties of this new compound.

4.2 Experimental

4.2.1 Synthesis

$\text{Na}_2\text{La}_2\text{Ti}_3\text{O}_{10}$ was prepared by a solid state reaction from Na_2CO_3 (Alfa Aesar 99.99%), La_2O_3 (Alfa Aesar 99.99%) and TiO_2 (Alfa Aesar 99.99%). A 30% molar excess of Na_2CO_3 was

used to compensate for the loss due to volatilization. The reagents were pressed into pellets, fired at 550 °C for 6 hours, and then sintered at 1050 °C for 12 hours.^[1] After the reaction, to remove unreacted Na₂CO₃, the sample was washed with warm water and acetone and dried at 150°C overnight. Phase purity for Na₂La₂Ti₃O₁₀ was confirmed by X-ray powder diffraction (XRD); the sample was indexed on the tetragonal unit cell $a = 3.8352(7) \text{ \AA}$ and $c = 28.5737(7)$, which is in agreement with the values reported in the literature. Sodium was replaced with lithium by an ion exchange reaction between the Na₂La₂Ti₃O₁₀ and LiNO₃, in a 1:15 molar ratio for two days at 300 °C. Li_{0.3}Ni_{0.85}La₂Ti₃O₁₀ was prepared by an aqueous solution (150 ml water) reaction between Li₂La₂Ti₃O₁₀ and NiCl₂ in 1:2 molar ratio, at 50 – 65 °C, under continuous stirring for 8 days. The reaction mixture was refreshed with a new nickel chloride solution after the first four days. The reaction can also take place if instead of NiCl₂, Ni(NO₃)₂ is used.^[6] The final product was washed with distilled water and acetone and dried at 100 °C overnight. Li_{0.3}Ni_{0.85}La₂Ti₃O₁₀ has a pale green color. The nickel ion exchange reaction was performed between the NiCl₂ with Na₂La₂Ti₃O₁₀ and K₂La₂Ti₃O₁₀, but it did not lead to the formation of NiLa₂Ti₃O₁₀.

4.2.2 Characterization

Elemental analysis was carried out by energy dispersive spectroscopy (EDS) on a series of individual crystallites using a JEOL (model JSM-5410) scanning electron microscope (SEM) equipped with an EDAX (DX-PRIME) microanalytical system to determine nickel content. Inductively coupled plasma emission spectroscopy (ICP) analysis was performed to determine lithium content. The samples were dissolved in concentrated nitric acid. Standard solutions were prepared from Specpure Alfa Aesar 10,000 µg/ml for lithium. All the standards and the samples

were analyzed in a 5% HNO₃ solution (vol./vol.). The composition of the final product corresponded to the general formula Li_{0.30(1)}Ni_{0.85(2)}La₂Ti_{3.00(2)}O₁₀.

X-ray powder diffraction studies were carried out on a Philips X'Pert System (Cu K α radiation $\lambda = 1.5418 \text{ \AA}$) equipped with a graphite monochromator. Data were collected in a continuous scan mode between 5 and 95° 2 θ with a step size of 0.02. The lattice parameters were refined using POLSQ.^[4] Structural refinement was done by the Rietveld method with the GSAS package of programs.^[5] The refined parameters include background, peak shape, cell, atom positions, scale factor, and thermal parameters. The R-factor (R_p), the weighted R-factor (wR_p), and the goodness of fit, χ^2 , are defined as: $R_p = \sum[y_{io} - y_{ic}] / \sum y_{io}$, $wR_p = [\sum w_i(y_{io} - y_{ic})^2 / \sum w_i(y_{io})^2]^{1/2}$, $R_F = \sum[|I_k(\text{obs})|^{1/2} - |I_k(\text{calc})|^{1/2}] / [I_k(\text{obs})]^{1/2}$, and $\chi^2 = [wR_p / R_{\text{exp}}]^2$, where $R_{\text{exp}} = [(N - P) / \sum w_i y_{io}^2]^{1/2}$ and y_{io} and y_{ic} are the observed and the calculated intensities, w_i is the weighting factor, N is the total number of observed intensities when the background is refined, and P is the number of adjusted parameters.

Thermal behavior was studied on a TGA 51 thermogravimetric analyzer and a Netzsch 404 S differential scanning calorimeter (DSC); measurements were performed in oxidizing and inert atmospheres between room temperature and 800 °C by heating samples at 10 °C/min in O₂ and Ar, respectively.

Magnetic measurements were performed on a Quantum Design MPMS-5S Superconducting Quantum Interference Device (SQUID) magnetometer between 2 and 300 K at 100 Oe. Heat capacity, *ac* susceptibility and transport measurements (two probe method) were investigated using a PPMS Quantum Design between 5 K and 300 K.

4.3 Results

4.3.1 Synthesis

The ability of Ruddlesden-Popper, $A_2La_2Ti_3O_{10}$ ($A = Li, Na, K$), to undergo ion exchange with nickel chloride has been investigated. Single phase $Li_{0.3}Ni_{0.85}La_2Ti_3O_{10}$ was obtained only from $Li_2La_2Ti_3O_{10}$. The reaction did not occur using either the sodium or the potassium equivalents. The ion exchange was not complete. The chemical analysis of the product indicated the ratio $Li:Ni:La:Ti$ is 0.30(2):0.85(2):2:3.00(2). Increasing the molar ratio, the temperature or the time does not produce any increase for exchange. The reaction can also lead to $Li_{0.3}Ni_{0.85}La_2Ti_3O_{10}$ if the source of nickel is nickel nitrate hydrate.^[6]

4.3.2 Structure

The ion exchange takes place in a topotactic manner. In Figure 4.1 the XRD powder patterns for the $Li_2La_2Ti_3O_{10}$, and $Li_{0.3}Ni_{0.85}La_2Ti_3O_{10}$ are presented. The ion exchanged material was indexed on a tetragonal Bravais lattice with the cell parameters listed in Table 4.1.^[4] For $Li_{0.3}Ni_{0.85}La_2Ti_3O_{10}$, a Rietveld refinement was carried out.^[5] The observed, calculated and difference maps are presented in Figure 4.2. The atomic positions are presented in Table 4.2, and the bond lengths are shown in Table 4.3.

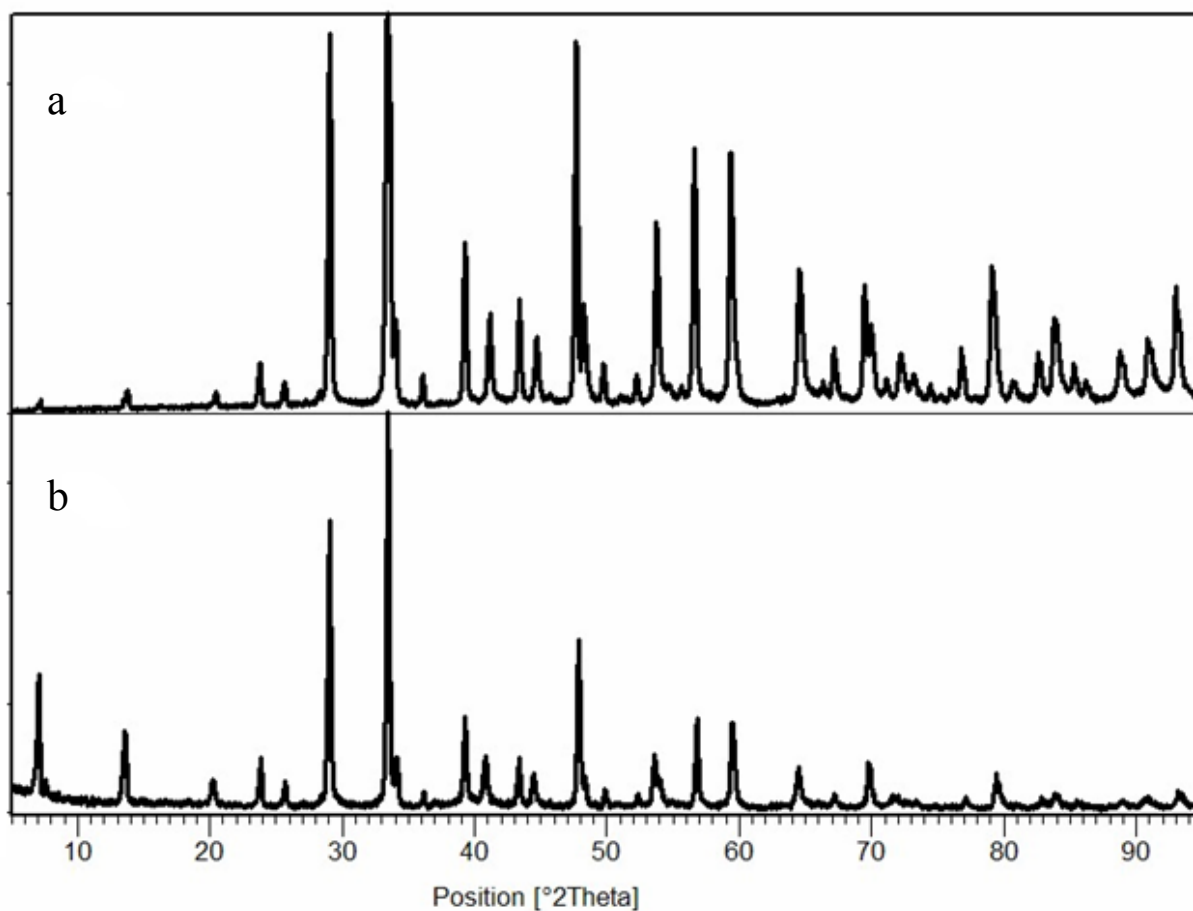


Figure 4.1 Comparison of the X-ray powder patterns for a) $\text{Li}_2\text{La}_2\text{Ti}_3\text{O}_{10}$; b) $\text{Li}_{0.3}\text{Ni}_{0.85}\text{La}_2\text{Ti}_3\text{O}_{10}$.

Table 4.1 The variation of the unit cell parameters and volume for the investigated materials

Compound	a (Å)	c (Å)	Volume (Å ³)
$\text{Li}_2\text{La}_2\text{Ti}_3\text{O}_{10}$	3.8411(6)	26.5601(2)	391.8(6)
$\text{Li}_{0.3}\text{Ni}_{0.85}\text{La}_2\text{Ti}_3\text{O}_{10}$	3.8483(1)	26.9871(2)	399.6(6)

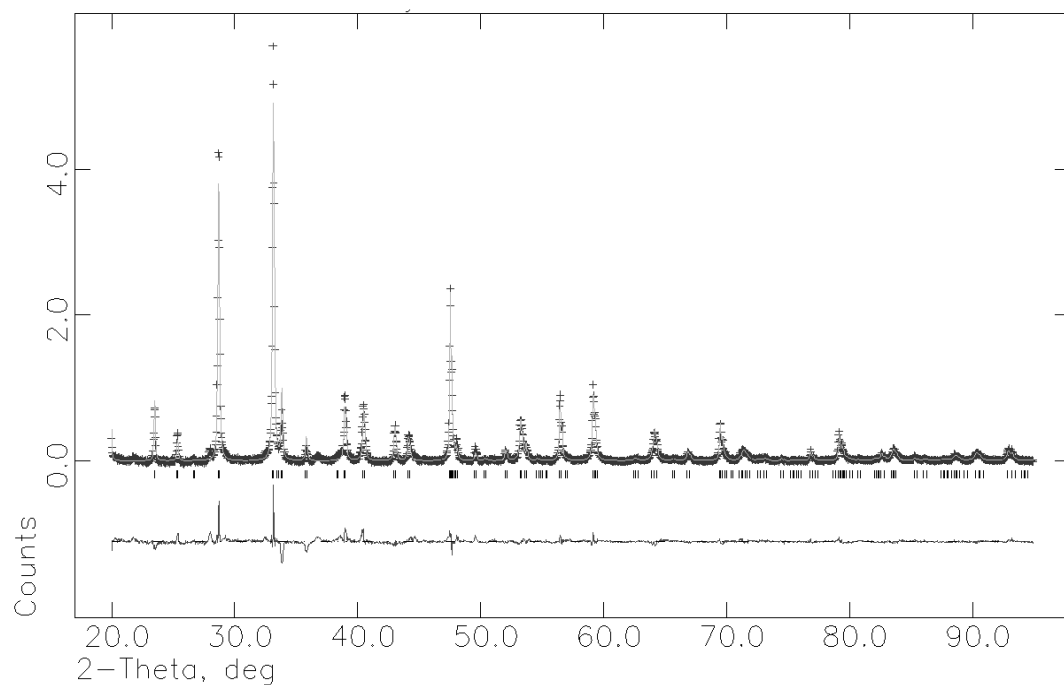


Figure 4.2 Calculated (solid line), experimental (crosses) and the difference (lower line) for $\text{Li}_{0.3}\text{Ni}_{0.85}\text{La}_2\text{Ti}_3\text{O}_{10}$.

Table 4.2 Crystallographic data for $\text{Li}_{0.3}\text{Ni}_{0.85}\text{La}_2\text{Ti}_3\text{O}_{10}$.

	Atom	Site	x	y	z	g^a	$U_{\text{iso}} (\text{\AA}^2)$
I4/ mmm	Ni	4d	0	0.5	0.25	0.425	0.01172(8)
$Z = 2$	La	4e	0	0	0.4193(3)	1.0	0.01875(2)
$a = 3.82444(2) \text{\AA}$	Ti1	2a	0	0	0	1.0	0.00426(4)
$c = 26.736(6) \text{\AA}$	Ti2	4e	0	0	0.1560(8)	1.0	0.03506(2)
$V = 391.0(6) \text{\AA}^3$	O1	4e	0	0	0.07440(7)	1.0	0.05275(1)
$R_p = 10.83 \%$	O2	4c	0	0.5	0	1.0	0.08511(3)
$wR_p = 14.52 \%$	O3	4e	0	0	0.23340(9)	1.0	0.02353(2)
$\chi^2 = 3.11\%$	O4	8g	0	0.5	0.1446(3)	1.0	0.0066(2)

^a g = occupancy

Table 4.3 Bond lengths and bond angles for $\text{Li}_{0.3}\text{Ni}_{0.85}\text{La}_2\text{Ti}_3\text{O}_{10}$.

Bond	Length Å/ angle °
Ni - O3 (X 4)	1.96300(3)
Ti1 - O1 (X 2)	1.98940(7)
Ti1 - O2 (X 4)	1.91222(3)
Ti2 - O1 (X 1)	2.18367(2)
Ti2 - O3 (X 1)	2.06747(8)
Ti2 - O4 (X 4)	1.93654(3)
La - O1 (X 4)	2.70946(4)
La - O2 (X 4)	2.88238(6)
O3 - Ni - O3	153.880(1)
O3 - Ni - O3	92.927(0)

4.3.3 Thermal Behavior

Differential scanning calorimetry for $\text{Li}_{0.3}\text{Ni}_{0.85}\text{La}_2\text{Ti}_3\text{O}_{10}$ in both oxidizing and inert atmosphere shows that this compound is a metastable phase that undergoes a phase transition above 300 °C. The DSC curves, presented in Figure 4.3 show a broad exothermic peak around 300 °C. The XRD after DSC at 200 °C, 400 °C and 800 °C are shown in Figure 4.4.

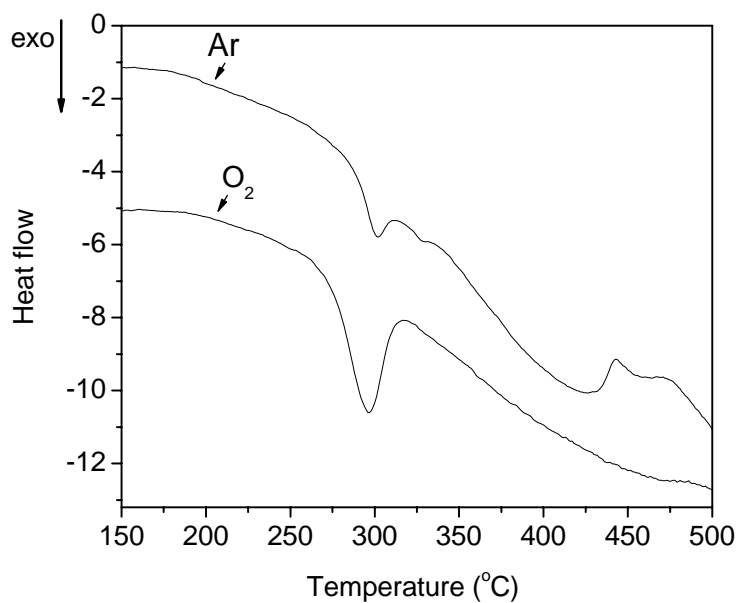


Figure 4.3 DSC curves in argon and oxygen for $\text{Li}_{0.3}\text{Ni}_{0.85}\text{La}_2\text{Ti}_3\text{O}_{10}$.

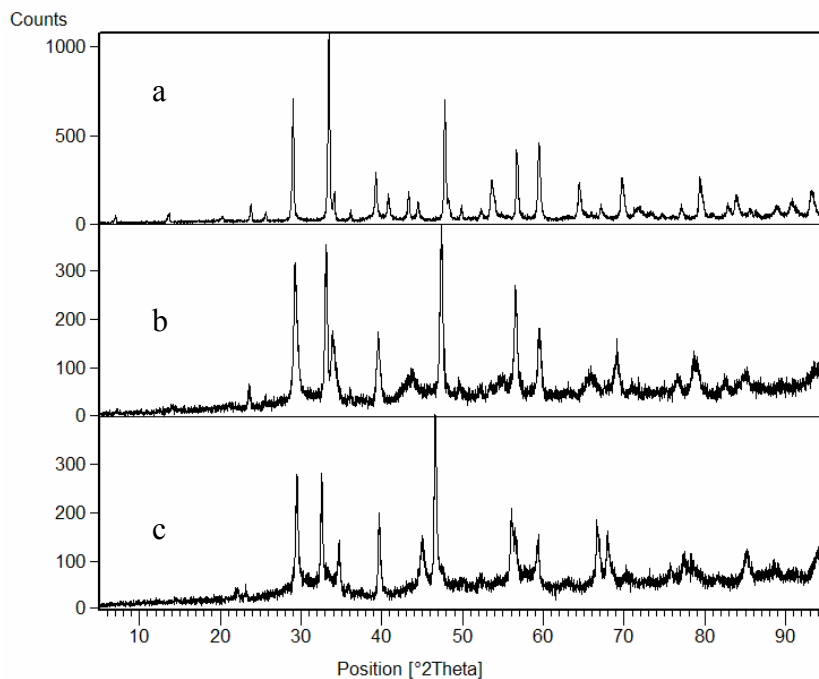


Figure 4.4 Comparison of the XRD for $\text{Li}_{0.3}\text{Ni}_{0.85}\text{La}_2\text{Ti}_3\text{O}_{10}$ after DSC in Ar at a) 200 °C, b) 400 °C, and c) 800 °C.

The thermal decomposition of this material above 300 °C is accompanied by a continual weight loss in inert atmosphere, as seen from the TGA in Ar measurements. The weight loss up to the first plateau at 300 °C is 2.47%. $\text{Li}_{0.3}\text{Ni}_{0.85}\text{La}_2\text{Ti}_3\text{O}_{10}$ starts losing this weight at approximately 200 °C, so presumably the layered structure is maintained. The total weight loss up to 800 °C adds to 7.64 %. The XRD after DSC and TGA shows that at 400 °C, NiO starts forming and at 800 °C, constitutes the predominant phase. Mixed in with NiO, is a defective perovskite phase, most likely $\text{La}_2\text{Ti}_3\text{O}_9$.

4.3.4 Band Structure Calculations and Transport Measurements

The band structure calculations and transport measurements on $\text{Li}_{0.3}\text{Ni}_{0.85}\text{La}_2\text{Ti}_3\text{O}_{10}$ are consistent with an insulator.^[7] Transport measurements suggest that $\text{Li}_{0.3}\text{Ni}_{0.85}\text{La}_2\text{Ti}_3\text{O}_{10}$ has a resistivity greater than 1 GΩ. The band structures along with the density of states (DOS) are presented in Figure 4.5. From the band dispersion at the Fermi level, it can be inferred that the electrons are localized on the nickel atom. The bands at and slightly below the Fermi level are Ni 3d states.

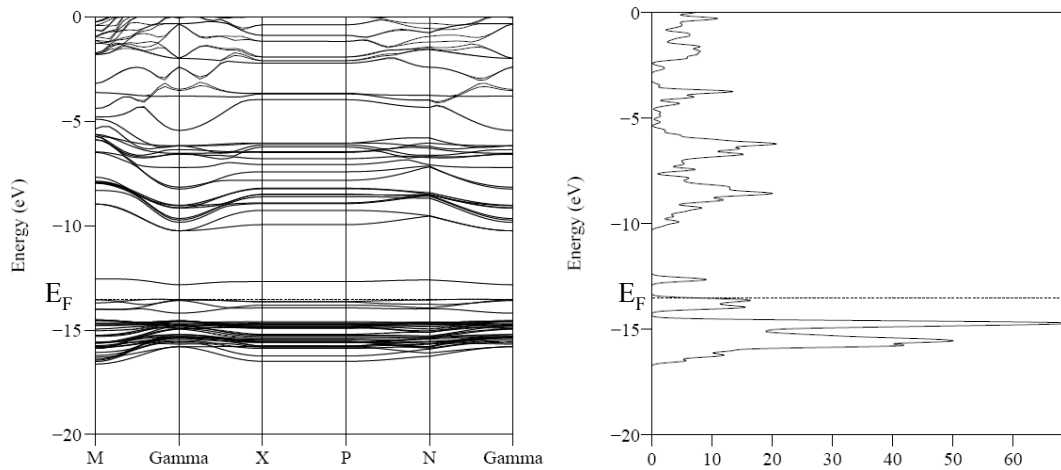


Figure 4.5 The band structures and the DOS for $\text{Li}_{0.3}\text{Ni}_{0.85}\text{La}_2\text{Ti}_3\text{O}_{10}$.

4.3.5 Magnetic Behavior and Heat Capacity

The magnetic susceptibility as a function of temperature in a 100 Oe and 10,000 Oe fields, and the linear fit of the reciprocal susceptibility versus temperature along with the hysteresis loops at 5 K, 20 K and 40 K, are shown in Figure 4.6. From the linear fit a magnetic moment was calculated for $\text{Li}_{0.3}\text{Ni}_{0.85}\text{La}_2\text{Ti}_3\text{O}_{10}$, $\mu = 2.97 \mu_B$ and a Weiss constant of 5 K. The calculated magnetic moment is in agreement with other values reported in the literature for a d^8 system in a tetrahedral ligand field. From the variation of the magnetic moment as a function of temperature and from the positive Weiss constant, the transition at 23 K seems to be ferromagnetic. Heat capacity measurements on this compound were performed between room temperature and 5 K on several samples. The heat capacity versus temperature is shown in Figure 4.7. Here only the 5-100 K is presented. As it can be seen from Figure 4.7, there is an inflection point at 23 K. This is an indication that a disorder–order transition takes place. Further, this transition can be correlated with the ferromagnetic transition seen in the magnetic data. To extract the magnetic component to the heat capacity, the correspondent states law has been used.^[8]

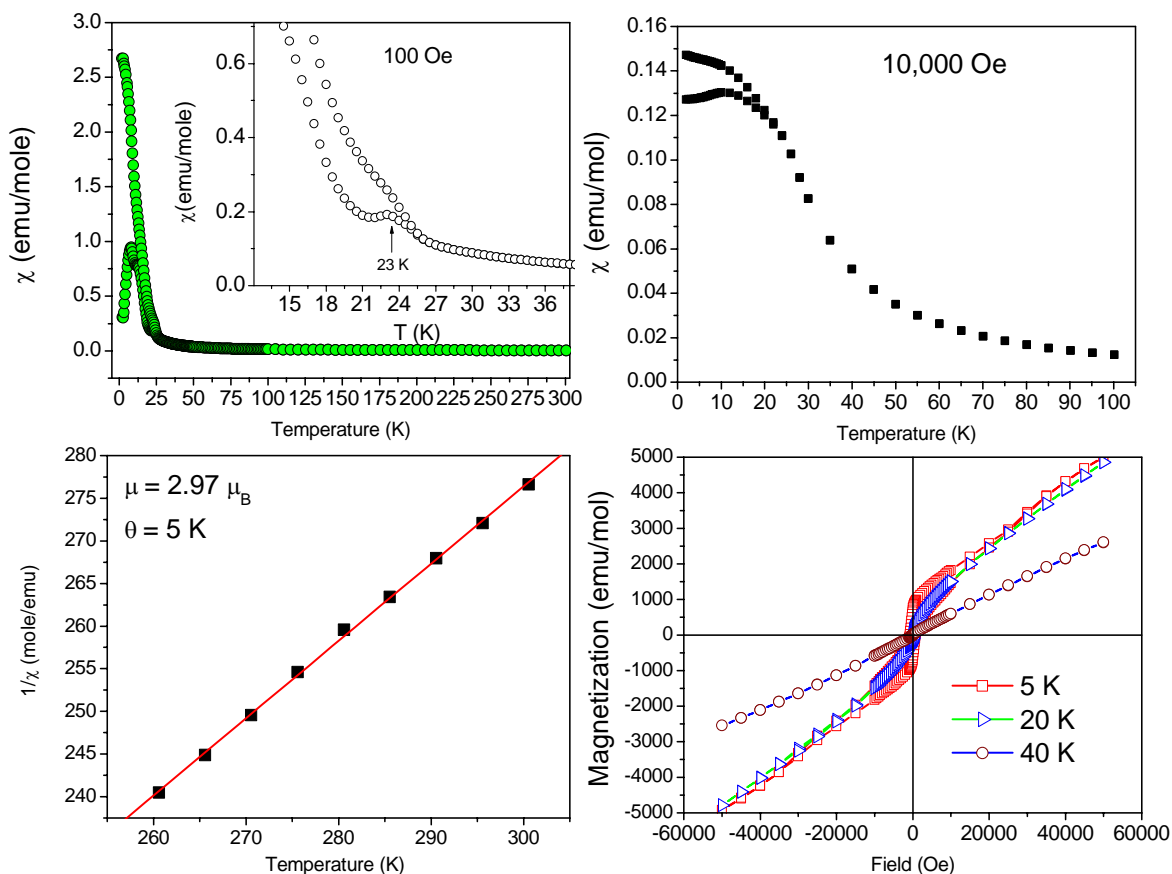


Figure 4.6 The magnetic behavior of $\text{Li}_{0.3}\text{Ni}_{0.85}\text{La}_2\text{Ti}_3\text{O}_{10}$. a) The magnetic susceptibility versus temperature in 100 Oe (the inset emphasizes the transition at 23 K); b) The magnetic susceptibility versus temperature in a 10,000 Oe; c) The reciprocal susceptibility versus temperature along with the linear fit; d) The hysteresis loops at 5 K, 20 K and 40 K .

The non-magnetic equivalent used in this case was the parent, $\text{Li}_2\text{La}_2\text{Ti}_3\text{O}_{10}$. The heat capacity of the parent was measured in the same conditions as for the $\text{Li}_{0.3}\text{Ni}_{0.85}\text{La}_2\text{Ti}_3\text{O}_{10}$. The specific heats for the two compounds are presented in Figure 4.7. The heat capacity for Li-compound was used as the lattice heat capacity for $\text{Li}_{0.3}\text{Ni}_{0.85}\text{La}_2\text{Ti}_3\text{O}_{10}$. The lattice component to the specific heat was then subtracted out and the resulting specific heat is shown in Figure 4.8. The magnetic entropy gained at the transition was calculated by integrating the area under the

C_p / T versus T curve, Figure 4.8. The magnetic entropy is consistent with an $S=1$ magnetic system.^[8]

$$S = \int C_p / T = R \ln(2S + 1)$$

Moreover, in a magnetic field of 1 T, the transition shifts to higher temperatures and broadens. The shift to higher temperatures confirms the ferromagnetic nature of this transition. This is represented in Figure 4.9.

In Figures 4.10 and 4.11 the ac susceptibility measurements are presented. It can be inferred from these figures, that both of the transitions are present in both the real and the imaginary components of the susceptibility. In addition, the transitions seem to be frequency dependent. In a dc magnetic field, the transition at 10 K shifts towards the high temperature transition at 23 K.

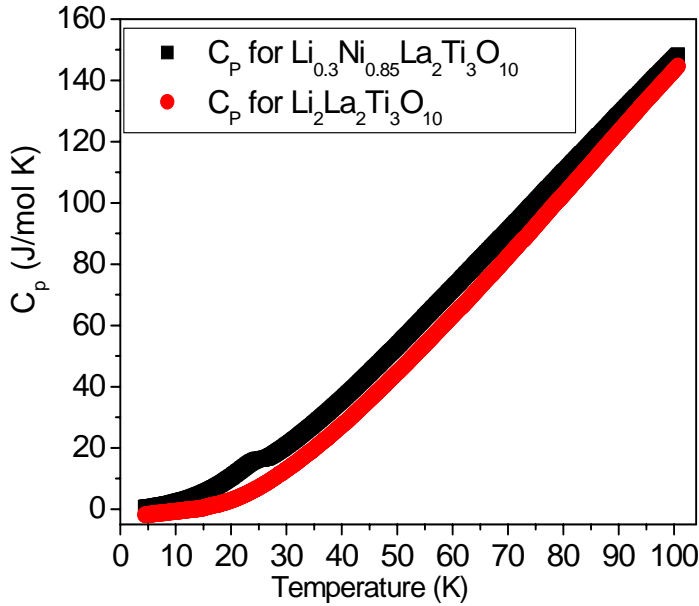


Figure 4.7 Heat capacity for $\text{Li}_2\text{La}_2\text{Ti}_3\text{O}_{10}$ and $\text{Li}_{0.3}\text{Ni}_{0.85}\text{La}_2\text{Ti}_3\text{O}_{10}$

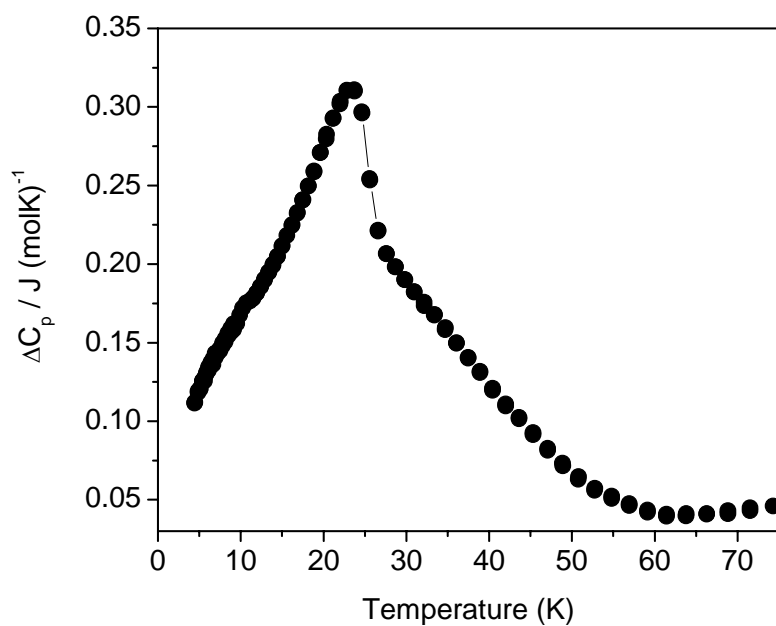


Figure 4.8 The magnetic contribution at the specific heat for $Li_{0.3}Ni_{0.85}La_2Ti_3O_{10}$.

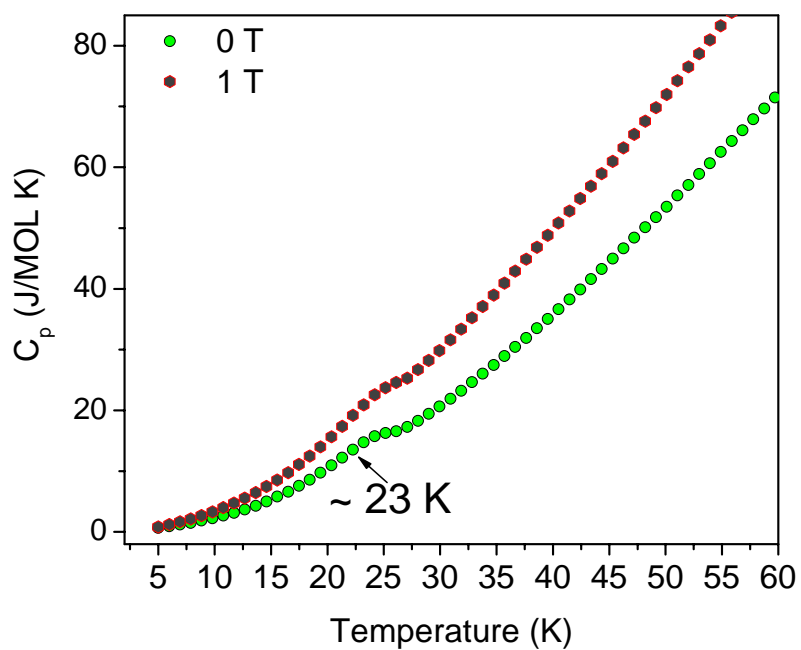


Figure 4.9. In field heat capacity data for $Li_{0.3}Ni_{0.85}La_2Ti_3O_{10}$.

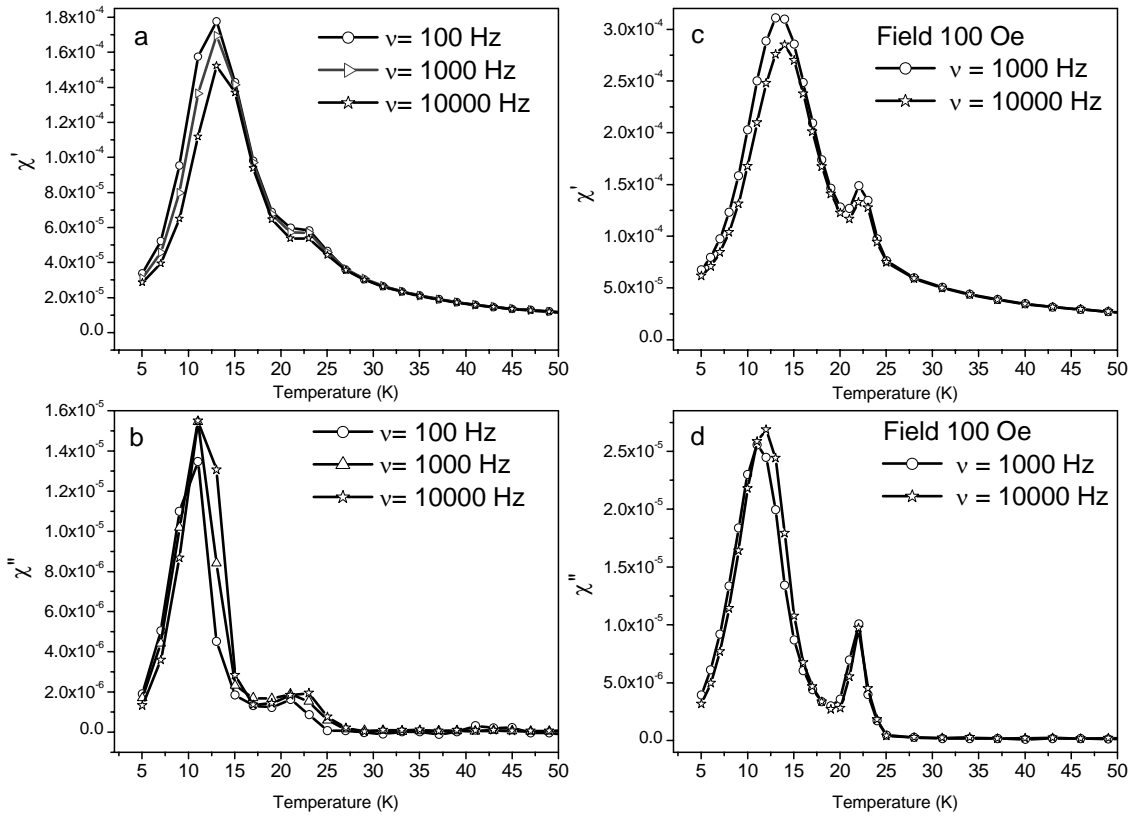


Figure 4.10 The ac susceptibility at 100, 1000 and 10,000 Hz for a,b-no field real and imaginary components in the absence of a dc applied magnetic field; c,d 100 Oe field for $\text{Li}_{0.3}\text{Ni}_{0.85}\text{La}_2\text{Ti}_3\text{O}_{10}$.

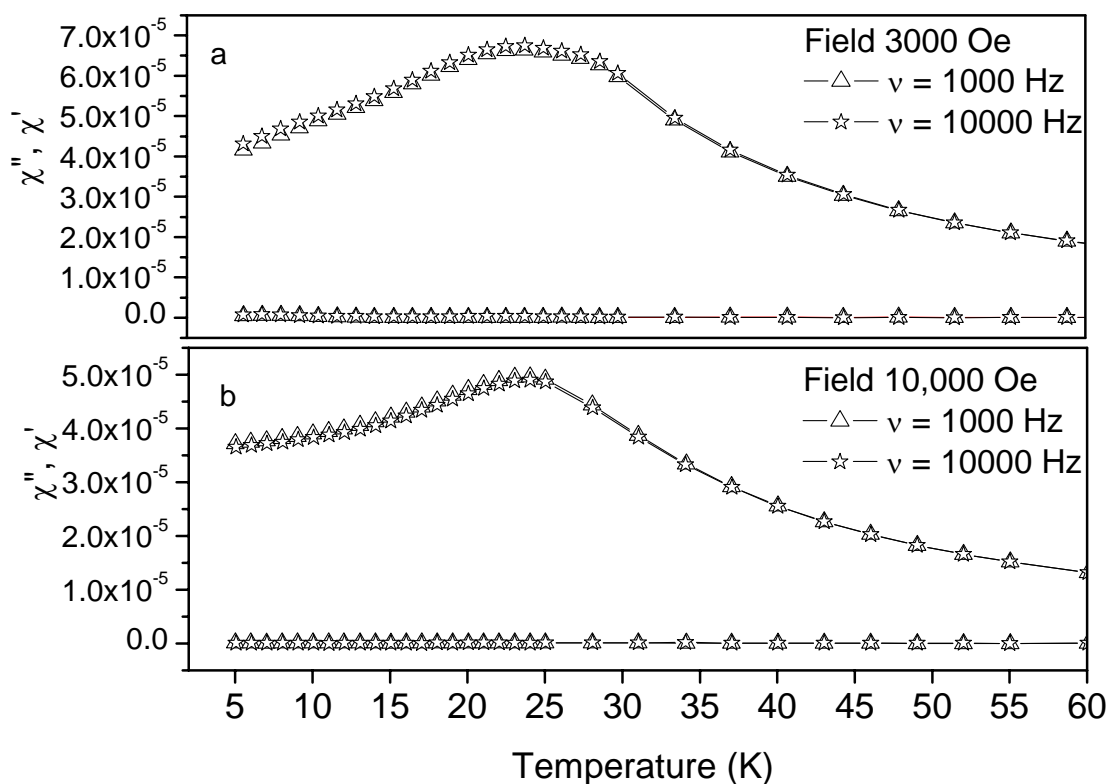


Figure 4.11 In field ac susceptibility for $\text{Li}_{0.3}\text{Ni}_{0.85}\text{La}_2\text{Ti}_3\text{O}_{10}$ in a) 3000 Oe and b) 10,000 Oe. The frequency used are 1000 and 10,000 Hz.

4.4 Discussion

The composition of the ion exchanged product corresponds to the formula $\text{Li}_{0.30(1)}\text{Ni}_{0.85(1)}\text{La}_{2.00}\text{Ti}_{3.00(2)}\text{O}_{10}$. A complete exchange leading to $\text{Ni}:\text{La}:\text{Ti} = 1:2:3$ was not observed even when varying the reaction conditions. This has been observed in other layered systems and has been attributed to the trapping of some alkali metal cations between the perovskite blocks.^[9] ICP shows the presence of small amounts of lithium in the sample.

The XRD for $\text{Li}_{0.30(1)}\text{Ni}_{0.85(2)}\text{La}_2\text{Ti}_3\text{O}_{10}$ is comparable with $\text{Li}_2\text{La}_2\text{Ti}_3\text{O}_{10}$. The layered structure has been maintained upon ion exchange. The structural refinement was based on the

$\text{Li}_2\text{La}_2\text{Ti}_3\text{O}_{10}$ cell, where Ni has replaced lithium, and the composition adjusted for 42.5% occupancy of the site. Interestingly, the unit cell expands along the c-axis upon ion exchange. Therefore, the trapping of lithium ions between the perovskite sheets does not occur because of their inability to exit the interlayer space. It is the tetrahedral arrangement of the Ni between the perovskite layers in combination with a relaxation of the Ti2-O3 bond that leads to this expansion.

The thermal behavior of this compound shows that an exothermic transition occurs in both inert and oxidizing atmosphere. In addition, a continuous weight loss is seen in TGA. The XRD after DSC shows that the layered structure is maintained at 400 °C, but the crystallinity degrades. At 800 °C, though the perovskite blocks are almost intact but the layered structure is destroyed. The decomposition products are NiO and $\text{La}_2\text{Ti}_3\text{O}_9$. This is consistent with the metastability observed in other ion exchanged layered perovskites. In addition, it demonstrates that $\text{Li}_{0.3}\text{Ni}_{0.85}\text{La}_2\text{Ti}_3\text{O}_{10}$ could not be obtained by high temperature methods since it is not stable under these conditions.

$\text{Li}_{0.3}\text{Ni}_{0.85}\text{La}_2\text{Ti}_3\text{O}_{10}$ has a unique magnetic behavior. First, in a small field, 100 Oe, the ZFC/FC curves split below 30 K. This is consistent with the magnetic ordering of nickel ions below this temperature. This behavior has been seen in both long range magnetically ordered systems and spin glasses.^[10,11] Then, two magnetic transitions occur, one at 23 K and one at 10 K. The magnetic moment calculated from the linear fit of the reciprocal susceptibility versus temperature is consistent with an $S = 1$ magnetic system. The fit also gives a positive Weiss constant, which suggest ferromagnetic interactions. In higher fields, 10,000 Oe, the magnetic behavior of $\text{Li}_{0.3}\text{Ni}_{0.85}\text{La}_2\text{Ti}_3\text{O}_{10}$ changes. The ZFC/FC curves split in the same temperature range as in low field (100 Oe), but there is not a clear transition at 10 K, and the transition at 23 K

broadens. Heat capacity data is consistent with an order-disorder transition at 23 K. In field, heat capacity data confirms the ferromagnetic origin of this transition, since with the applied field the transition shifts to higher temperatures. In addition, the magnetic entropy gained at the transition is consistent with a $S = 1$ system.^[10] Further, from Figure 4.8 in the inset, it can be seen that there is a tail for the C versus T curve for the magnetic specific heat. This tail can be attributed to Schottky anomaly due to nickel ion anisotropy.^[8]

For the 10 K transition, ac susceptibility measurements have been used to investigate the possibility of a spin glass like behavior. AC susceptibility data is very useful for spin glasses since their freezing point cannot be obtained from the heat capacity.^[10] Also, ac data can help distinguish between ferromagnetic and antiferromagnetic types of ordering because antiferromagnets lack a signal in the imaginary part of the ac susceptibility. Since both of the transitions are present in the real as well as the imaginary part of the ac susceptibility, an antiferromagnetic order can be ruled out. Both of these transitions are frequency dependent. It is generally very hard to distinguish between a ferromagnetic and a spin glass transition, because they are so much alike. Both spin glasses and ferromagnets are characterized by ZFC/FC splitting, hysteresis loops and frequency dependent ac susceptibilities. There are subtle differences though. A sharp peak appears at the freezing point in spin glasses and a sharp peak appears in ferromagnets at the Curie point. In contrast with ferromagnetic transitions, the spin glass transition can be rounded by high magnetic field. As shown in Figure 4.5, a 10,000 Oe dc field rounded the 10 K transition. In addition, the in-field ac susceptibility shows that the transition at 10 is first, rounded, in small fields (Figure 4.8), and completely shifts (Figure 4.9) in higher fields, 3000 Oe and 10,000 Oe. Because spin glasses are amorphous magnetic systems, they do not show an inflection point in the specific heat. It is very difficult to rule out a spin glass

transition based on our specific heat data since our measurements were performed between 2 K and 300 K. It is known that the magnetic transition temperatures from specific heat can be very different from the ones in the magnetic data. It has been seen that the specific heat transition temperature can be displaced lower in temperature by as much as 10 K. Therefore, based only on specific heat, we cannot rule out another order-disorder transition occurring below 2 K. The in-field ac susceptibility data is consistent with a spin glass like behavior. The frequency dependence in zero field disappears in a 3 kOe and 10 kOe field confirming the spin glass like behavior.^[12]

Going back to the ion exchange reaction, it is easy to rationalize such a behavior. When replacing lithium (+1) with nickel (+2) only one nickel goes in the interlayer space for every two lithium ions. This maintains the charge balance. The interlayer space is left with half of the sites empty. The basic requirements for a glass state are the existence of disorder and frustration. It is reasonable to assume that a structure having 42.5% occupancy for the magnetic ion site (Ni^{2+}), constitutes a disordered structure. Presumably, in such a disordered structure, frustration can occur whenever a nickel is missing. Considering a Ni – O – Ni, periodic arrangement, frustration should not occur because the magnetic ions are correlated via a superexchange interaction. If one nickel is missing in such an arrangement, then the nearest neighbor interactions will be frustrated. Thus, the spin glass transition comes from an unsatisfied ferromagnetic arrangement for the magnetic ions. Therefore, a magnetic phase diagram for $\text{Li}_{0.3}\text{Ni}_{0.85}\text{La}_2\text{Ti}_3\text{O}_{10}$ could be paramagnetic 30 K – 300 K, followed by a ferromagnetic region 30 K -10 K, and a spin glass below 10 K. Because, the spin glass comes from a ferromagnetic state instead of a paramagnetic one, can be classified as a reentrant spin glass.^[10,13]

4.5 References

- [1] Toda, K.; Watanabe, J.; Sato, M. *Materials Research Bulletin* **1996**, *31*, 1427.
- [2] Gopalakrishnan, J.; Uma, S.; Bhat, V.; *Chem. Mater.*, **1993**, *5*, 132.
- [3] Hyeon, Ki-An and Byeon, Song-Ho *Chem. Mater.* **1999**, *11*, 352.
- [4] D. A. and J. A. Ibers, *Modified POLSQ*, Department of Chemistry, Northwestern University, Evanston, IL, **1983**.
- [5] Larson, A.; Von Dreele, R. B. *GSAS: Generalized Structure Analysis System*, Los Alamos National Laboratory: Los Alamos NM, **1994**.
- [6] Schaak, R. E. and Mallouk, T. E. *J. Am. Chem. Soc.* **2000**, *122*, 2798.
- [7] Landrum, G. and Hoffmann, R. *Yet Another Extended Hückel Molecular Orbital Package* (YAEHMOP), <http://yaehmop.sourceforge.net/>.
- [8] R. L. Carlin, *Magnetochemistry*, Springer-Verlag Berlin Heidelberg, **1986**.
- [9] McIntyre, R. A.; Falster, A. U.; Sichu Li; Simmons, W. B.; O'Connor, C. J. and Wiley, J. B. *J. Am. Chem. Soc.* **1998**, *120*, 217.
- [10] Moorjani, K. and Coey, J. M. D. *Magnetic glasses*, Elsevier Science Publishers B. V., **1984**.
- [11] Rayaprol, S.; Sengupta, K.; and Sampathkumaran, E. V. *Phys. Rev. B* **2003**, *67*, 180404(R).
- [12] Rao, C.N.R.; Paul, G.; Choudhury, A.; Sampathkumaran, E.V.; Raychaudhuri, A. K. Ramasesha S. and Rudra, I. *Phys. Rev. B* **2003**, *67*, 134425.
- [13] Blasco, J.; Garcia, J.; Sanchez, M. C.; Larrea, A.; Campo J. and Subias, G. *J. Phys.: Condens. Mater.* **2001**, *13*, L729.

Chapter 5

Lithium intercalation in $\text{Li}_{0.3}\text{Ni}_{0.85}\text{La}_2\text{Ti}_3\text{O}_{10}$

5.1 Introduction

Ruddlesden-Popper layered perovskites can intercalate alkali metal ions into their interlayer galleries. The insertion of these cations takes place in a topotactic manner such that the layered structure is maintained. Reductive intercalation reactions are important for tuning the valency, and therefore the electronic and magnetic properties. In our group it has been shown that using a two-step low temperature route (ion exchange and then reductive intercalation), mixed valence compounds, with semiconducting behavior, such as $\text{Na}_{1-x+y}\text{Ca}_{x/2}\text{LaTiO}_4$, $\text{Na}_{2-x+y}\text{Ca}_{x/2}\text{La}_2\text{Ti}_3\text{O}_{10}$ and $(\text{Li}_x\text{VO})\text{La}_2\text{Ti}_3\text{O}_{10}$ can be obtained.^[1-3] Herein we describe the influence of lithium intercalation upon structure, electronic and magnetic properties of the triple layered Ruddlesden-Popper perovskite, $\text{Li}_{0.3}\text{Ni}_{0.85}\text{La}_2\text{Ti}_3\text{O}_{10}$. This compound was prepared from the triple layered Ruddlesden-Popper perovskite, $\text{Li}_2\text{La}_2\text{Ti}_3\text{O}_{10}$, by ion exchange with the divalent nickel ion.^[1] As in other divalent reactions, two lithium ions are replaced by a nickel and a vacancy.^[2-4] Lithium metal ions can then be intercalated into these vacancies. This paper presents a detailed description of the synthesis and characterization of this new series of compounds.

5.2 Experimental

5.2.1 Synthesis The parent, $\text{Li}_2\text{La}_2\text{Ti}_3\text{O}_{10}$, was prepared from $\text{Na}_2\text{La}_2\text{Ti}_3\text{O}_{10}$ and LiNO_3 (Alfa Aesar 99.997%) mixed in a 1:15 molar ratio and heat at 300 °C for 2 days. Phase purity for $\text{Li}_2\text{La}_2\text{Ti}_3\text{O}_{10}$ was confirmed by X-ray powder diffraction (XRD). The powder pattern was indexed in a tetragonal unit cell, $a = 3.8411(6) \text{ \AA}$ and $c = 26.5601(2) \text{ \AA}$, which is in agreement with literature values.^[5]

Ion exchange was used to substitute the Li^+ ions in $\text{Li}_2\text{La}_2\text{Ti}_3\text{O}_{10}$ with nickel ions. The source of nickel is nickel chloride (NiCl_2 , Alfa Aesar, 99%). $\text{Li}_2\text{La}_2\text{Ti}_3\text{O}_{10}$ was mixed in a 1:2 molar ratio with NiCl_2 in 100 ml water. The solution was heated at 50 – 65 °C for 8 days with continuous stirring. After 4 days, the powder is separated from the reaction mixture and a fresh nickel chloride solution is added. Phase purity for $\text{Li}_{0.3}\text{Ni}_{0.85}\text{La}_2\text{Ti}_3\text{O}_{10}$ was confirmed by X-ray powder diffraction (XRD). $\text{Li}_{0.3}\text{Ni}_{0.85}\text{La}_2\text{Ti}_3\text{O}_{10}$ was refined on a tetragonal cell with $a = 3.8483(1) \text{ \AA}$ and $c = 26.9871(2) \text{ \AA}$.

Lithium intercalation was performed by reacting $\text{Li}_{0.3}\text{Ni}_{0.85}\text{La}_2\text{Ti}_3\text{O}_{10}$ and n-butyllithium (Aldrich 1.6 M in hexanes) in different molar ratios (1:1, 1:2, 1:4 and 1:10) in inert atmosphere at 60 °C for 3-4 days. The final products were washed with anhydrous hexanes under Ar and then dried under vacuum. The intercalated samples have colors ranging from gray for the lowest lithium content, to black for the sample with the highest lithium content.

5.2.2 Characterization

The inductively coupled plasma emission spectroscopy (ICP) analysis was performed to determine lithium contents. The samples were dissolved in concentrated nitric acid. Standard solutions were prepared from Specpure Alfa Aesar 10,000 $\mu\text{g/ml}$ for lithium. All the standards and the samples were analyzed in a 5% HNO_3 solution (vol./vol.). The composition of the final products corresponded to the general formula $(\text{Li}_x\text{Ni})\text{La}_2\text{Ti}_3\text{O}_{10}$, with $x = 1.100 \pm 0.004$, 2.010 ± 0.008 , 3.710 ± 0.002 and 8.0 ± 0.1 for $\text{Li}_{0.3}\text{Ni}_{0.85}\text{La}_2\text{Ti}_3\text{O}_{10}$ to n-BuLi 1:1, 1:2, 1:4 and 1:10 .

X-ray powder diffraction studies were carried out on a Philips X'Pert System (Cu $K\alpha$ radiation $\lambda=1.5418 \text{ \AA}$) equipped with a graphite monochromator. Data were collected in a continuous scan mode between 5 and $95^\circ 2\theta$. The lattice parameters were refined using POLSQ.^[6]

DC magnetic susceptibility measurements were carried out on a Quantum Design MPMS-5S superconducting quantum interference device (SQUID) magnetometer between 2 and 300 K at 1000 Oe. AC susceptibility was measured using a Quantum Design PPMS between 5 K and 300 K.

5.3 Results

5.3.1 Structure

The intercalation of lithium in $\text{Li}_{0.3}\text{Ni}_{0.85}\text{La}_2\text{Ti}_3\text{O}_{10}$ takes place in a topotactic manner. The tetragonal unit cell shrinks along the c-axis and slightly increases along the

a-axis with increasing lithium content for $(\text{Li}_{1.1}\text{Ni}_{0.85})\text{La}_2\text{Ti}_3\text{O}_{10}$ and $(\text{Li}_{2.01}\text{Ni}_{0.85})\text{La}_2\text{Ti}_3\text{O}_{10}$. Table 5.1 presents the variation of the unit cell parameters and cell volume for the parent, $\text{Li}_{0.3}\text{Ni}_{0.85}\text{La}_2\text{Ti}_3\text{O}_{10}$, $(\text{Li}_{1.1}\text{Ni})\text{La}_2\text{Ti}_3\text{O}_{10}$ and $(\text{Li}_{2.01}\text{Ni})\text{La}_2\text{Ti}_3\text{O}_{10}$. Figure 5.1 presents the X-ray powder patterns for the parent, $\text{Li}_{0.3}\text{Ni}_{0.85}\text{La}_2\text{Ti}_3\text{O}_{10}$ and the lithium intercalated series $(\text{Li}_x\text{Ni})\text{La}_2\text{Ti}_3\text{O}_{10}$. At higher molar ratios, $\text{Li}_{0.3}\text{Ni}_{0.85}\text{La}_2\text{Ti}_3\text{O}_{10}$ to n-BuLi, 1:4 and 1:10, nickel is reduced to nickel metal. This has been found by X-ray diffraction, after annealing the samples in sealed tubes for one day at 350 °C.

5.3.2 DC and ac magnetic susceptibility measurements

The magnetic susceptibility as a function of temperature in a 100 Oe field, and the linear fit of the reciprocal susceptibility versus temperature along with the hysteresis loop at 5 K for $\text{Li}_{1.1}\text{NiLa}_2\text{Ti}_3\text{O}_{10}$ are shown in Figure 5.2. From the linear fit a magnetic moment was calculated, $\mu = 8.7 \mu_B$ and a Weiss constant of 48 K. The variation of the magnetic moment as a function of temperature and the positive Weiss constant, suggest that the transition at 23 K is ferromagnetic. The magnetic susceptibility as a function of temperature in a 100 Oe field, and the linear fit of the reciprocal susceptibility versus temperature along with the hysteresis loop at 5 K for $\text{Li}_{2.01}\text{Ni}_{0.85}\text{La}_2\text{Ti}_3\text{O}_{10}$ are shown in Figure 5.3. From the linear fit a magnetic moment was calculated for $\text{Li}_{2.01}\text{Ni}_{0.85}\text{La}_2\text{Ti}_3\text{O}_{10}$, $\mu = 9.79 \mu_B$ and a Weiss constant of -12.24 K. For the $\text{Li}_{2.01}\text{Ni}_{0.85}\text{La}_2\text{Ti}_3\text{O}_{10}$, the transition at 23 K is suppressed, and the interactions between the magnetic ions seem to be antiferromagnetic.

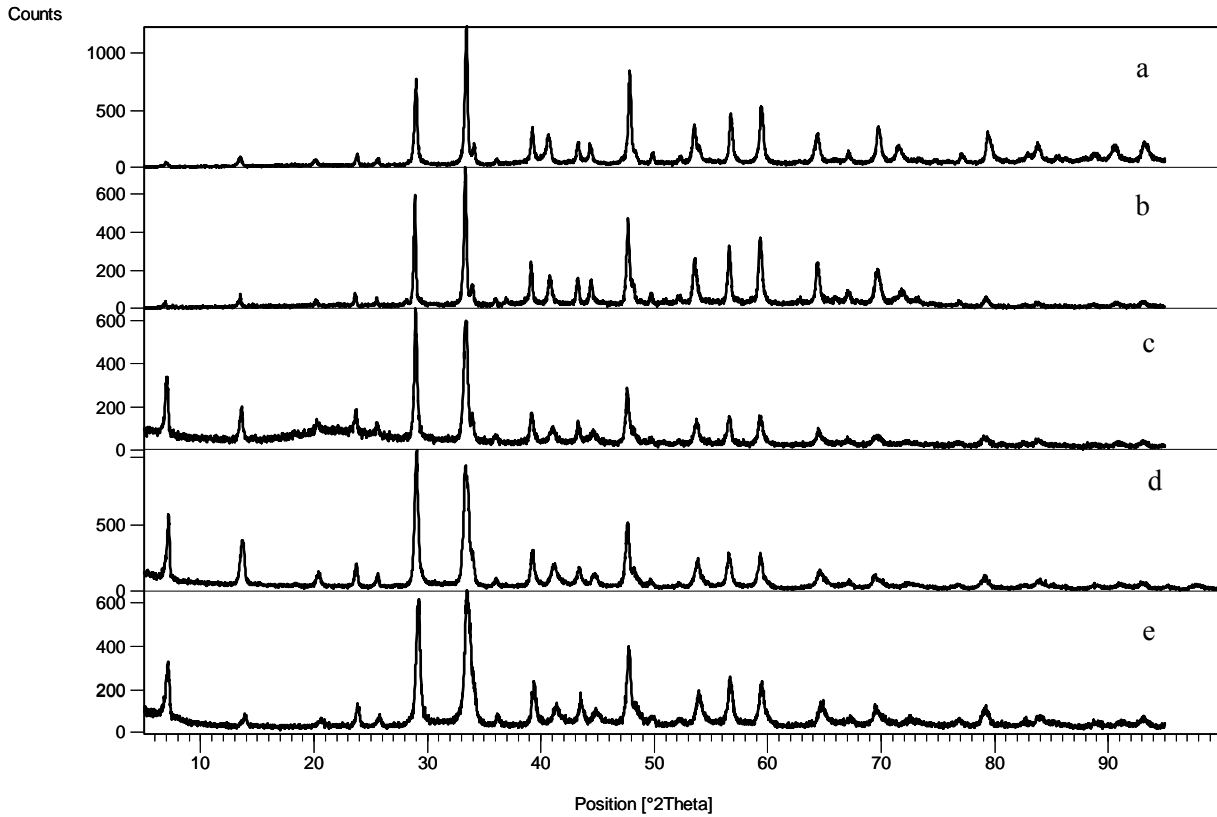


Figure 5.1 X-ray powder patterns for a) $\text{Li}_{0.3}\text{Ni}_{0.85}\text{La}_2\text{Ti}_3\text{O}_{10}$, b) $\text{Li}_{1.1}\text{Ni}_{0.85}\text{La}_2\text{Ti}_3\text{O}_{10}$ c) $\text{Li}_{2.01}\text{Ni}_{0.85}\text{La}_2\text{Ti}_3\text{O}_{10}$ d) $\text{Li}_{3.71}\text{Ni}_{0.85}\text{La}_2\text{Ti}_3\text{O}_{10}$ and e) $\text{Li}_{8.04}\text{Ni}_{0.85}\text{La}_2\text{Ti}_3\text{O}_{10}$.

Table 5.1 Cell parameters based on a tetragonal symmetry for $\text{Li}_{0.3}\text{Ni}_{0.85}\text{La}_2\text{Ti}_3\text{O}_{10}$, $\text{Li}_{1.1}\text{Ni}_{0.85}\text{La}_2\text{Ti}_3\text{O}_{10}$ and $\text{Li}_{2.01}\text{Ni}_{0.85}\text{La}_2\text{Ti}_3\text{O}_{10}$.

Compound	a (Å)	c (Å)	V(Å ³)
$\text{Li}_{0.3}\text{Ni}_{0.85}\text{La}_2\text{Ti}_3\text{O}_{10}$	3.8483(1)	26.9871(2)	399.6(6)
$\text{Li}_{1.100}\text{Ni}_{0.85}\text{La}_2\text{Ti}_3\text{O}_{10}$	3.8656(2)	26.6674(2)	398.4(5)
$\text{Li}_{2.010}\text{Ni}_{0.85}\text{La}_2\text{Ti}_3\text{O}_{10}$	3.8704(3)	26.6076(4)	398.5(3)

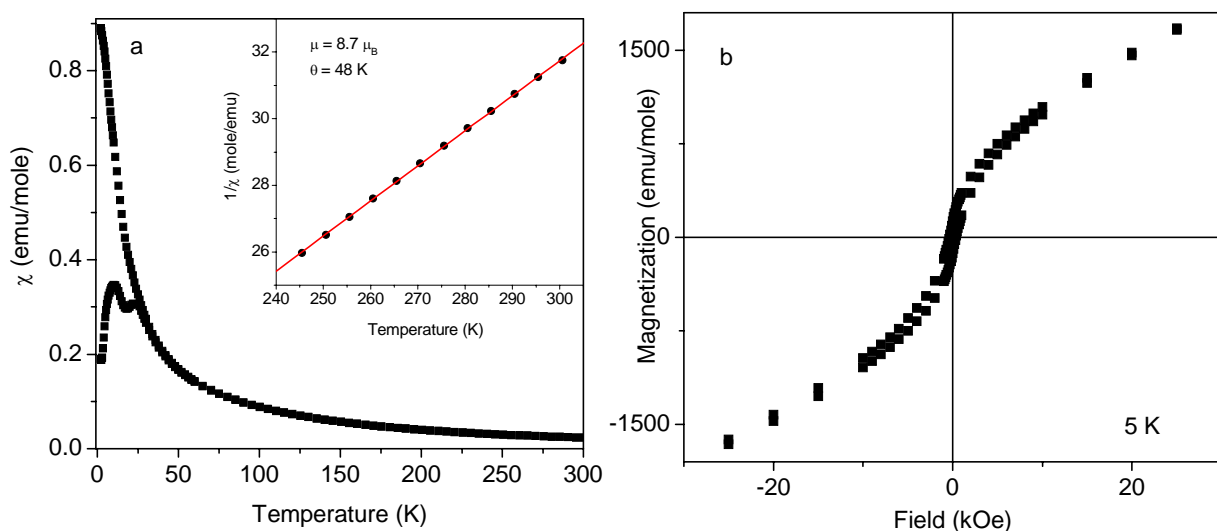


Figure 5.2 Magnetic data for $\text{Li}_{1.1}\text{Ni}_{0.85}\text{La}_2\text{Ti}_3\text{O}_{10}$: a) Susceptibility versus temperature in 100 Oe field; and b) Hysteresis loop at 5 K.

In Figures 5.4 and 5.5 the *ac* susceptibility for $\text{Li}_{1.1}\text{Ni}_{0.85}\text{La}_2\text{Ti}_3\text{O}_{10}$ measurements are presented. It can be seen from these figures, that both of the transitions (10 K and ~ 20-24 K) seen in the parent, $\text{Li}_{0.3}\text{Ni}_{0.85}\text{La}_2\text{Ti}_3\text{O}_{10}$, are present in both the real and the imaginary components of the *ac* susceptibility. In addition, the transitions seem to be frequency dependent. AC measurements performed in a *dc* magnetic field are presented in Figure 5.6 and 5.7. The transition at 10 K varies with the applied *dc* field. Also, the transition at 23 K is suppressed by the applied magnetic field. Both of these transitions seem to be stimulated by the presence of a 100 Oe, *dc* field.

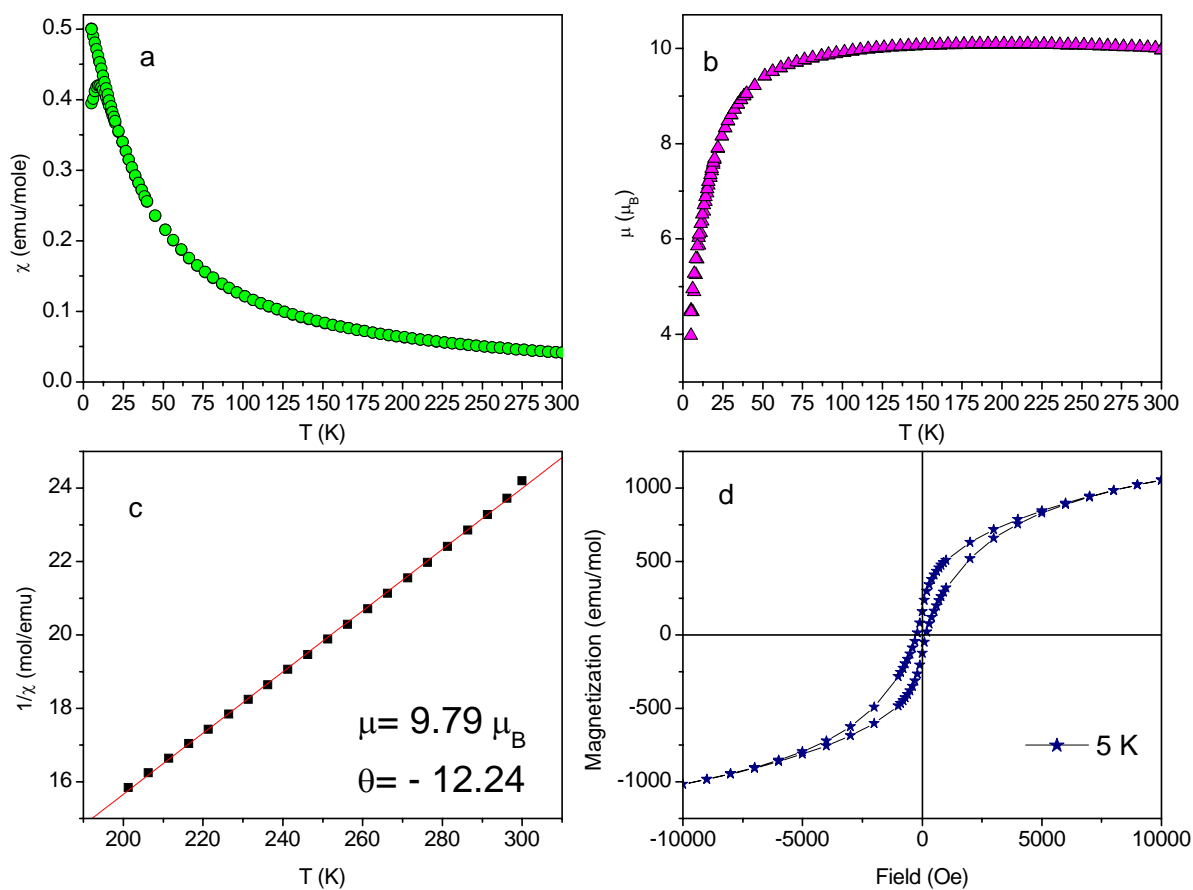


Figure 5.3 The magnetic behavior of $\text{Li}_{2.01}\text{Ni}_{0.85}\text{La}_2\text{Ti}_3\text{O}_{10}$ a) The magnetic susceptibility versus temperature in 100 Oe b) The variation of the magnetic moment with temperature c) The reciprocal susceptibility versus temperature along with the linear fit; d) The hysteresis loop at 5 K.

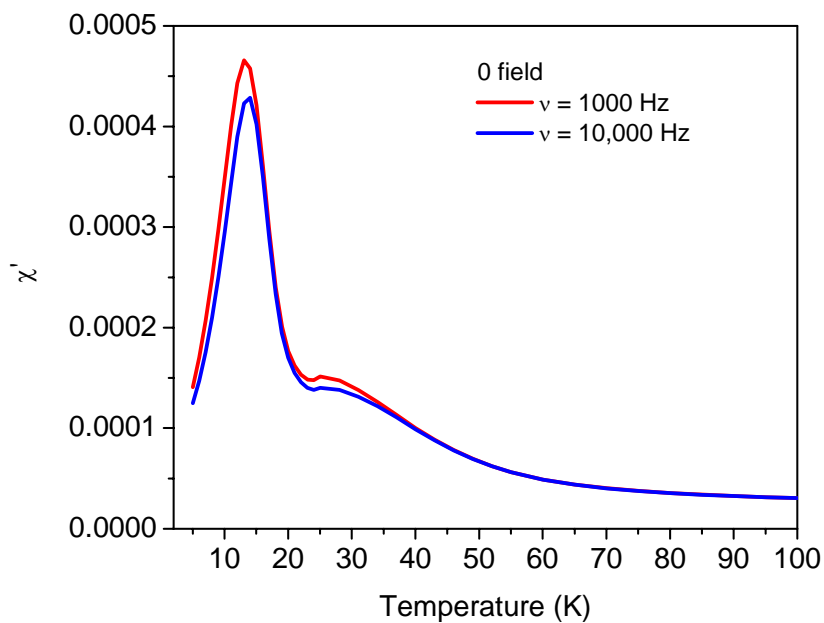


Figure 5.4 The real part of the *ac* susceptibility versus temperature in 0 Oe field for $\text{Li}_{1.1}\text{Ni}_{0.85}\text{La}_2\text{Ti}_3\text{O}_{10}$.

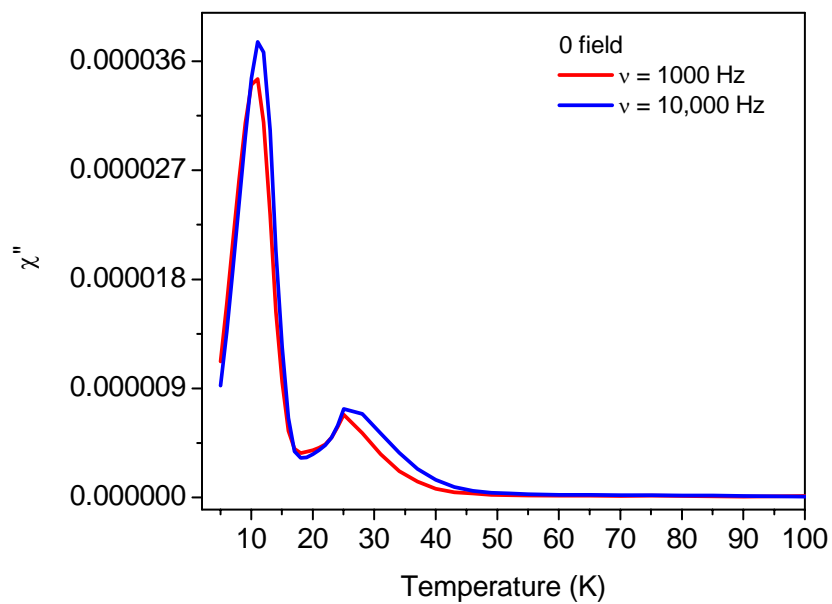


Figure 5.5 The imaginary part of the *ac* susceptibility versus temperature in 0 Oe field for $\text{Li}_{1.1}\text{Ni}_{0.85}\text{La}_2\text{Ti}_3\text{O}_{10}$.

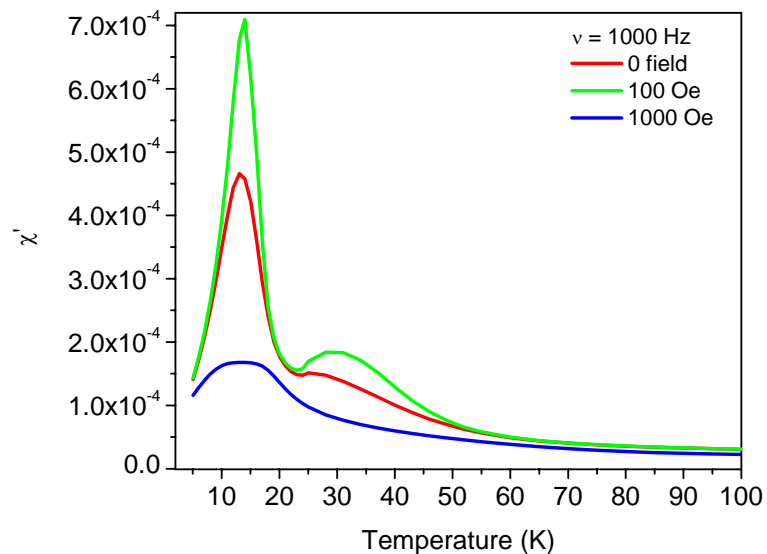


Figure 5.6 The real part of the *ac* susceptibility versus temperature in 0, 100 and 1000 Oe field for $\text{Li}_{1.1}\text{Ni}_{0.85}\text{La}_2\text{Ti}_3\text{O}_{10}$.

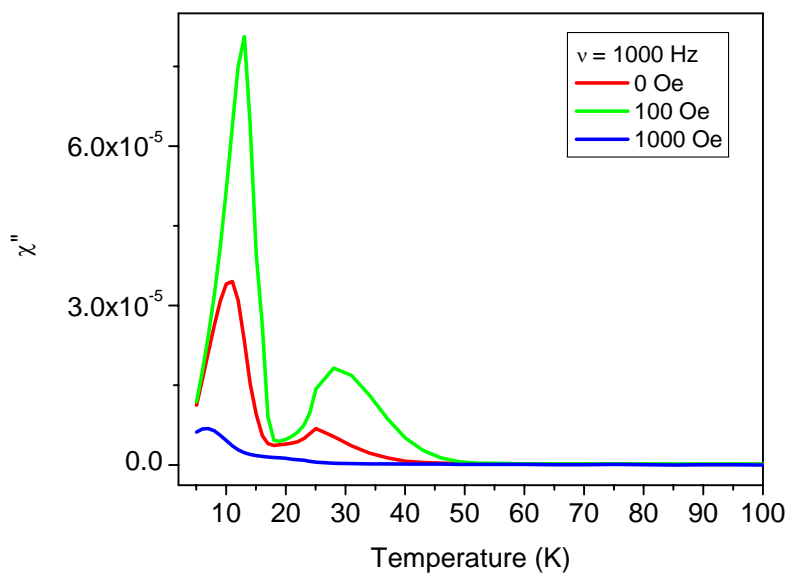


Figure 5.7 The imaginary part of the *ac* susceptibility versus temperature in 0, 100 and 1000 Oe field for $\text{Li}_{1.1}\text{Ni}_{0.85}\text{La}_2\text{Ti}_3\text{O}_{10}$.

In Figures 5.8 and 5.9 the ac susceptibility for $\text{Li}_{2.01}\text{Ni}_{0.85}\text{La}_2\text{Ti}_3\text{O}_{10}$ measurements are presented. It can be seen from these figures, that only one transition, at 9 K, is present in both the real and the imaginary components of the *ac* susceptibility. In addition, the transition seems to be frequency dependent. *AC* measurements performed in a *dc* magnetic field are presented in Figure 5.10. The transition at 9 K is rounded by the applied magnetic field.

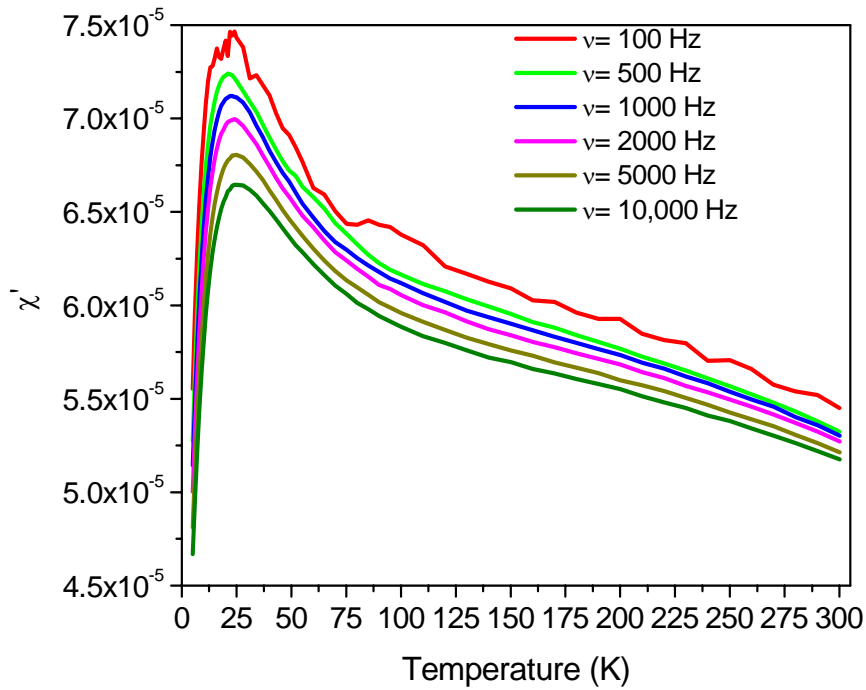


Figure 5.8 The real part of the *ac* susceptibility versus temperature in 0 Oe *dc* field for $\text{Li}_{2.01}\text{Ni}_{0.85}\text{La}_2\text{Ti}_3\text{O}_{10}$.

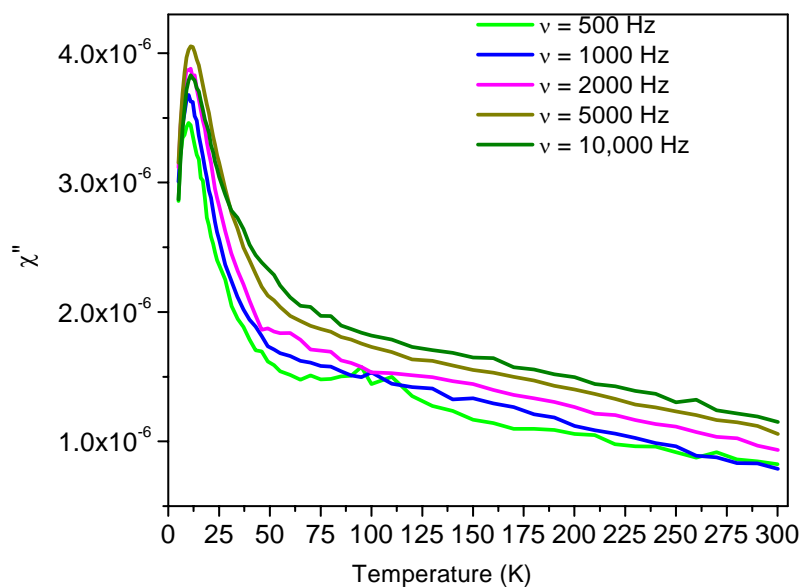


Figure 5.9 The imaginary part of the *ac* susceptibility versus temperature in 0 Oe dc field for $\text{Li}_{2.01}\text{Ni}_{0.85}\text{La}_2\text{Ti}_3\text{O}_{10}$.

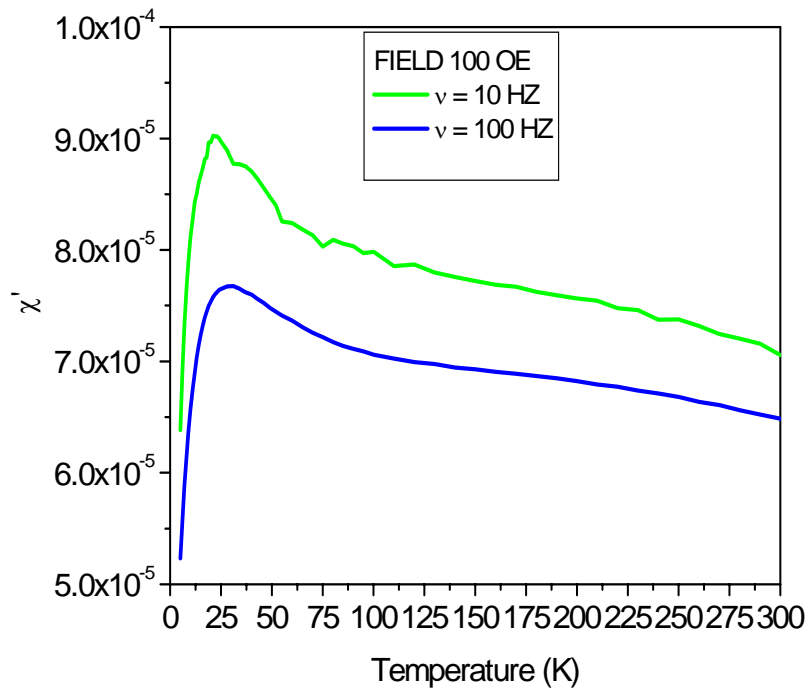


Figure 5.10 The real part of the *ac* susceptibility versus temperature in 100 Oe field for $\text{Li}_{2.01}\text{Ni}_{0.85}\text{La}_2\text{Ti}_3\text{O}_{10}$.

5.3.3 Band Structure Calculations

The changes that lithium content causes in $(\text{Li}_x\text{Ni})\text{La}_2\text{Ti}_3\text{O}_{10}$ have been also followed by extended Hückel calculations performed using the YAEHMOP software package.^[7] In Figure 5.11 are shown the density of states for $(\text{Li}_{1.1}\text{Ni}_{0.85})\text{La}_2\text{Ti}_3\text{O}_{10}$ and $(\text{Li}_{2.01}\text{Ni}_{0.85})\text{La}_2\text{Ti}_3\text{O}_{10}$. The valence band is occupied by nickel 4s states. The Fermi level energy increases with increasing lithium content.

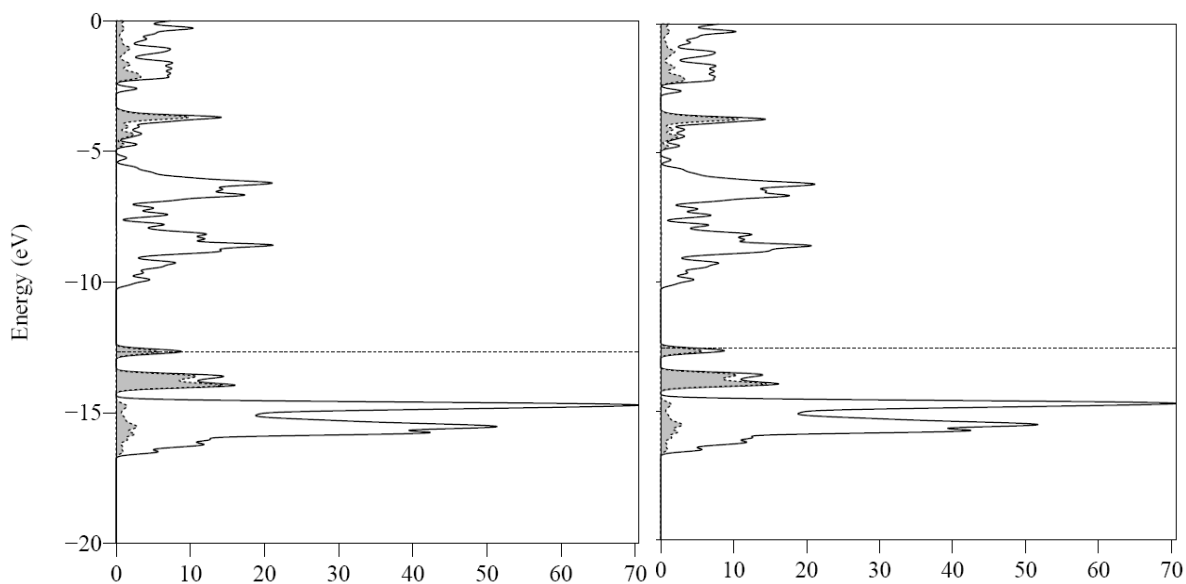


Figure 5.11 The density of states (DOS) for $(\text{Li}_{1.1}\text{Ni}_{0.85})\text{La}_2\text{Ti}_3\text{O}_{10}$ and $(\text{Li}_{2.01}\text{Ni}_{0.85})\text{La}_2\text{Ti}_3\text{O}_{10}$. The Fermi level is indicated by the dashed horizontal line at -12.68 eV and -12.57 eV, respectively. The total DOS are represented by a solid line. The grey area represents nickel DOS.

5.4 Discussion

Lithium intercalation in the $\text{Li}_{0.3}\text{Ni}_{0.85}\text{La}_2\text{Ti}_3\text{O}_{10}$ takes place in a topotactic manner. The unit cell of the parent contracts along the c axis and expands along the a axis upon intercalation for $\text{Li}_{1.1}\text{Ni}_{0.85}\text{La}_2\text{Ti}_3\text{O}_{10}$ and $\text{Li}_{2.01}\text{Ni}_{0.85}\text{La}_2\text{Ti}_3\text{O}_{10}$. This type of behavior has been seen for other lithium intercalated compounds.^[4] Lithium intercalates in the $\text{Li}_{0.3}\text{Ni}_{0.85}\text{La}_2\text{Ti}_3\text{O}_{10}$ in a comparable amount with $(\text{VO})\text{La}_2\text{Ti}_3\text{O}_{10}$ for the same molar ratio parent to $n\text{-BuLi}$ (1:1 and 1:2). The higher lithium content samples contain nickel metal.

In terms of their magnetic behavior, $\text{Li}_{1.1}\text{Ni}_{0.85}\text{La}_2\text{Ti}_3\text{O}_{10}$, retains the two magnetic transitions seen in the parent, $\text{Li}_{0.3}\text{Ni}_{0.85}\text{La}_2\text{Ti}_3\text{O}_{10}$. The magnetic moment increases upon lithium intercalation from $2.97 \mu_B$ for $\text{Li}_{0.3}\text{Ni}_{0.85}\text{La}_2\text{Ti}_3\text{O}_{10}$ to $8.7 \mu_B$ for $\text{Li}_{1.1}\text{Ni}_{0.85}\text{La}_2\text{Ti}_3\text{O}_{10}$. This can be attributed to the reduction of Ti^{4+} (d^0) to Ti^{3+} (d^1). Based on the ICP composition of this compound, 30% of the titaniums have been reduced to Ti^{3+} . This gives an average oxidation state for the Ti in the perovskite layers of +3.6. Also due to this reduction, the ferromagnetic interactions in this compound intensify. This claim is supported by the Weiss constant value, which also increases upon intercalation from 5 K in $\text{Li}_{0.3}\text{Ni}_{0.85}\text{La}_2\text{Ti}_3\text{O}_{10}$ to 48 K in $\text{Li}_{1.1}\text{Ni}_{0.85}\text{La}_2\text{Ti}_3\text{O}_{10}$. Zener suggested that in a mixed valence compound, the interactions between the magnetic ions take place via a double exchange mechanism.^[7] Also, he proved that for the lowest energy configuration corresponds to a ferromagnetic arrangement of spins on the transition metal in the two oxidation states (here titanium is in a 4+ and in a 3+ oxidation state). Moreover, this ferromagnetic interaction is strongest when the angle between the

$\text{Ti}^{4+} - \text{O}^{2-} - \text{Ti}^{3+}$ is 180° , which is the case for $\text{Li}_{1.1}\text{Ni}_{0.85}\text{La}_2\text{Ti}_3\text{O}_{10}$.^[6] In the zero dc field *ac* susceptibility measurement, both of the transitions are present in the in phase and out of phase components. The transitions are frequency dependent, and therefore they could be either ferromagnetic or spin glass like.^[9] In 1000 Oe, the *ac* susceptibility behavior changes as compared with the parent, $\text{Li}_{0.3}\text{Ni}_{0.85}\text{La}_2\text{Ti}_3\text{O}_{10}$. Both of the transitions round with the applied *dc* field, which suggests not only that the frustration existent in the parent is retained but also that lithium intercalation induces more frustration in the magnetic interactions. This could be due to the disorder (50% occupancy on the nickel site in $\text{Li}_{1.1}\text{Ni}_{0.85}\text{La}_2\text{Ti}_3\text{O}_{10}$) and geometric magnetic frustration because of $\text{Ni}^{2+} - \text{O}^{2-} - \text{Ti}^{3+}$ interlayer interactions. It is worth noticing that a magnetic field of 100 Oe greatly stimulates both of the transitions. It is possible that this field corresponds to the energy necessary for the spins to exist in a more stable configuration.

Upon increasing lithium content from $\text{Li}_{1.1}\text{Ni}_{0.85}\text{La}_2\text{Ti}_3\text{O}_{10}$ to $\text{Li}_{2.01}\text{Ni}_{0.85}\text{La}_2\text{Ti}_3\text{O}_{10}$, an even more intriguing magnetic behavior is obtained. The magnetic moment increases to $9.79 \mu_B$ and the Weiss constant is -12.24 K, which suggests antiferromagnetic interactions. The mean oxidation state for titanium in $\text{Li}_{2.01}\text{Ni}_{0.85}\text{La}_2\text{Ti}_3\text{O}_{10}$ is +3.3. This compound has only one magnetic transition at 9 K. The *ac* susceptibility data reveals also only one frequency dependent transition in both the real and the imaginary part. Also in the *dc* field *ac* measurement, this transition rounds even with small *dc* fields.^[9-11] This is a typical spin glass transition, from a paramagnetic state with weak antiferromagnetic interactions into a frustrated spin glass state.^[9-11] It is most likely that upon increasing lithium content, increasing $\text{Ti}^{3+}/\text{Ti}^{4+}$ ratio, the interactions between the magnetic layers (the perovskite block and the interlayer strata) become more competitive.

5.5 References

- [1] Schaak, R. E. and Mallouk, T. E. *J. Am. Chem. Soc.* **2000**, *122*, 2798.
- [2] Lalena, J.N.; Cushing, B.L.; Falster, A.U.; Simmons, W.B. Jr.; Seip, C.T.; Carpenter, E.E.; O'Connor, C.J. and Wiley, J. B. *Inorg. Chem.* **1998**, *37*, 4484.
- [3] Toda, K.; Watanabe, J.; Sato, M. *Mat. Res. Bull.* **1996**, *31*, 1427.
- [4] Neiner, D. Sweany, R. L. Golub, V. and Wiley, J. B. in the Proceedings of the MRS Fall Meeting, Boston, MA, **2004**, 848 FF9.3.
- [5] Toda, K.; Watanabe, J.; Sato, M. *Materials Research Bulletin* **1996**, *31*, 1427.
- [6] Ibers, D. A. and J. A. Modified POLSQ, Department of Chemistry, Northwestern University, Evanston, IL, **1983**.
- [7] Landrum, G. and Hoffman, R. *Yet Another Extended Hückel Molecular Orbital Package (YAEHMOP)*, <http://yaehmop.sourceforge.net/>
- [8] Zener, C. *Phys. Rev.* **1951**, *82*, 403.
- [9] Carlin, R. L. *Magnetochemistry*, Springer-Verlag Berlin Heidelberg, 1986.
- [10] Moorjani, K.; Coey, J. M. D. *Magnetic glasses*, Elsevier Science Publishers B. V., 1984.
- [11] Greedan, J. E. *J. Mater. Chem.* **2001**, *11*, 37.

Chapter 6

Vanadyl insertion and lithium intercalation in the single layered RP, NaGdTiO₄

6.1 Introduction

Layered perovskites of the Dion-Jacobson (DJ), $A'[A_{m-1}B_mO_{3m+1}]$, and Ruddlesden-Popper (RP), $A'_2[A_{m-1}B_mO_{3m+1}]$, families, where A' = alkali or alkali earth metal, A = rare earth or alkaline metal, B = transition metal, and m is the number of perovskite blocks. The reactivity of the A' cations make these compounds effective precursors to new low temperature phases via topochemical routes. Ion exchange reactions with the single-layered perovskite, NaLaTiO₄, have also resulted in a series of new compounds. Monovalent exchange has produced KLaTiO₄, AgLaTiO₄ (α and β forms) and HLaTiO₄. Divalent exchange has resulted in alkaline, Ca_{0.5}LaTiO₄, and transition metal, M_{0.5}LaTiO₄ ($M = Cu, Co, Zn$) RP oxides.^[1-4] Gopalakrishnan and coworkers investigated the triple-layered perovskite, K₂La₂Ti₃O₁₀ and reported initial studies on the ion exchange of vanadyl species.^[5] Also, we reported an ion exchange route via a solution reaction in NaLaTiO₄ to produce Na_{0.1}(VO)_{0.45}LaTiO₄.^[6] Herein we expand on this approach with a detailed study on the synthesis and characterization of the new single-layered perovskite, Na_{0.05}(VO)_{0.48}GdTiO₄. After the ion exchange step reductive intercalation with n-BuLi was performed to form Li_{1.056}Na_{0.05}(VO)_{0.48}GdTiO₄.

6.2 Experimental

6.2.1. Synthesis

NaGdTiO₄ was synthesized by conventional solid-state reaction with a method similar to that of Toda *et al.*^[7] Initially, Gd₂O₃ (Alfa Aesar, 99.99%) was preheated to 1000 °C for 16 hrs. before use to remove any hydroxide and carbonate contaminates. Then stoichiometric amounts of La₂O₃ and TiO₂ (Alfa Aesar, 99.99%) were combined with a 40% molar excess of Na₂CO₃ (Alfa Aesar, 99.99%) and heated in an alumina crucible at 950 °C for 30 minutes. The final product was washed with warm water, rinsed with acetone and dried at 150 °C overnight. Phase purity for NaGdTiO₄ was confirmed by X-ray powder diffraction (XRD). NaGdTiO₄ was indexed on the tetragonal unit cell $a = 3.7144(1) \text{ \AA}$ and $c = 12.2289(2)$, which is in agreement with the values reported in the literature.^[7]

Ion exchange was used to substitute the Na ions in NaGdTiO₄ with vanadyl ions, (VO)²⁺. The source of the vanadyl unit was vanadyl sulfate hydrate (VOSO₄·nH₂O, Alfa Aesar, 99.99%). NaGdTiO₄ was mixed in a 1:1.5 molar ratio with VOSO₄ in 150 ml water. The solution was heated for 48 hours at 50 °C with continuous stirring. The final product was dark green in color. Na_{0.05}(VO)_{0.48}GdTiO₄ was then lithium intercalated. The reaction was performed with n-BuLi in inert atmosphere, using a 1:2 molar ratio. The reaction mixture was stirred for 4 days at room temperature in inert atmosphere. The product was separated by vacuum filtration. The Li_{1.056}Na_{0.05}(VO)_{0.48}GdTiO₄ compound is black.

6.2.2. Characterization

The $\text{Na}_{0.05}(\text{VO})_{0.48}\text{GdTiO}_4$ phase could not be completely dissolved in a variety of strong acids. So, to analyze the extent of exchange, the exchange solution after reaction was analyzed for the sodium byproduct and unreacted vanadyl. The analysis was carried out by inductively coupled plasma spectrometry (ICP). Standard solutions were prepared from Specpure Alfa Aesar 10,000 $\mu\text{g/ml}$ for sodium and vanadium. All the standards and the samples were analyzed in a 5% HNO_3 solution (vol./vol.). For the lithium intercalated compound, $\text{Li}_{1.056}\text{Na}_{0.05}(\text{VO})_{0.48}\text{GdTiO}_4$ the samples were dissolved in 25 ml volumetric flask using 70% HNO_3 , heated with stirring for 2-3 days. Then, part of this solution was diluted to 5% HNO_3 .

X-ray powder diffraction studies were carried out on a Phillips X'Pert System (Cu $K\alpha$ radiation $\lambda=1.5418 \text{ \AA}$) equipped with a graphite monochromator. Data were collected in a step scan mode between 2 and $95^\circ 2\theta$ with a step size of 0.02° and a counting time of 10 s. Structural refinement was done by the Rietveld method with the GSAS package of programs.^[8] Thirty-nine parameters were varied including background, peak shape, cell, atom positions, thermal parameters and occupancies. In the beginning of the refinement, the Le Bail method^[9] was employed for the background and peak shape parameters. The R-factor (R_p), the weighted R-factor (wR_p), and the goodness of fit, χ^2 , are defined as: $R_p = \sum [y_{io} - y_{ic}] / \sum y_{io}$, $wR_p = [\sum w_i (y_{io} - y_{ic})^2 / \sum w_i (y_{io})^2]^{1/2}$, $R_F = \sum [|I_k(\text{obs})|^{1/2} - |I_k(\text{calc})|^{1/2}] / [\sum |I_k(\text{obs})|^{1/2}]$, and $\chi^2 = [wR_p / R_{\text{exp}}]^2$, where $R_{\text{exp}} = [(N - P) / \sum w_i y_{io}^2]^{1/2}$ and y_{io} and y_{ic} are the observed and the calculated intensities, w_i is the weighting factor, N is the total number of observed intensities when the background is refined, and P is the number of adjusted parameters.

Infrared spectroscopy (IR) was performed on a Perkin Elmer 2000 FT-IR; the samples were analyzed as pellets in a 1:100 molar ratio with dry KBr. Magnetic measurements were performed on a Quantum Design MPMS-5S Superconducting Quantum Interference Device (SQUID) magnetometer between 2 and 300 K at 1000 Oe. Thermal behavior was studied on a TGA 51 thermogravimetric analyzer and a Netzsch 404 S differential scanning calorimeter (DSC); measurements were performed in oxidizing, inert and reducing atmospheres between room temperature and 800 °C by heating samples at 10 °C/min in O₂, Ar and H₂ (8% hydrogen in argon), respectively.

6.3 Results

6.3.1. Synthesis

Ion exchange reactions were performed between NaGdTiO₄ and aqueous vanadyl sulfate solutions. XRD indicated that the reaction was complete after 48 hours when carried out at 50 °C. Heating at temperatures higher than 70 °C leads to the formation of a GdVO₄ impurity phase. ICP was used to determine sodium and vanadium contents. This elemental analysis shows a composition of Na:V:Gd:Ti = 0.05:0.48:1:1 corresponding to Na_{0.050±0.007}(VO)_{0.48±0.05}GdTiO₄. This compound was then intercalated with lithium. The intercalation reaction is accompanied by a color change from green Na_{0.05}(VO)_{0.48}GdTiO₄ to black Li_xNa_{0.05}(VO)_{0.48}GdTiO₄. ICP analysis showed that lithium content was $x = 1.056 \pm 0.009$.

6.3.2. Structure

Ion exchange takes place in a topotactic manner in that the structure of the perovskite host is maintained. Figure 6.1 presents the crystal structures of $\text{Na}_{0.05}(\text{VO})_{0.48}\text{GdTiO}_4$. Figure 6.2 shows a comparison of the X-ray powder diffraction patterns before and after exchange for the single layered RP perovskite. Table 6.1 shows the variation in unit cell parameters and cell volume. The cells have been refined using POLSQ.^[10] There is about a 4 % reduction in cell volume on exchange with the greatest change occurring in the c direction (contraction $\sim 0.4 \text{ \AA}$). This contraction can be understood knowing that two sodium ions are replaced with one vanadyl cationic unit.

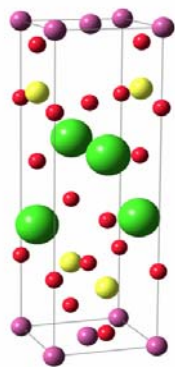


Figure 6.1 Idealized crystal structure for $\text{Na}_{0.05}(\text{VO})_{0.48}\text{GdTiO}_4$. V atoms are represented with purple, Gd with green, Ti with yellow and oxygen with red. Sodium atoms are not represented.

Structural refinement of $\text{Na}_{0.05}(\text{VO})_{0.48}\text{GdTiO}_4$ was carried out by the Rietveld method. The starting model was based on NaGdTiO_4 , where the atomic positions of lanthanum, titanium and oxygen were kept the same as in the parent except that sodium was replaced with vanadium at $2c (0\ 0\ z)$ with 48% occupancy. An idealized crystal structure is presented in Figure 6.1. The occupancy for vanadium was maintained constant at 48% during the Rietveld refinement. While this model produced reasonable

agreement factors and most of the atoms were well behaved, χ^2 is still large. The observed, calculated and difference plots for the refinement are shown in Figure 6.3 and the structural information is provided in Table 6.2.

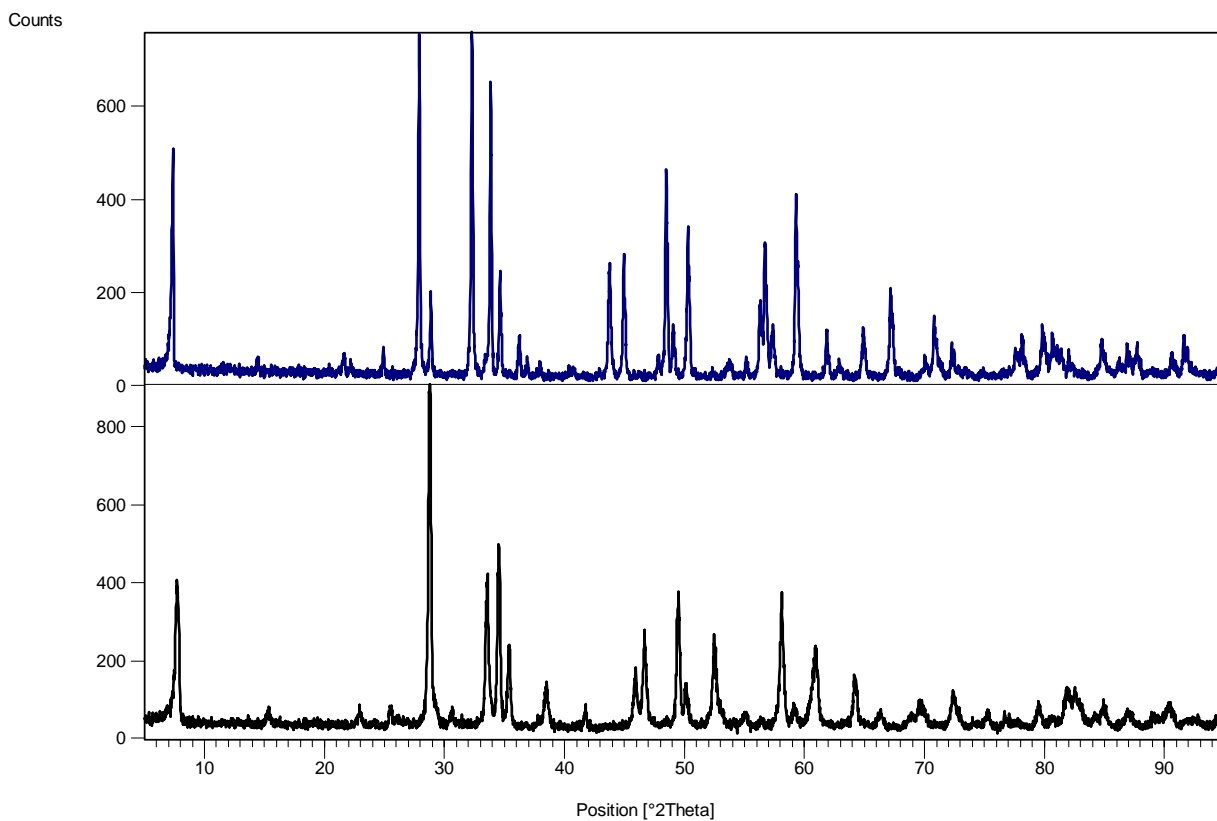


Figure 6.2 XRD powder patterns for NaGdTiO₄ (top) and Na_{0.05}(VO)_{0.48}GdTiO₄ (bottom).

Table 6.1 Refined unit cell parameters for NaGdTiO_4 , $\text{Na}_{0.05}(\text{VO})_{0.48}\text{GdTiO}_4$ and $\text{Li}_{1.056}\text{Na}_{0.05}(\text{VO})_{0.48}\text{GdTiO}_4$.

Compounds	Unit cell parameters		Cell volume
	a (Å)	c (Å)	V (Å ³)
NaGdTiO_4 this work	3.7144(1)	12.2289(2)	168.71
$\text{Na}_{0.05}(\text{VO})_{0.48}\text{GdTiO}_4$	3.7075(4)	11.7898(2)	162.03
$\text{Li}_{1.056}\text{Na}_{0.05}(\text{VO})_{0.48}\text{GdTiO}_4$	3.7798(1)	11.2413(2)	160.60

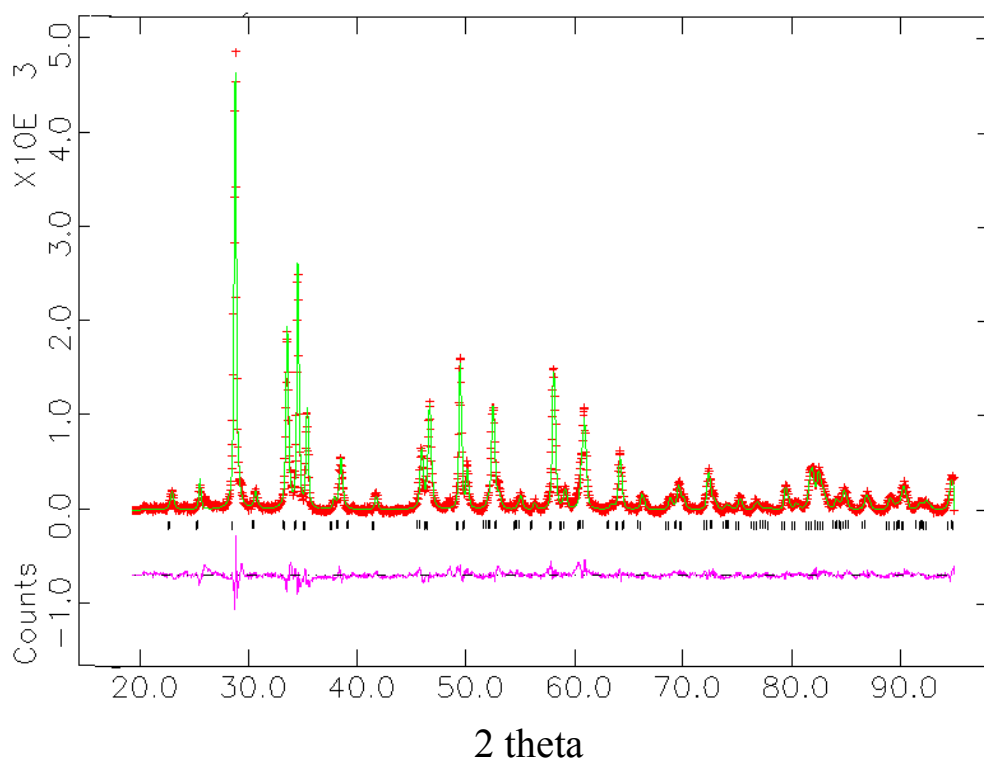


Figure 6.3 Rietveld refinement of $\text{Na}_{0.05}(\text{VO})_{0.48}\text{GdTiO}_4$. Observed data is indicated with crosses, calculated pattern as a solid line, and the difference is indicated at the bottom.

Table 6.2 Crystallographic data for $\text{Na}_{0.05}(\text{VO})_{0.48}\text{GdTiO}_4$ ^a

Atom	Site	x	y	z	g^b	U_{iso}
Gd	2c	0.75	0.75	0.3856(1)	1.001(2)	0.012(2)
Ti	2c	0.25	0.25	0.2100(2)	1.030(7)	0.016(1)
O 1	4f	0.75	0.25	0.7596(6)	0.990(2)	0.026(3)
O 2	2c	0.75	0.75	0.5843(1)	1.040(2)	0.015(3)
O 3	2c	0.75	0.75	0.9472(1)	1.070(2)	0.028(3)
V	2a	0.25	0.25	0.04900	0.48	0.090(1)

^a P4/nmm (2nd choice of origin); $Z = 2$, $R_p = 8.18\%$, $wR_p = 10.68\%$, $\chi^2 = 3.08$, $R_F^2 = 12.77\%$; ^b occupancy.

6.3.3. Thermal analysis

Above 300 °C, $\text{Na}_{0.05}(\text{VO})_{0.48}\text{GdTiO}_4$ starts to degrade. XRD shows that GdVO_4 starts to form around 460 °C and at 700 °C is the predominant phase. The same behavior was observed in oxidizing atmosphere. In reducing atmosphere, the material starts the formation of GdVO_3 above 220 °C, and this is the predominant phase up to 800 °C.

6.3.4. IR data.

The presence of the VO unit in the structure is supported by the IR spectra, which show the characteristic stretching band at around 1006 cm^{-1} . This is in agreement with the accepted range for a vanadyl stretch, $950 - 1035\text{ cm}^{-1}$.^[5,6] A comparable value was observed in the triple layered RP $(\text{VO})\text{La}_2\text{Ti}_3\text{O}_{10}$ and for $\text{Na}_{0.1}(\text{VO})_{0.45}\text{LaTiO}_4$.^[5, 6] IR also supports the presence of water in $\text{Na}_{0.05}(\text{VO})_{0.48}\text{GdTiO}_4$ showing the corresponding stretching bands of water around 1600 and 3400 cm^{-1} .

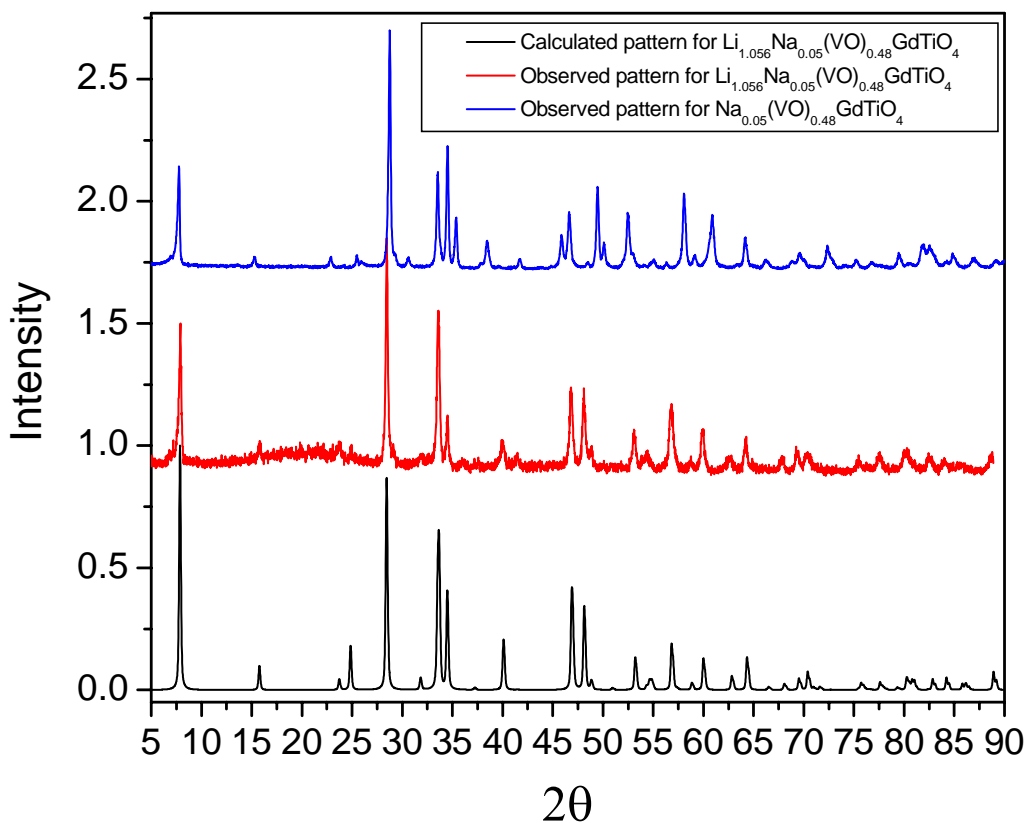


Figure 6.4 Calculated (bottom), observed (middle) powder patterns for $\text{Li}_{1.056}\text{Na}_{0.05}(\text{VO})_{0.48}\text{GdTiO}_4$ and for $\text{Na}_{0.05}(\text{VO})_{0.48}\text{GdTiO}_4$ (top).

6.3.5. Magnetic data

Magnetic susceptibility data for $\text{Na}_{0.05}(\text{VO})_{0.48}\text{GdTiO}_4$ is shown in Figure 6.5. Measurements were performed in a field of 1000 Oe as a function of temperature. The compound is paramagnetic and exhibits Curie-Weiss behavior (Figure 6.5, inset). The Curie-Weiss constant and magnetic moment calculated from the fitted data are $\theta = -8.06$ K and $\mu_{\text{eff}} = 8.95 \mu_{\text{B}}$ per formula unit of $\text{Na}_{0.05}(\text{VO})_{0.48}\text{GdTiO}_4$.

The lithium-intercalated compound undergoes a paramagnetic to ferromagnetic transition at 6 K. The susceptibility versus temperature is presented in Figure 6.6 and the hysteresis loop at 2 K in Figure 6.7.

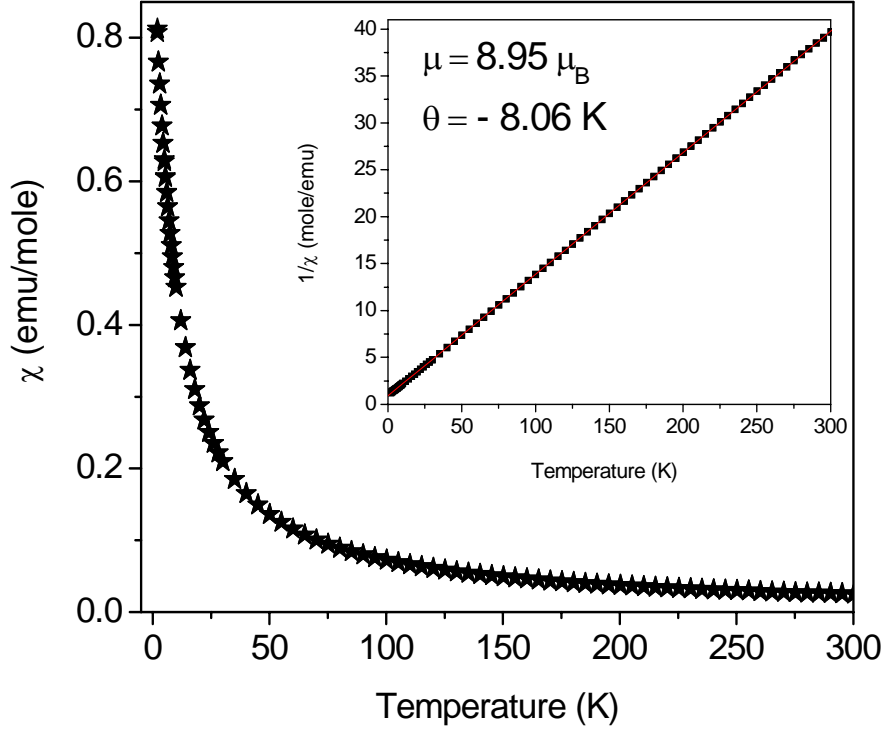


Figure 6.5 Temperature dependence of magnetic susceptibility in 1000 Oe for $\text{Na}_{0.05}(\text{VO})_{0.48}\text{GdTiO}_4$. The inset represents the reciprocal susceptibility versus temperature and the solid line is the result of the linear fit.

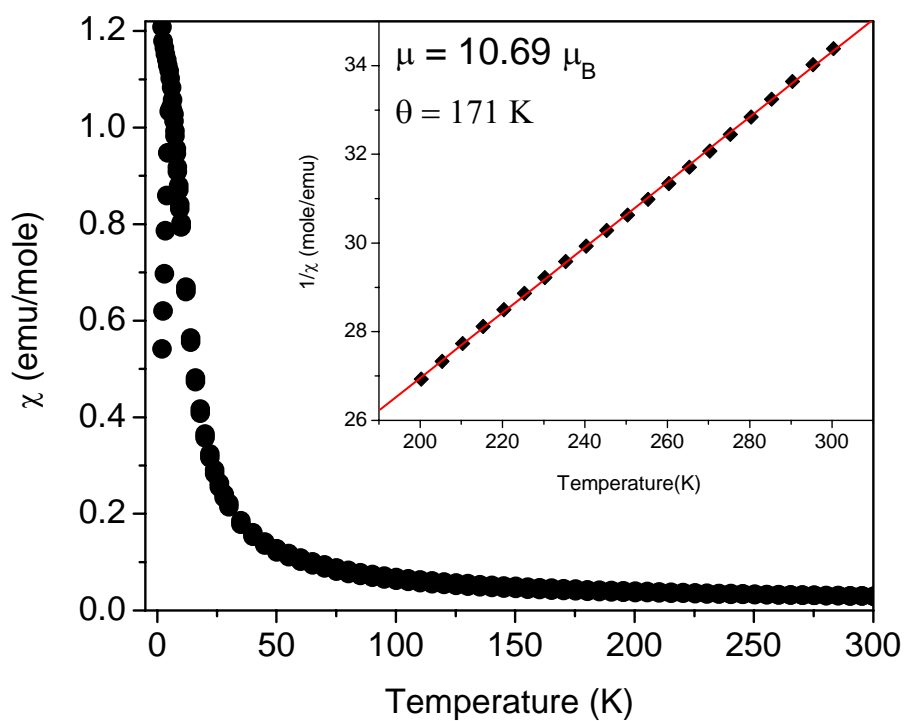


Figure 6.6 Temperature dependence of magnetic susceptibility in 1000 Oe for $\text{Li}_{1.056}\text{Na}_{0.05}(\text{VO})_{0.48}\text{GdTiO}_4$. The inset represents the reciprocal susceptibility versus temperature and the solid line is the result of the linear fit.

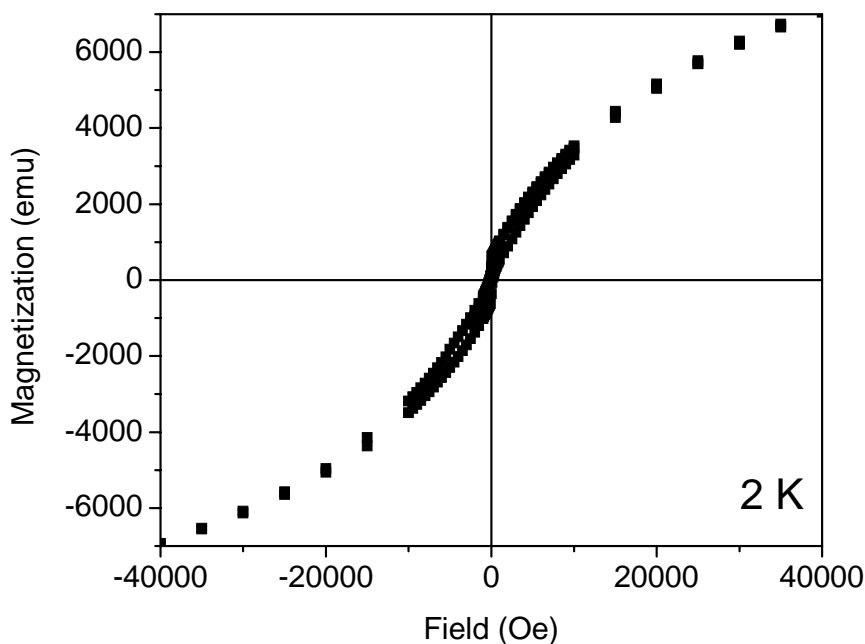


Figure 6.7 Hysteresis loop for $\text{Li}_{1.056}\text{Na}_{0.05}(\text{VO})_{0.48}\text{GdTiO}_4$ at 2 K.

6.4 Discussion

A vanadyl unit has been inserted in the single layered RP, NaGdTiO_4 . The exchange occurs with structure retention. The vanadium ion is in a tetrahedral site relative to the perovskite blocks. Vanadyl exchange for sodium occurs with a considerable cell contraction. This happens because in order for the charge balance to be maintained, for every two sodium ions that leave the structure there is only one vanadyl unit, $(\text{VO})^{2+}$, that enters the interlayer space. At the same time, this exchange opens the structure to further chemistry. This is done by a reductive intercalation step when Ti^{4+} is reduced to Ti^{3+} .

Thermal analysis shows that $\text{Na}_{0.05}(\text{VO})_{0.48}\text{GdTiO}_4$ is low temperature phase. The changes seen above 300 °C can be attributed to the instability of V^{4+} versus V^{5+} with increasing temperature. At 800 °C, GdVO_4 is the predominate crystalline phase in both inert and oxidizing atmospheres.

In terms of magnetic properties, $\text{Na}_{0.05}(\text{VO})_{0.48}\text{GdTiO}_4$ is a Curie-Weiss paramagnet with a magnetic moment of $8.95 \mu_B$ and a Weiss constant of - 8.06 K, which suggests weak antiferromagnetic interactions. This value is higher than expected for two non-interacting magnetic ions, $\mu_{total} = (\mu_{Gd}^2 + \mu_{VO}^2)^{1/2} = (7.9^2 + 1.73^2)^{1/2} = 8.08 \mu_B$. The magnetic moment for NaGdTiO_4 is $7.89 \mu_B$.^[12] Also, the parent, NaGdTiO_4 follows Curie law.^[12] It is most likely that the antiferromagnetic interactions take place between the vanadyl units. The IR stretching frequency for the vanadyl units is in agreement with little exchange between vanadium ions. This has also been seen in $\text{Na}_{0.05}(\text{VO})_{0.45}\text{LaTiO}_4$. It is reasonable to assume that there are no interactions between the Gd^{3+} (f^7) and the V^{4+} (d^1) electrons given the fact that there is a layer of isolating Ti^{4+} (d^0) between the two. The compound formed by lithium reductive intercalation, $\text{Li}_{1.056}\text{Na}_{0.05}(\text{VO})_{0.48}\text{LaTiO}_4$ has more complicated magnetic interactions. Now the system contains three magnetic ions, V^{4+} , Gd^{3+} and Ti^{3+} . The ZFC/FC split and there is a transition at 6 K. Also, there is a hysteresis loop below this transition and a positive Weiss constant indicating ferromagnetic interactions. Because of the high $\theta/T_C \cong 28$ value, there is a high degree of frustration in the magnetic interactions.

6.5 References

- [1] Kim, S. Y.; Oh, J. M.; Park, J. C.; Byeon, S. H. *Chem. Mater.* **2002**, *14*, 1643.
- [2] Schaak R. E. and Mallouk, T. *J. Solid State Chemistry* **2001**, *161*, 225.
- [3] Toda, K.; Kurita, S.; Sato, M. *Solid State Ionics* **1995**, *81*, 267.
- [4] Byeong, Song-Ho; Yoon, Jong-Jin; Lee, Sung-Ohk. *Journal of Solid State Chemistry* **1996**, *127(1)*, 119.
- [5] Gopalakrishnan, J.; Sivakumar, T.; Ramesha, K.; Thangadurai, V.; Subanna, G. N. *J. Am. Chem. Soc.* **2000**, *122*, 6237.
- [6] Neiner, D.; Golub, V.; Wiley, John B. *Materials Research Bulletin* **2004**, *39(10)*, 1385.
- [7] Zhu, W. J.; Feng, H. H.; Hor, P. H. *Materials Research Bulletin* **1996**, *31(1)*, 107.
- [8] A. Larson, R. B. Von Dreele, GSAS: Generalized Structure Analysis System, Los Alamos National Laboratory: Los Alamos NM, **1994**.
- [9] Le Bail, A.; Duroy and Fourquet, *Mater. Res. Bull.* **1988**, *23*, 447.
- [10] D. A. and J. A. Ibers, Modified POLSQ, Department of Chemistry, Northwestern University, Evanston, IL **1983**.
- [11] Blasse, G.; Van den Heuvel, G. P. M. *Journal of Solid State Chemistry* **1974**, *10(3)*, 206.
- [12] Tezuka, K., Hinatsu, Y., Masaki, N. M., Saeki, M., *J. Solid State Chem.* **1998**, *138*, 342.

Chapter 7

Concluding Remarks

The theme of the present dissertation was the use of topotactic techniques (divalent transition metal ion exchange and butyl lithium reductive intercalation) in the preparation of new compounds with interesting magnetic and electronic properties. The lesson we learned is that electron correlation effects and disorder govern the magnetic and electronic behavior of these compounds. Electron correlation effects lead to electron localization and therefore to insulating/semiconducting behavior, even if an empty d-band is easily accessible to filling via reductive intercalation. Disorder induced in these layered materials through a divalent ion exchange leads to unsatisfied magnetic interactions. This is the case for magnetic frustrated systems, which because of the impossibility of arranging the magnetic ions in a ferro or antiferromagnetic fashion; they prefer to go in a state where all of the magnetic interactions are equally unsatisfied. Overcoming these two undesired effects, correlation and disorder can be extremely challenging.

For example, in the second chapter we saw that disorder caused by both a solution reaction and by a 45% occupancy of vanadium site in $\text{Na}_{0.1}(\text{VO})_{0.45}\text{LaTiO}_4$ gives rise to paramagnetic properties. In the third chapter, the reductive intercalation of lithium in the triple layered RP produced a series of mixed valence titanates. The presence of an extra signal in the EPR data suggests that titanium from the perovskite blocks has been reduced upon intercalation. The magnetic properties of the new compounds depend on lithium content. At low lithium contents, these materials are Curie-Weiss paramagnets, while for

high lithium content ($x = 1.8$), magnetic order is observed. This dissertation described the structure, electronic and magnetic properties of this new series of compounds.

In the fourth chapter, a nickel layer has been inserted between the perovskite blocks of a triple layer Ruddlesden-Popper titanate, $\text{Li}_2\text{La}_2\text{Ti}_3\text{O}_{10}$. The magnetic data for $\text{Li}_{0.3}\text{Ni}_{0.85}\text{La}_2\text{Ti}_3\text{O}_{10}$ shows a Curie–Weiss behavior at high temperatures with a magnetic moment in agreement with the existence of a $\text{Ni}(\text{e}^4\text{t}_2^4)$ in a tetrahedral site. At 23 K, a ferromagnetic transition occurs. At lower temperatures (10 K), this system undergoes a reentrant spin glass transition. In terms of electronic behavior, $\text{Li}_{0.3}\text{Ni}_{0.85}\text{La}_2\text{Ti}_3\text{O}_{10}$ is an insulator. Then, a series of mixed valence Ruddlesden-Popper titanates have been prepared by reductive intercalation in $\text{Li}_{0.3}\text{Ni}_{0.85}\text{La}_2\text{Ti}_3\text{O}_{10}$. The magnetic properties of the new compounds depend on both lithium content and on the magnetic behavior of the parent, $\text{Li}_{0.3}\text{Ni}_{0.85}\text{La}_2\text{Ti}_3\text{O}_{10}$. With increasing lithium content, the interactions between neighboring nickel ions are less strong. At the same time, the ratio $\text{Ti}^{3+}/\text{Ti}^{4+}$ increases and their interactions become prevalent. Though in this case, $(\text{Li}_x\text{Ni})\text{La}_2\text{Ti}_3\text{O}_{10}$ is still a frustrated magnetic system.

In chapter six, $\text{Na}_{0.05}(\text{VO})_{0.48}\text{GdTiO}_4$ has been synthesized by an ion exchange reaction between the single-layered perovskite, NaGdTiO_4 , and VOSO_4 . Upon vanadyl insertion, empty sites are generated at the interlayer space. On these sites, lithium is intercalated by an $n\text{-BuLi}$ intercalation. The layered structure is preserved upon the intercalation step. The magnetic moment for $\text{Na}_{0.05}(\text{VO})_{0.48}\text{GdTiO}_4$ increases from $8.95 \mu_{\text{B}}$ to $10.69 \mu_{\text{B}}$ on lithium intercalation. The magnetic behavior seems to change from paramagnetic with a small antiferromagnetic component for $\text{Na}_{0.05}(\text{VO})_{0.48}\text{GdTiO}_4$ to a

magnetically ordered material characterized by frustration for



Also, band structure calculations, provided us with a better understanding of these materials. Band structures made it clear that whenever an ion exchange with an electron rich transition metal ion or unit occurs, the resulting product would have the electronic properties of the parent. This is because if one starts with the triple layered RP, $\text{Na}_2\text{La}_2\text{Ti}_3\text{O}_{10}$, which is an insulator with a direct band gap of approximately 5.4 eV, because of the non-magnetic insulating perovskite blocks, $[\text{La}_2\text{Ti}_3\text{O}_{10}]$, the ion exchange will produce a 2D magnetic insulating compound. If this compound is then intercalated with an alkali metal, the transition metal in the perovskite block will be partially reduced. The resulting compound would still be insulating/semiconductive depending on the crystal structure, bandwidth and the average oxidation state on the transition metal ion in the perovskite blocks. In this particular case, Ti is a 3d metal, and therefore has an already narrow band. Electrons in narrow bands tend to be localized on the individual atom due to electron correlation effects.

In the end, we have demonstrated the ability of these low temperature topotactic routes to prepare new compounds. The properties of these new materials have been examined and they can be categorized as diverse. One-step ahead, would be to investigate how these topotactic reactions occur.

Appendix 1

The insertion of a transition metal layer between the perovskite blocks

A.1.1 Introduction

The reactivity of the A' cations makes the Ruddlesden-Popper compounds, $A_2[A_{n-1}B_nO_{3n+1}]$, effective precursors to new low temperature phases via topochemical routes. One of the most effective topotactic routes is the replacement of the A' cations via an ion exchange reaction. These reactions can take place in either aqueous medium, molten state or solid state. Monovalent and divalent ions can be exchanged. Monovalent ion exchange has led to $Li_2La_2Ti_3O_{10}$ and the acidic form $H_2La_2Ti_3O_{10}$ in a molten state for the first and an acidic aqueous solution for the second.^[1,2] Divalent ion exchange $MLa_2Ti_3O_{10}$ with M= Co, Zn, Cu have been performed using an eutectic mixture of alkali metal chlorides and transition metal chlorides in a sealed tube.^[3]

This work constitutes an extension of such ion exchange reactions in the triple layered Ruddlesden-Popper series to obtain $Mn_{0.8}La_2Ti_3O_{10}$. This compound is obtained by a solid-state reaction. This paper describes the synthesis, the crystal structure, thermal behavior and magnetic and electronic properties of the new compound.

A.1.2 Experimental section

A.1.2.1 Synthesis

First, the $\text{Na}_2\text{La}_2\text{Ti}_3\text{O}_{10}$ prepared by a solid-state reaction from Na_2CO_3 (Alfa Aesar 99.99%), La_2O_3 (Alfa Aesar 99.99%) and TiO_2 (Alfa Aesar 99.99%). A 30% molar excess of Na_2CO_3 was used to compensate for the loss due to volatilization. The reagents were pressed into pellets, fired at 550 °C for 6 hours, and then sintered at 1050 °C for 12 hours. After the reaction, to remove unreacted Na_2CO_3 , the sample was washed with warm water and acetone and dried at 150 °C overnight.^[1] Phase purity for $\text{Na}_2\text{La}_2\text{Ti}_3\text{O}_{10}$ was confirmed by X-ray powder diffraction (XRD); the sample was indexed on the tetragonal unit cell $a = 3.8352(7)$ Å and $c = 28.5737(7)$, which is in agreement with the values reported in the literature.^[1] Then sodium was replaced with lithium by an ion exchange reaction between the $\text{Na}_2\text{La}_2\text{Ti}_3\text{O}_{10}$ and LiNO_3 , in a 1:15 molar ratio for two days at 300 °C.^[1] $\text{Mn}_{0.8}\text{La}_2\text{Ti}_3\text{O}_{10}$ was prepared in an evacuated tube. The reaction takes place from MnCl_2 and either $\text{Li}_2\text{La}_2\text{Ti}_3\text{O}_{10}$ or $\text{Na}_2\text{La}_2\text{Ti}_3\text{O}_{10}$. Initially, the reaction was performed at 390 °C for 7, 9, 12 and 14 days using a 1:2 molar ratio $\text{Li}_2\text{La}_2\text{Ti}_3\text{O}_{10}$ or $\text{Na}_2\text{La}_2\text{Ti}_3\text{O}_{10}$ to MnCl_2 . An unidentified impurity phase was always present. Other synthetic conditions were also tried. First, several other temperatures were employed. These were 300 °C, 325 °C, 340 °C, 350 °C and 425 °C. Also, different molar ratios 1:1, 1:3 were tried. Finally, an aqueous solution reaction at 50 °C using a 1:2 molar ratio was undertaken. The final product was washed with distilled water and acetone and dried at 100 °C overnight. $\text{Mn}_{0.8}\text{La}_2\text{Ti}_3\text{O}_{10}$ has a yellow color.

A.1.2.2 Characterization

Elemental analysis was carried out by energy dispersive spectroscopy (EDS) on a series of individual crystallites using a JEOL (model JSM-5410) scanning electron microscope (SEM) equipped with an EDAX (DX-PRIME) microanalytical system. X-ray powder diffraction studies were carried out on a Philips X'Pert System (Cu K α radiation $\lambda=1.5418$ Å) equipped with a graphite monochromator. Data were collected in a continuous scan mode between 5 and 95° 2 θ with a step size of 0.02. The lattice parameters were refined using POLSQ.^[4]

Thermal behavior was studied on a TGA 51 thermogravimetric analyzer and a Netzsch 404 S differential scanning calorimeter (DSC); measurements were performed in oxidizing and inert atmospheres between room temperature and 800 °C by heating samples at 10 °C/min in O₂ and Ar, respectively.

Magnetic measurements were performed on a Quantum Design MPMS-5S Superconducting Quantum Interference Device (SQUID) magnetometer between 2 and 300 K in 1000 Oe. Heat capacity, *ac* susceptibility and resistivity (two probe method) were measured using a PPMS Quantum Design between 5 K and 300 K.

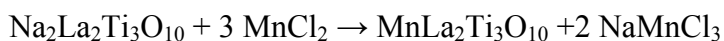
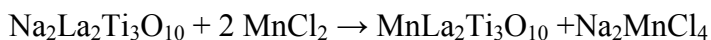
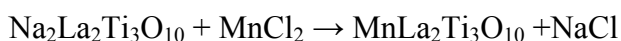
A.1.3 Results

A.1.3.1 Synthesis

The ability of Ruddlesden-Popper, A₂La₂Ti₃O₁₀ (A = Li, Na, K), to undergo ion exchange with manganese chloride has been investigated. Single phase Mn_{0.8}La₂Ti₃O₁₀ could not be obtained. The powder pattern for Na₂La₂Ti₃O₁₀, and Mn_{0.8}La₂Ti₃O₁₀

obtained at different temperatures are presented in Figure A.1.1. The reaction takes place in an evacuated sealed tube using pellets of $A_2La_2Ti_3O_{10}$ ($A = Li$ or Na). For a 1:2 molar ratio, $A_2La_2Ti_3O_{10}$ to $MnCl_2$, at 300 °C, the reaction does not occur after 7 days. For the same molar ratio and reaction time, at 325 °C, the reaction is not complete. For 390 °C and 425 °C, the impurity peaks appear more intense. The best reaction conditions were found to be a 1:2 and a temperature of 340 – 350 °C for 7 days. The impurity peaks have been reduced in these conditions. Even in this case, the ion exchange was not complete. The chemical analysis of the final product indicated the ratio Mn:La:Ti 0.80(1):2:3.00(2). Increasing the molar ratio, the temperature or the time length does not lead to any improvement in manganese content or impurity level. The product is yellow, though sometimes a green compound with the exact same composition and powder pattern is obtained. This is presumably related to a certain amount of Mn^{2+} that is oxidized to Mn^{3+} . Because not all of the peaks in the powder pattern could be indexed, we concluded that the sample contains a small amount of impurity (see Figure A.1.2).

The chemical reaction can be sometimes can be sometimes governed by the formation of certain byproducts. In this case, the possible reactions are:



Aqueous solution reaction (not shown) at 50 °C did not lead to the formation of the desired product; instead a brown precipitate manganese oxyhydroxide, $MnO(OH)$, was formed.

A.1.3.2 Structure

The ion exchange takes place in a topotactic manner. In Figure A.1.1 the XRD the powder patterns for the $\text{Na}_2\text{La}_2\text{Ti}_3\text{O}_{10}$ and $\text{Mn}_{0.8}\text{La}_2\text{Ti}_3\text{O}_{10}$ obtained using different synthetic conditions are presented. The product has been indexed on a tetragonal unit cell with the parameters listed in Table A.1.1.^[4] A simulated versus observed powder pattern for $\text{Mn}_{0.8}\text{La}_2\text{Ti}_3\text{O}_{10}$ is presented in Figure A.1.2.

A.1.3.3 Thermal behavior

In terms of thermal stability, DSC (Differential Scanning Calorimetry) for $\text{Mn}_{0.8}\text{La}_2\text{Ti}_3\text{O}_{10}$ in Ar shows that this compound is stable up to 900 °C. It decomposes above 1000 °C into a metallic material. In O_2 , this compound decomposes above 800 °C. The thermal behavior in both oxidizing and inert atmosphere is presented in Figure A.1.3. In addition, the XRD after DSC in O_2 is shown in Figure A.1.4. The decomposition products were found to be $\text{La}_2\text{Ti}_2\text{O}_7$ and MnTiO_3 .

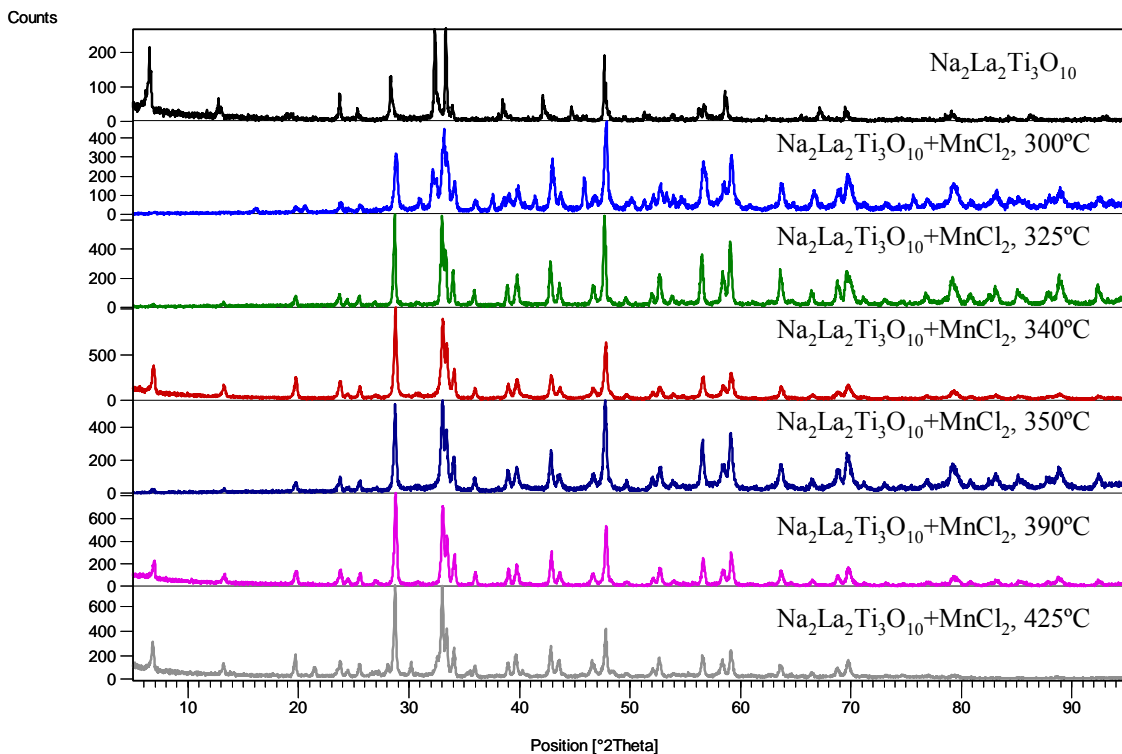


Figure A.1.1. Comparison of the X-ray powder patterns for different conditions used for the reaction $\text{Na}_2\text{La}_2\text{Ti}_3\text{O}_{10} + \text{MnCl}_2$ for a 1:2 molar ratio and 7 days.

Table A.1.1. The unit cells for $\text{Li}_2\text{La}_2\text{Ti}_3\text{O}_{10}$, $\text{Na}_2\text{La}_2\text{Ti}_3\text{O}_{10}$ and $\text{Mn}_{0.8}\text{La}_2\text{Ti}_3\text{O}_{10}$

Compound	a (Å)	c (Å)	Volume (Å ³)
$\text{Li}_2\text{La}_2\text{Ti}_3\text{O}_{10}$	3.8411(6)	26.5601(2)	391.8(6)
$\text{Na}_2\text{La}_2\text{Ti}_3\text{O}_{10}$	3.8352(1)	28.5737(3)	420.28(3)
$\text{Mn}_{0.8}\text{La}_2\text{Ti}_3\text{O}_{10}$	3.8137(1)	27.3296(2)	397.49(1)

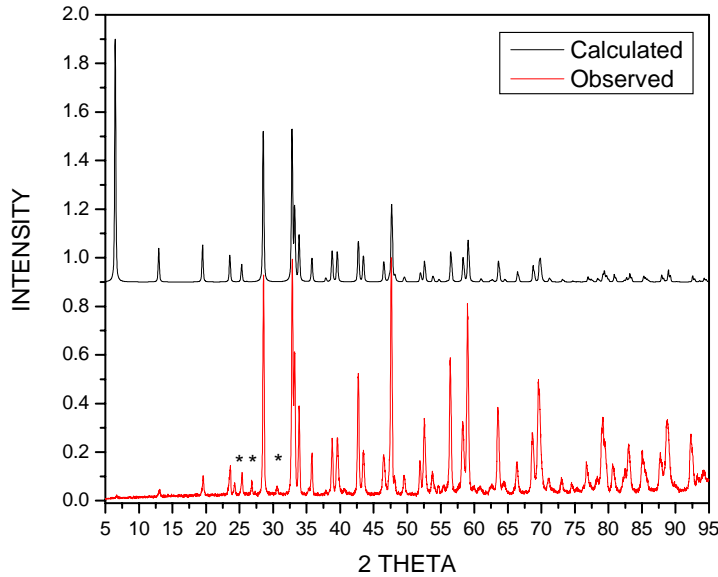


Figure A.1.2. Calculated (top) versus observed (bottom) powder patterns for $\text{Mn}_{0.8}\text{La}_2\text{Ti}_3\text{O}_{10}$. The stars evidence the unindexed peaks.

A.1.3.4 Band structure calculations and transport measurements

Transport measurements on $\text{Mn}_{0.8}\text{La}_2\text{Ti}_3\text{O}_{10}$ are consistent with an insulator (resistivity greater than $1 \text{ G}\Omega$). The changes that manganese insertion causes in $\text{Na}_2\text{La}_2\text{Ti}_3\text{O}_{10}$ have been also followed by extended Hückel calculations performed using the YAEHMOP software package.^[16] The band structures along with the density of states (DOS) are presented in Figure A.1.5. The Fermi level is at -10.9415 eV . The states below the Fermi level are Ti s, d states and O s, p states. The bands a little below and at the Fermi level are bonding and non-bonding combinations of Mn s, d with O s, p. The high-energy states around -6 eV , that correspond to La, remain unoccupied.

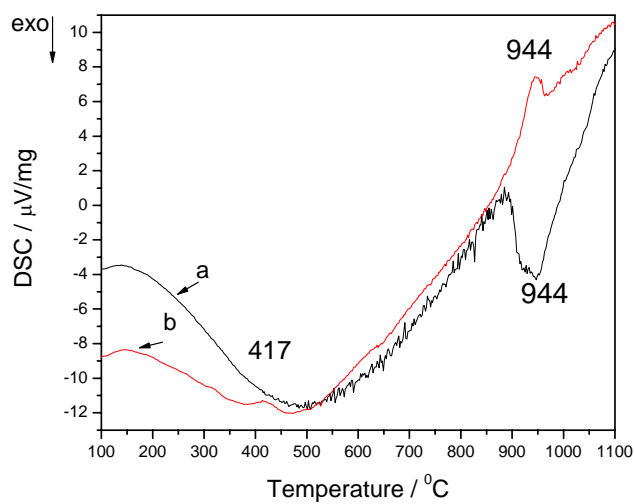


Figure A.1.3. DSC curves in a) argon and b) oxygen for $\text{Mn}_{0.8}\text{La}_2\text{Ti}_3\text{O}_{10}$.

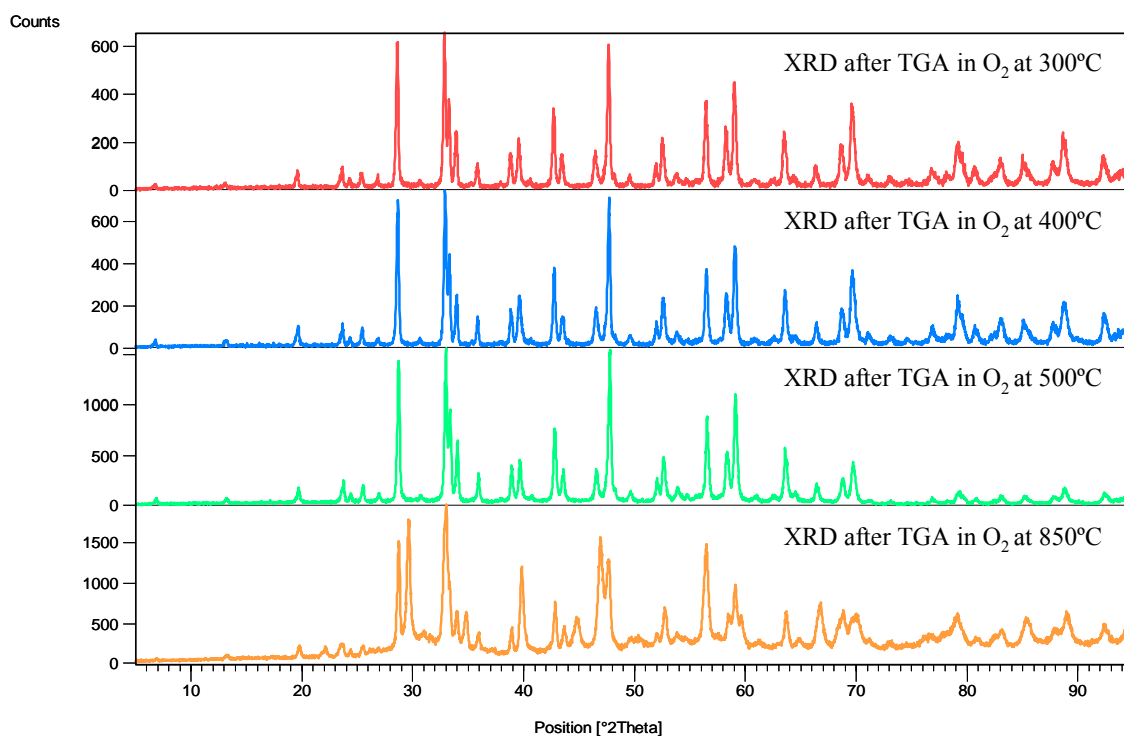


Figure A.1.4. X-ray powder patterns for $\text{Mn}_{0.8}\text{La}_2\text{Ti}_3\text{O}_{10}$ after TGA in O_2 .

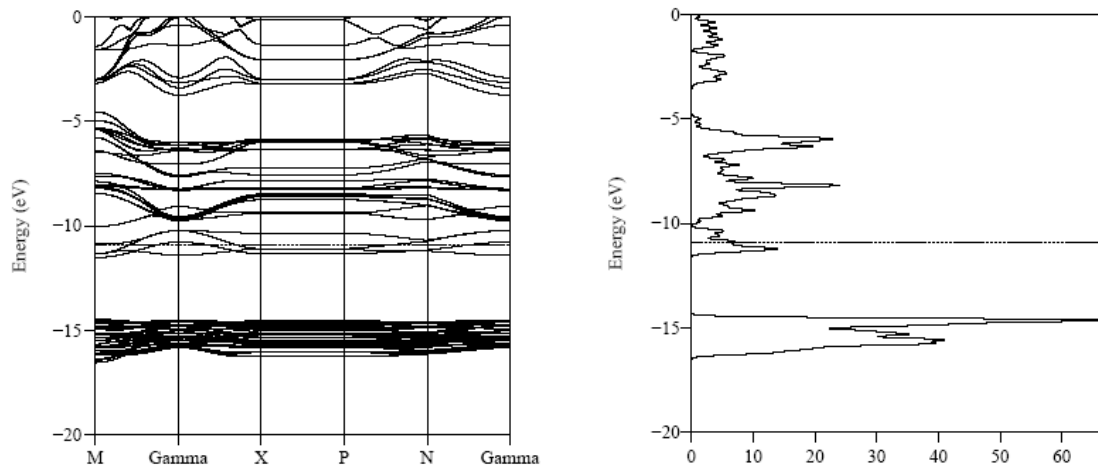


Figure A.1.5. The band structures and the DOS for $\text{Mn}_{0.8}\text{La}_2\text{Ti}_3\text{O}_{10}$.

A.1.3.5 Magnetic behavior and heat capacity

The magnetic susceptibility (ZFC/FC data) in a 1000 Oe field are presented in Figure A.1.6. From the linear fit of the reciprocal susceptibility versus temperature, a magnetic moment of $6.15 \mu_B$ and a Weiss constant of -196 K were obtained. The magnetic moment is higher than expected for a Mn^{2+} spin only system. At low temperatures, the ZFC/FC curves split. Also, at 2 K there is a small hysteresis loop, presented in Figure A.1.7. The heat capacity of $\text{Mn}_{0.8}\text{La}_2\text{Ti}_3\text{O}_{10}$ is presented in Figure A.1.8. There is no transition to long range order in the specific heat measurement, so most likely $\text{Mn}_{0.8}\text{La}_2\text{Ti}_3\text{O}_{10}$ is an amorphous magnetic system characterized by disorder and maybe frustration in the magnetic interactions. Though there is no transition to long range order in the specific heat, the entropy levels off at ~ 15 J/ mole, which corresponds to a $S = R \ln(2S+1) = 14.88$ J/mole, for an $S = 5$ system. This can be seen from Figure A.1.9.

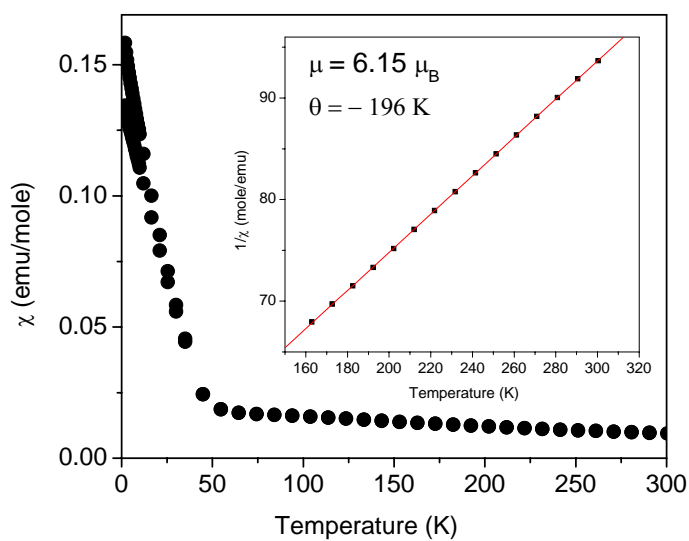


Figure A.1.6. The temperature dependence of the molar susceptibility for $\text{Mn}_{0.8}\text{La}_2\text{Ti}_3\text{O}_{10}$.

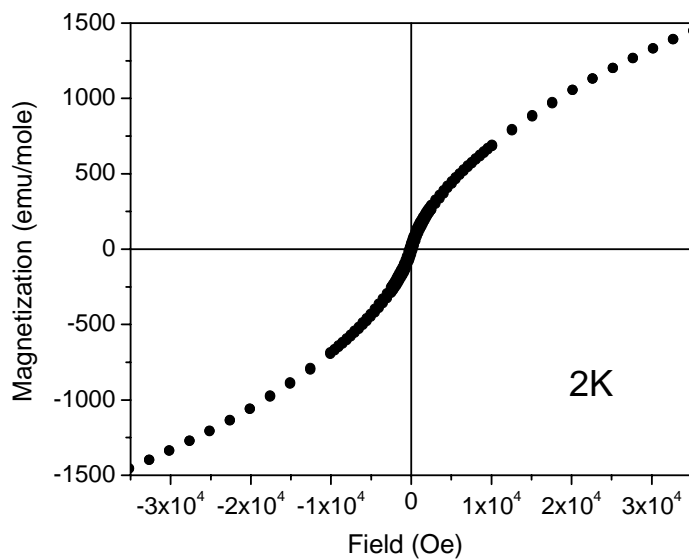


Figure A.1.7. Hysteresis loop at 2 K for $\text{Mn}_{0.8}\text{La}_2\text{Ti}_3\text{O}_{10}$.

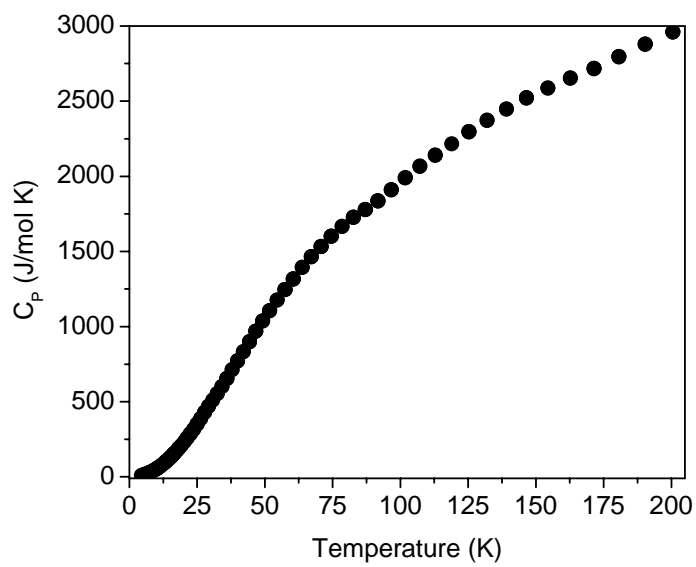


Figure A.1.8. Heat capacity for $\text{Mn}_{0.8}\text{La}_2\text{Ti}_3\text{O}_{10}$.

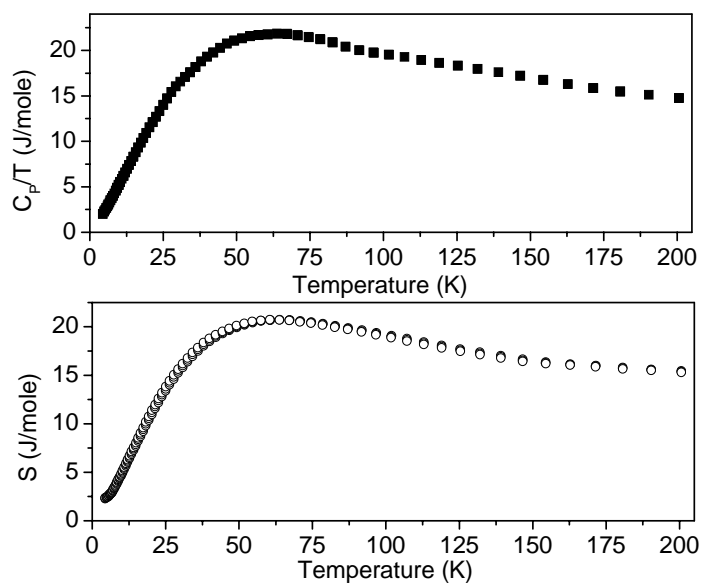


Figure A.1.9. Heat capacity and entropy variation as a function of temperature for $\text{Mn}_{0.8}\text{La}_2\text{Ti}_3\text{O}_{10}$.

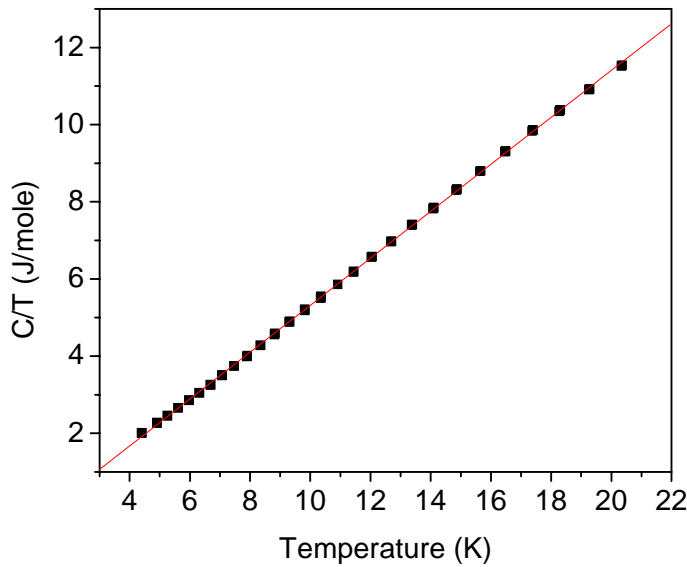


Figure A.1.10. Heat capacity as a function of temperature for $\text{Mn}_{0.8}\text{La}_2\text{Ti}_3\text{O}_{10}$ showing a linear behavior for the C/T .

Also, as presented in Figure A.1.10, there is a linear behavior for the C/T versus T , at low temperatures. This signals the presence of a spin glass behavior.

The ac susceptibility measurements revealed only one peak, very broad at 39 K in the real and a very weak signal in the imaginary part (not shown). This peak corresponds to the ZFC/FC split seen in the *dc* measurements. The real part *ac* susceptibility is presented in Figure A.1.11. The signal does not seem to vary with applied *ac* frequency; here are represented only two frequencies, 1000 and 2000 Hz. Also, there is no signal in the imaginary part. This seems to agree with an antiferromagnetic arrangement of spins.

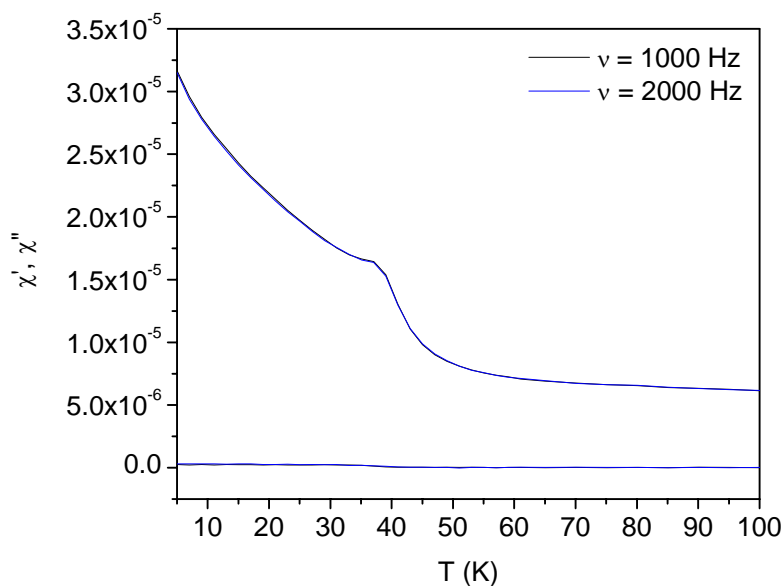


Figure A.1.11. The real and imaginary part of the ac susceptibility for $\text{Mn}_{0.8}\text{La}_2\text{Ti}_3\text{O}_{10}$.

A.1.4 Discussion

The ion exchange that replaces the alkali metal layer in $\text{A}_2\text{La}_2\text{Ti}_3\text{O}_{10}$ (where A = Li or Na) with Mn^{2+} ions takes place in a topotactic manner. The unit cell for $\text{Mn}_{0.8}\text{La}_2\text{Ti}_3\text{O}_{10}$ is similar in size with $\text{CoLa}_2\text{Ti}_3\text{O}_{10}$.^[3] Manganese occupies a tetrahedral site between the perovskite sheets. Thermal behavior of $\text{Mn}_{0.8}\text{La}_2\text{Ti}_3\text{O}_{10}$ indicates that the layered structure is maintained up to 900 °C in inert atmosphere. In oxidizing conditions, probably the facile oxidation of Mn^{2+} to Mn^{3+} , favors the formation of a more thermodynamically stable phase, LaMnO_3 , above 800 °C.

The compound is an insulator. The band structure calculations performed in this study are not consistent with an insulating type of behavior. There are two possible reasons for our calculations to fail explaining the observed resistivity data. One could be

that the program we use to approximate the electronic properties, does not account for electronic repulsions effects.

This material has unique magnetic properties. The magnetic moment calculated based on the linear fit of $1/\chi$ versus T is higher than expected for a Mn^{2+} system. The calculated magnetic moment is $6.15 \mu_B$, while the expected value based on both spin only and with a non-quenched angular momentum, is $5.92 \mu_B$.^[5] Also, the observed values for d^5 ions in the iron series ran from $5.8 \mu_B$ to $6.00 \mu_B$.^[5] It could be that the impurity we see in the XRD data (unindexed peaks in Figure A.1.2) is magnetic. Though this can be the case, the possibility that this is an intrinsic property of $\text{Mn}_{0.8}\text{La}_2\text{Ti}_3\text{O}_{10}$ cannot be ruled out. The Weiss constant, $\theta = -196 \text{ K}$, indicates strong antiferromagnetic interactions. Although, the Weiss constant indicates antiferromagnetic interactions, no transition to a long range order has been seen in the specific heat measurement. Moreover, the shape of the C/T and entropy versus temperature suggest short range order interactions.^[6] These can be due to zero field splitting effects or single ion anisotropy. Also, $\text{MnLa}_2\text{Ti}_3\text{O}_{10}$ could be a 2D system, and therefore the shape of the C/T and S is as expected. Interestingly, the entropy increases with increasing temperature, and it levels off to a value that is approximately what one might expect for an spin $S = 5$, using $S = R\ln(2S+1) = 14.88 \text{ J/mole}$. This can be seen from Figure A.1.8. Another indication of short range order is the linearity of the C/T versus T for $4 - 20 \text{ K}$. This is known to be a characteristic of spin glasses, which are nothing but short range ordered systems. In the real part of the ac susceptibility measurement, there is only one broad transition at 39 K . At this temperature, the two curves, ZFC/FC, split. In addition, this transition does not seem to be frequency dependent. This rule out the possibility of either a spin glass or a

ferromagnet since these would be frequency dependent. Therefore, at this point, this transition could be classified as antiferromagnetic caused by short range interaction, though a true long range order is not established.

A.1.5 References

- [1] Toda, K.; Watanabe, J.; Sato, M., *Mat. Res. Bull.* **1996**, *31*, 1427.
- [2] Gopalakrishnan, J.; Uma, S.; Bhat, V.; *Chem. Mater.* **1993**, *5*, 132.
- [3] Hyeon, Ki-An and Byeon, Song-Ho *Chem. Mater.* **1999**, *11*, 352.
- [4] D. A. and J. A. Ibers, Modified POLSQ, Department of Chemistry, Northwestern University, Evanston, IL **1983**.
- [5] Carlin, R. L. *Magnetochemistry*, Springer-Verlag Berlin Heidelberg, **1986**.

Appendix 2

Vanadyl insertion in the double and triple layered RP

A.2.1 Introduction

Layered perovskites of the Dion-Jacobson (DJ), $A'[A_{m-1}B_mO_{3m+1}]$, and Ruddlesden-Popper (RP), $A'_2[A_{m-1}B_mO_{3m+1}]$, families, where A' = alkali or alkali earth metal, A = rare earth or alkaline metal, B = transition metal, m goes from 1 to infinity and contain perovskite strata interleaved with A' ion-exchangeable cations. The reactivity of the A' cations make these compounds effective precursors to new low temperature phases via topochemical routes. In the case of the double layer RP, ion exchange lead to the formation of the hydrogen form, $H_2SrTa_2O_7$.^[1] This could be topochemically condensed in a three dimensional perovskite structure, $Sr_{0.5}TaO_3$.^[2] Gopalakrishnan and coworkers investigated the triple-layered perovskite, $K_2La_2Ti_3O_{10}$ and reported initial studies on the ion exchange of vanadyl species.^[3] Also, we reported an ion exchange route via a solution reaction in $NaLaTiO_4$ to produce $Na_{0.1}(VO)_{0.45}LaTiO_4$.^[4] Herein we expand on this approach with a detailed study on the synthesis of $(VO)Gd_2Ti_2MnO_{10}$ and $(VO)SrTa_2O_7$. The instability of these compounds in acidic conditions prevented the formation of $(VO)Gd_2Ti_2MnO_{10}$ and $(VO)SrTa_2O_7$.

A.2.2 Experimental

A.2.2.1. Synthesis

The double layered RP compound, $\text{K}_2\text{SrTa}_2\text{O}_7$ was prepared by a solid state reaction from K_2CO_3 and SrCO_3 and Ta_2O_5 mixed in stoichiometric amounts. The mixture of the three solids was first fired at 850 °C for 6 hours and then at 1050 °C for 6 hours.^[5] Then the final product was cooled naturally at 200 °C. The triple layered RP perovskite, $\text{Na}_2\text{Gd}_2\text{Ti}_2\text{MnO}_{10}$, was prepared from Na_2CO_3 , Gd_2O_3 , TiO_2 and MnO_2 mixed in stoichiometric amounts and fired at 1100 °C.^[6] The reaction takes place in 12-14 hours with intermediate grindings every 30 minutes. All of the final products were washed with warm water, rinsed with acetone and dried at 150 °C overnight. Phase purity for $\text{K}_2\text{SrTa}_2\text{O}_7$ and $\text{Na}_2\text{Gd}_2\text{Ti}_2\text{MnO}_{10}$ was confirmed by X-ray powder diffraction (XRD). $\text{K}_2\text{SrTa}_2\text{O}_7$ was indexed in a tetragonal cell with $a = 3.8588(1)$ and $c = 22.0008(2)$. $\text{Na}_2\text{Gd}_2\text{Ti}_2\text{MnO}_{10}$ was indexed in a tetragonal cell with $a = 7.4202(1)$ and $c = 27.8479(2)$. These values are in agreement with the values reported in the literature for these compounds.^[5,6]

Ion exchange was used to substitute the Na and K ions in the double and the triple layered RP with vanadyl ions, $(\text{VO})^{2+}$. The source of the vanadyl unit was vanadyl sulfate hydrate ($\text{VOSO}_4 \cdot n\text{H}_2\text{O}$, Alfa Aesar, 99.99%). Different synthetic conditions have been used to form $(\text{VO})\text{SrTa}_2\text{O}_7$ and $(\text{VO})\text{Gd}_2\text{Ti}_2\text{MnO}_{10}$ including various molar ratio and reaction medium, temperatures and reaction time.

A.2.2.2. Characterization

Energy dispersive spectroscopy (EDS) was carried out on a JEOL (model JSM-5410) scanning electron microscope (SEM) equipped with an EDAX (DX-PRIME) microanalytical system.

X-ray powder diffraction studies were carried out on a Phillips X'Pert System (Cu K α radiation $\lambda=1.5418 \text{ \AA}$) equipped with a graphite monochromator. Data were collected in a step scan mode between 2 and 95° 2 θ with a step size of 0.02° and a counting time of 10 s. The unit cells for the studied compounds were found by indexing their powder pattern using POLSQ.^[7]

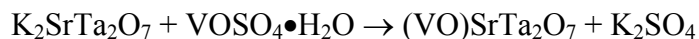
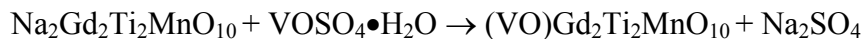
Infrared spectroscopy (IR) was performed on a Perkin Elmer 2000 FT-IR; the samples were analyzed as pellets in a 1:100 molar ratio with dry KBr.

Thermal behavior was studied on a Netzsch 404 S differential scanning calorimeter (DSC); measurements were performed in inert atmospheres between room temperature and 800 °C by heating samples at 10 °C/min in Ar.

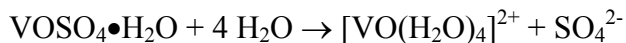
A.2.3 Results

A.2.3.1. Synthesis

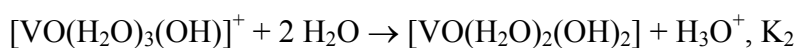
The ion exchange reaction was carried out to replace Na⁺ and respectively K⁺ ions with the (VO)²⁺ ion in Na₂Gd₂Ti₂MnO₁₀ and K₂SrTa₂O₇ to obtain (VO)Gd₂Ti₂MnO₁₀ and (VO)SrTa₂O₇.



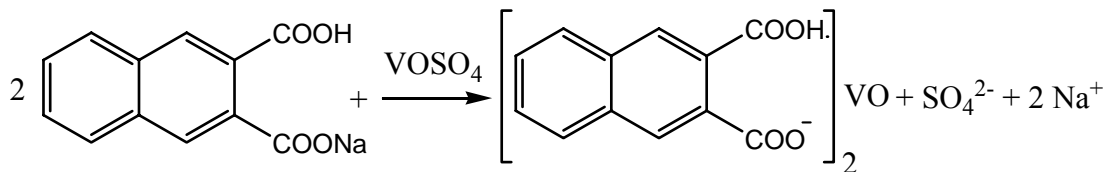
The reaction between vanadyl sulfate and $\text{Na}_2\text{Gd}_2\text{Ti}_2\text{MnO}_{10}$ was carried out in aqueous solution, typically 100 ml water, using 1.5 mmoles of reactant for 1 mol of the starting material, at 100 °C under reflux. The reaction is considered to be complete after 5 days. A color change from the black, $\text{Na}_2\text{Gd}_2\text{Ti}_2\text{MnO}_{10}$, to green, $(\text{VO})\text{Gd}_2\text{Ti}_2\text{MnO}_{10}$, is observed; green being the characteristic color for the vanadyl salts. The XRD pattern of the starting material and of the ion exchanged product along with elemental analysis reveal that, $(\text{VO})\text{Gd}_2\text{Ti}_2\text{MnO}_{10}$ forms (Table A.2.3, Figure A.2.4). Unfortunately, an unidentified impurity is always present. Moreover, EDAX (Table A.2.4) showed that the amount of Mn decreases upon ion exchange. This fact was also confirmed by ICP on the ion exchange solution, after the completion of the reaction, when Mn was found (56.251 mg/l). It is known that the vanadyl cation is acidic in aqueous solution, in the conditions of this reaction a pH = 2.4 was found. The reaction is pH sensitive so to increase the pH, but still have vanadyl cations in solution (vanadyl cation is stable in solution up to pH around 5), a standard buffer that insures a pH = 5 was used instead of water. The pH of the vanadyl sulfate solution when dissolved in sodium phthalate (buffer) increases to 4.5. The problem this time comes from the fact that the ion exchange is not taking place at the same extent as it did in the aqueous solution. This is shown in Table A.2.4 in which EDAX data from three samples, two in water and one in buffer are presented and for comparison EDAX for the parent is presented. In water vanadyl sulfate hydrates:



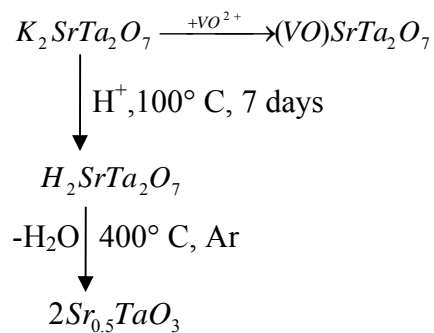
In addition, hydrolysis, and therefore the solution become acidic:



In buffer, the situation is different:



In the case of $\text{K}_2\text{SrTa}_2\text{O}_7$, there are two reasons for the ion exchange not to lead to $(\text{VO})\text{SrTa}_2\text{O}_7$, one is the competitive reaction to form $\text{H}_2\text{SrTa}_2\text{O}_7$ and the other is the instability of $\text{K}_2\text{SrTa}_2\text{O}_7$ in an acidic medium. $\text{K}_2\text{SrTa}_2\text{O}_7$ is not stable under a pH of 6. This is outlined in the scheme below.



A.2.3.2. Structure.

Ion exchange takes place in a topotactic manner in that the structure of the perovskite host is maintained. Figure A.2.1 presents the crystal structures of the two hosts compounds. Figure A.2.2 shows a comparison of the X-ray powder diffraction patterns before and after exchange for the single layered RP perovskite. Table A.2.1 shows the variation in unit cell parameters and cell volume. For the double-layered RP, a comparison of the XRD powder patterns before and after the ion exchange reaction is presented in Figure A.2.4. A unit cell for this compound was not obtained due to its poor

crystallinity. In the case of the triple layered RP, $\text{Na}_2\text{Gd}_2\text{Ti}_2\text{MnO}_{10}$, the powder pattern for the parent and ion-exchanged product are represented in Figure A.2.4. The refined cell parameters are in Table A.2.3. The compound forms, but there is a small amount of Mn-containing impurity. Also, elemental analysis shows (Table A.2.3) that there is a loss of manganese accompanying the ion exchange reaction when the reaction is performed in water. Also as seen from Table A.2.4, when the reaction is in buffer, this consumes the vanadyl cation, so the exchange rate decreases dramatically.

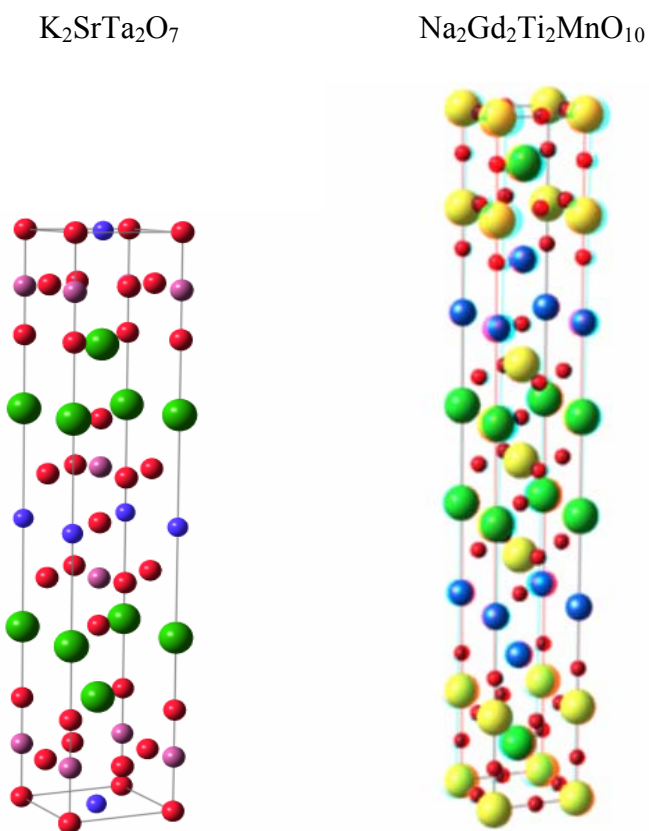


Figure A.2.1. The double and triple layered RP used in this study.

Table A.2.1. Refined unit cell parameters for $\text{Na}_2\text{Gd}_2\text{Ti}_2\text{MnO}_{10}$ and $(\text{VO})\text{Gd}_2\text{Ti}_2\text{MnO}_{10}$

Compounds	Unit cell parameters		Cell volume
	a (Å)	c (Å)	V (Å ³)
$\text{Na}_2\text{Gd}_2\text{Ti}_2\text{MnO}_{10}$ this work	7.4202(1)	27.8479(2)	1533.28
$(\text{VO})\text{Gd}_2\text{Ti}_2\text{MnO}_{10}$	7.4909(4)	25.4383(2)	1427.43

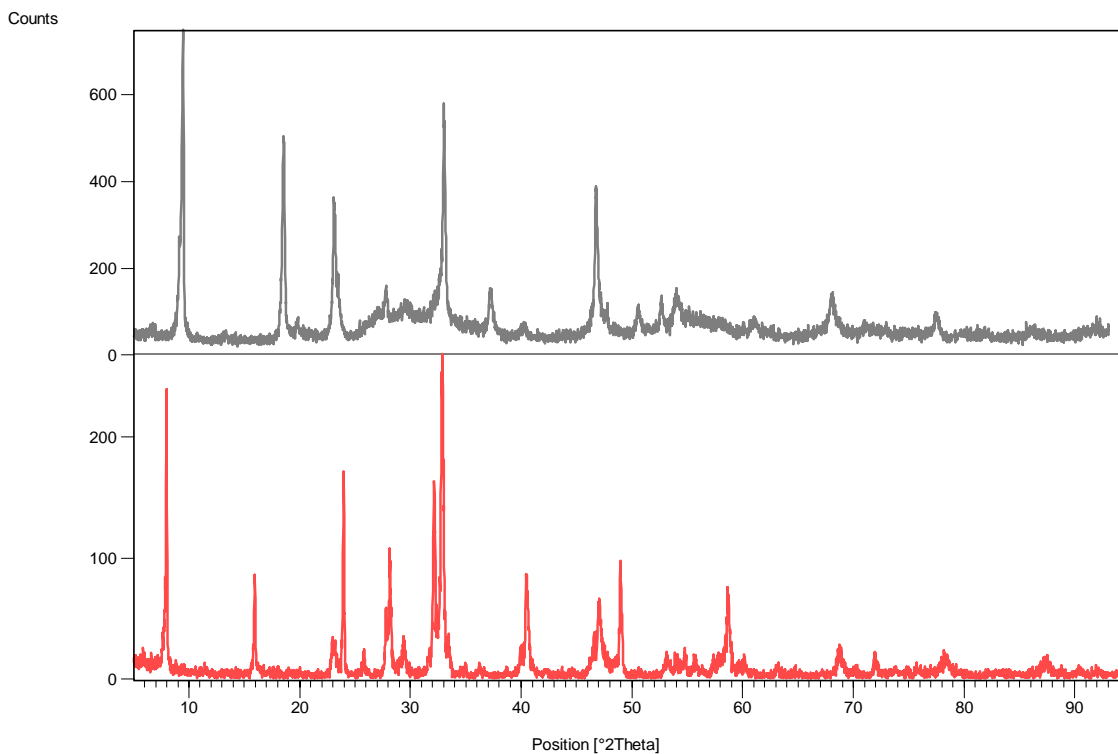


Figure A.2.2 XRD powder patterns for $\text{K}_2\text{SrTa}_2\text{O}_7$ (bottom) and $(\text{VO})\text{SrTa}_2\text{O}_7$ (top).

A.2.4.3. IR data

The presence of the VO unit in the structure is supported by the IR spectra, which show the characteristic stretching band at around 1012 cm^{-1} . A comparable value was observed in the triple layered RP, $(\text{VO})\text{La}_2\text{Ti}_3\text{O}_{10}$ and for $\text{Na}_{0.1}(\text{VO})_{0.45}\text{LaTiO}_4$.^[3, 4]

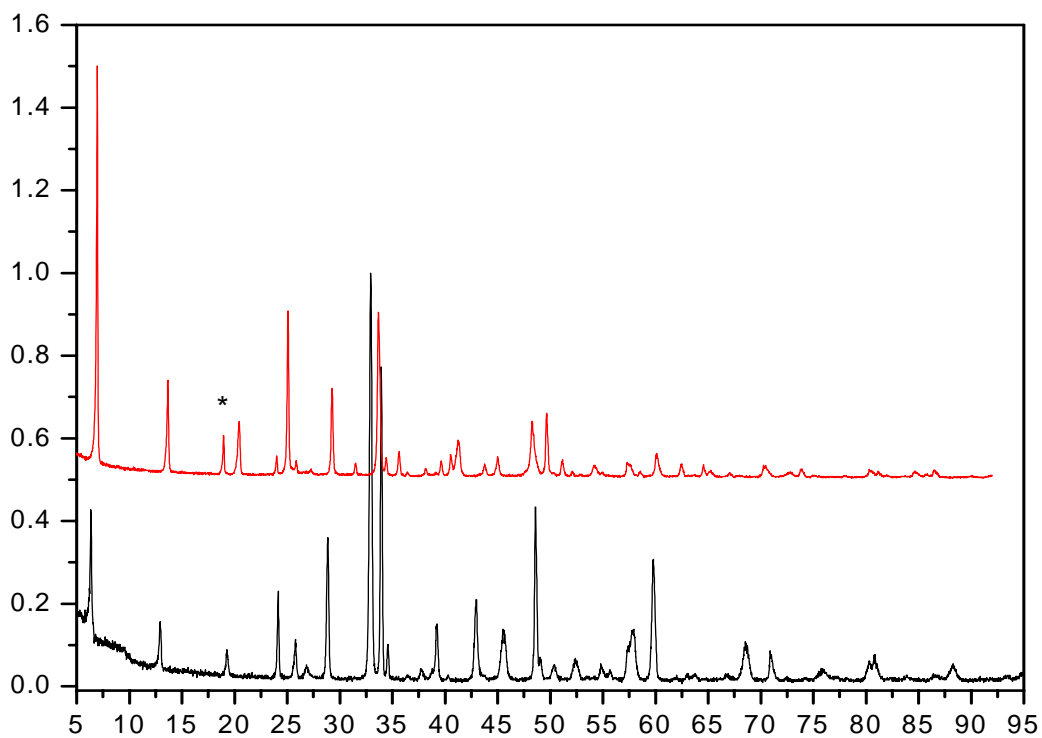


Figure A.2.3. XRD patterns for $\text{Na}_2\text{Gd}_2\text{Ti}_2\text{MnO}_{10}$ (bottom) and $(\text{VO})\text{Gd}_2\text{Ti}_2\text{MnO}_{10}$ (top).

Table A.2.2. EDAX for the ion exchange reaction between $\text{Na}_2\text{Gd}_2\text{Ti}_2\text{MnO}_{10}$ and VOSO_4 .

Sample type	EDAX results in Na:Gd:Ti:Mn:V ratio
$\text{Na}_2\text{Gd}_2\text{Ti}_2\text{MnO}_{10} + \text{VOSO}_4$ in buffer	0.44:2.33:2:0.75:0.2
$\text{Na}_2\text{Gd}_2\text{Ti}_2\text{MnO}_{10} + \text{VOSO}_4$ in water I	0.17:2:1.7:0.45:1.35
$\text{Na}_2\text{Gd}_2\text{Ti}_2\text{MnO}_{10} + \text{VOSO}_4$ in water II	0.23:2:1.8:0.52:0.97
$\text{Na}_2\text{Gd}_2\text{Ti}_2\text{MnO}_{10}$	2:1:1.6:1:0

A.2.4 Discussion

The ion exchange reaction leads to the vanadyl insertion only for the single layered RP compound. The reaction is prevented to occur in the double layered RP, $\text{K}_2\text{SrTa}_2\text{O}_7$, due to the competition between the H^+ and VO^{2+} moiety mobilities in solution. Another factor that precluded the formation of $(\text{VO})\text{SrTa}_2\text{O}_7$ is the instability of $\text{K}_2\text{SrTa}_2\text{O}_7$ under a pH of 6. The XRD on the final product showed that the layered structure has been maintained. XRD after TGA in Ar shows that the decomposition

product is the defective perovskite phase $\text{Sr}_{0.5}\text{TaO}_3$. This compound is obtained by a condensation reaction from $\text{H}_2\text{SrTa}_2\text{O}_7$.

In the case of the triple layered RP, $\text{Na}_2\text{Gd}_2\text{Ti}_2\text{MnO}_{10}$, a loss of the manganese ions from the perovskite blocks occurs upon ion exchange. This means that the acidity of the vanadyl sulfate solution attacks and partially destroys the perovskite blocks. When the reaction is performed in buffer, apparently, the buffer binds the vanadyl unit and therefore the ion exchange does not occur.

A.2.7 References

- [1] Bhuvanesh, N.; S. P.; Crosnier-Lopez, M.P.; Duroy, H.; Fourquet, J. L. *Journal of Materials Chemistry* **2000** 10(7), 1685.
- [2] Ollivier, Patricia J.; Mallouk, Thomas E. *Chemistry of Materials* **1998** 10(10), 2585.
- [3] Gopalakrishnan, J.; Sivakumar, T.; Ramesha, K.; Thangadurai, V.; Subanna, G. N. *J. Am. Chem. Soc.* **2000** 122, 6237.
- [4] Neiner, D.; Golub, V.; Wiley, John B. *Mat. Res. Bull.* **2004** 39(10), 1385.
- [5] Kodenkandath, T. A.; Wiley, J. B. *Mat. Res. Bull.* **2000** 35(10), 1737.
- [6] Schaak, R.E.; Afzal, D.; Schottenfeld, J.; Mallouk, Thomas E. *Chemistry of Materials* **2002**, 14(1), 442.
- [7] D. A. and J. A. Ibers, Modified POLSQ, Department of Chemistry, Northwestern University, Evanston, IL **1983**.

Appendix 3

The insertion of a transition metal layer between the perovskite blocks

A.3.1 Introduction

The reactivity of the A' cations makes the Ruddlesden-Popper compounds, $A_2[A_{n-1}B_nO_{3n+1}]$, effective precursors to new low temperature phases via topochemical routes. One of the most effective topotactic routes is the replacement of the A' cations via an ion exchange reaction. The assembly of a transition metal halide layer between the perovskite sheets has been proved only for the Dion-Jacobson series.^[1] This work constitutes an extension of such ion exchange reactions in the triple layered Ruddlesden-Popper series to obtain $(FeCl)La_2Ti_3O_{10}$. Herein, we describe the synthesis, the crystal structure and magnetic properties of the new compound.

A.3.2 Experimental section

A.3.2.1 Synthesis

First, the $Na_2La_2Ti_3O_{10}$ prepared by a solid state reaction from Na_2CO_3 (Alfa Aesar 99.99%), La_2O_3 (Alfa Aesar 99.99%) and TiO_2 (Alfa Aesar 99.99%).^[2] A 30% molar excess of Na_2CO_3 was used to compensate for the loss due to volatilization. The reagents were pressed into pellets, fired at 550 °C for 6 hours, and then sintered at 1050 °C for 12 hours. After the reaction, to remove unreacted Na_2CO_3 , the sample was washed with warm water and acetone and dried at 150 °C overnight. Phase purity for

$\text{Na}_2\text{La}_2\text{Ti}_3\text{O}_{10}$ was confirmed by X-ray powder diffraction (XRD); the sample was indexed on the tetragonal unit cell $a = 3.8352(7) \text{ \AA}$ and $c = 28.5737(7)$, which is in agreement with the values reported in the literature.^[2] Then sodium replaced with lithium by an ion exchange reaction between the $\text{Na}_2\text{La}_2\text{Ti}_3\text{O}_{10}$ and LiNO_3 , in a 1:15 molar ratio for two days at 300°C . The attempt to prepare $(\text{FeCl})\text{La}_2\text{Ti}_3\text{O}_{10}$ used a sealed tube reaction. This takes place from either $\text{Li}_2\text{La}_2\text{Ti}_3\text{O}_{10}$ or $\text{Na}_2\text{La}_2\text{Ti}_3\text{O}_{10}$ and FeCl_3 pelletized, in 1:2 molar ratio and a temperature of 250°C for 7 days. The final product was washed with distilled water and acetone and dried at 100°C overnight. $\text{Fe}_{0.62}\text{La}_2\text{Ti}_3\text{O}_{10}$ has a dark brown color.

A.3.2.2 Characterization

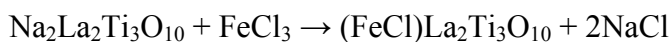
Elemental analysis was carried out by energy dispersive spectroscopy (EDS) on a series of individual crystallites using a JEOL (model JSM-5410) scanning electron microscope (SEM) equipped with an EDAX (DX-PRIME) microanalytical system. X-ray powder diffraction studies were carried out on a Philips X'Pert System ($\text{Cu K}\alpha$ radiation $\lambda = 1.5418 \text{ \AA}$) equipped with a graphite monochromator. Data were collected in a continuous scan mode between 5 and $95^\circ 2\theta$ with a step size of 0.02 .

Magnetic measurements were performed on a Quantum Design MPMS-5S Superconducting Quantum Interference Device (SQUID) magnetometer between 2 and 300 K at 100 Oe .

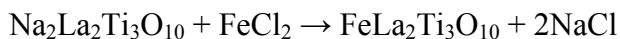
A.3.3 Results

A.3.3.1 Synthesis

The ability of Ruddlesden-Popper, $A_2La_2Ti_3O_{10}$ ($A = Li, Na, K$), to undergo ion exchange with iron (III) chloride has been investigated. Chemical analysis, EDAX indicated a ratio Fe:La:Ti 0.620(1):2:3.004(2). In addition, no chlorine was found in the sample. The expected reaction was:



The route the reaction went was:



A.3.3.2 Structure

The ion exchange takes place in a topotactic manner. In Figure A.3.1 the XRD powder patterns for the $Na_2La_2Ti_3O_{10}$ and $Fe_{0.62}La_2Ti_3O_{10}$ are presented. The ion-exchanged material was refined on tetragonal Bravais lattice with the cell parameters listed in Table A.3.1. Figure A.3.2 shows a calculated versus observed powder pattern for $Fe_{0.62}La_2Ti_3O_{10}$.

Table A.3.1. The variation of the unit cell parameters and volume for all of the investigated materials

Compound	a (Å)	c (Å)	Volume (Å ³)
Li ₂ La ₂ Ti ₃ O ₁₀	3.8411(6)	26.5601(2)	391.8(6)
Na ₂ La ₂ Ti ₃ O ₁₀	3.8352(1)	28.5737(3)	420.28(3)
Fe _{0.62} La ₂ Ti ₃ O ₁₀	3.8067(1)	27.2126(2)	394.33(1)

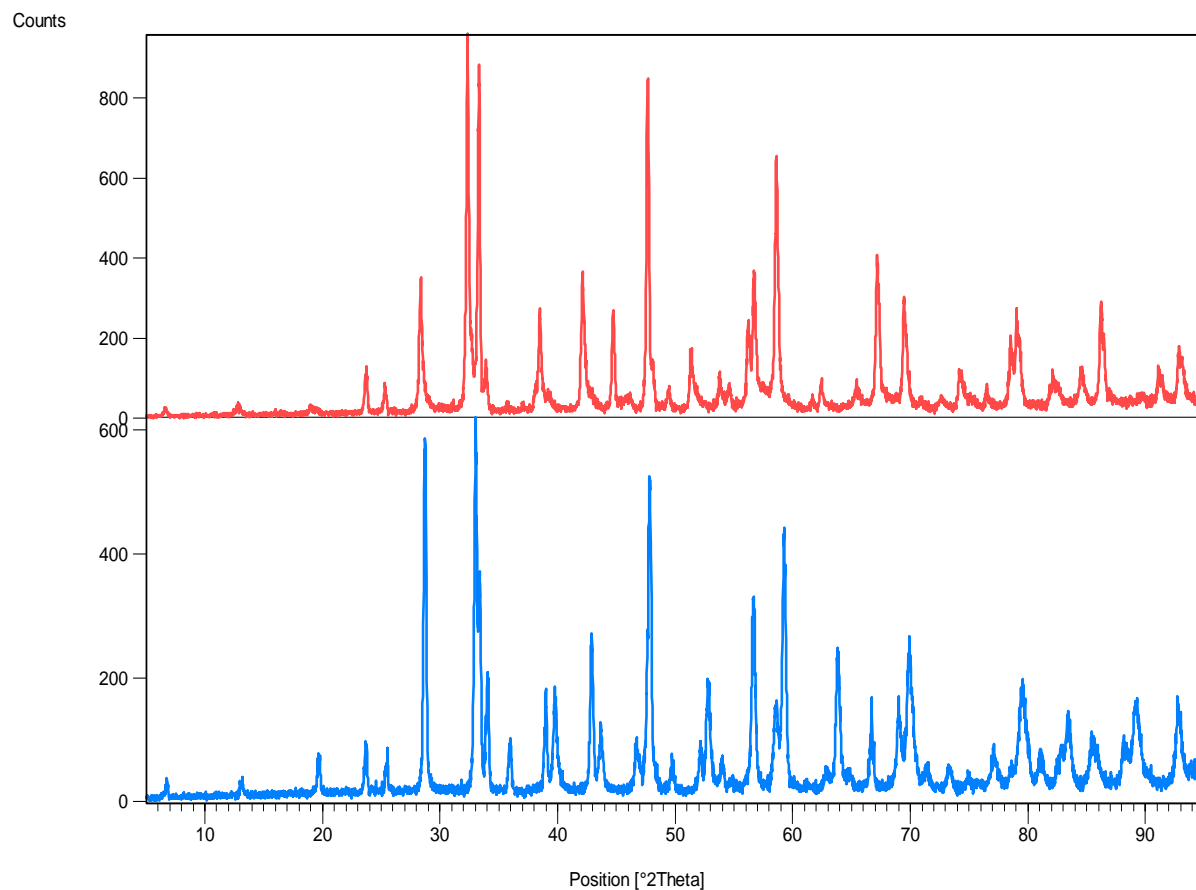


Figure A.3.1. X-ray powder patterns for Na₂La₂Ti₃O₁₀ and Fe_{0.62}La₂Ti₃O₁₀

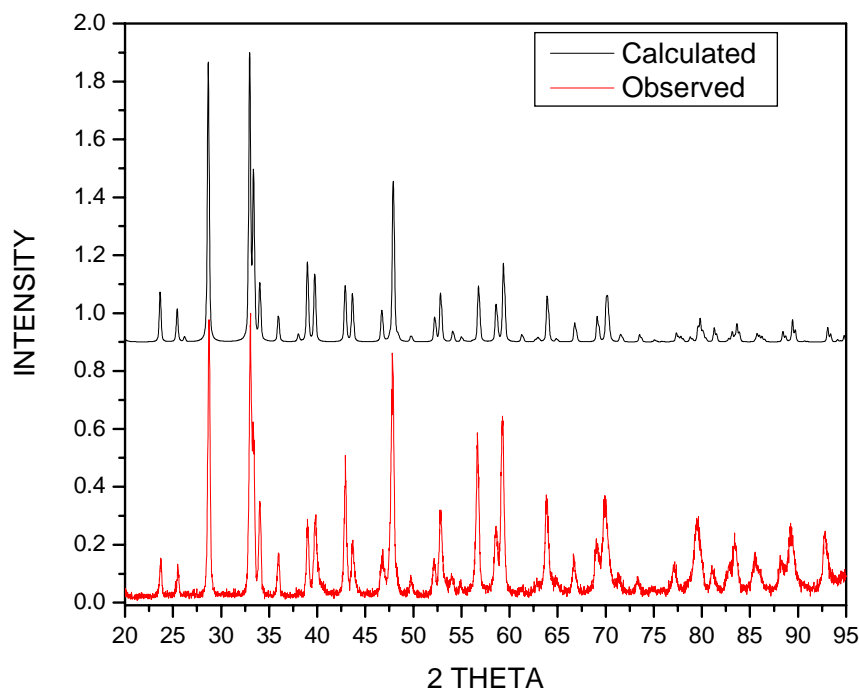


Figure A.3.2. The observed versus calculated powder patterns for $\text{Fe}_{0.62}\text{La}_2\text{Ti}_3\text{O}_{10}$

A.3.3.3 Magnetic behavior

The magnetic data, ZFC/FC is presented in Figure A.3.3. The magnetic moment calculated based on the linear fit is $5.2 \mu_B$, which is consistent with $\text{Fe}^{2+} (d^6)$.^[3] The Weiss constant is $\theta = 190 \text{ K}$, and this indicates strong ferromagnetic interactions between the magnetic ions. A transition occurs at low temperatures, at 20 K, where the two curves, ZFC/FC split. Also below this transition, there is a hysteresis loop, at 7 K. The hysteresis loop for $\text{Fe}_{0.62}\text{La}_2\text{Ti}_3\text{O}_{10}$ is presented in Figure A.3.4. This is also an indication of ferromagnetic exchange between the Fe^{2+} ions.

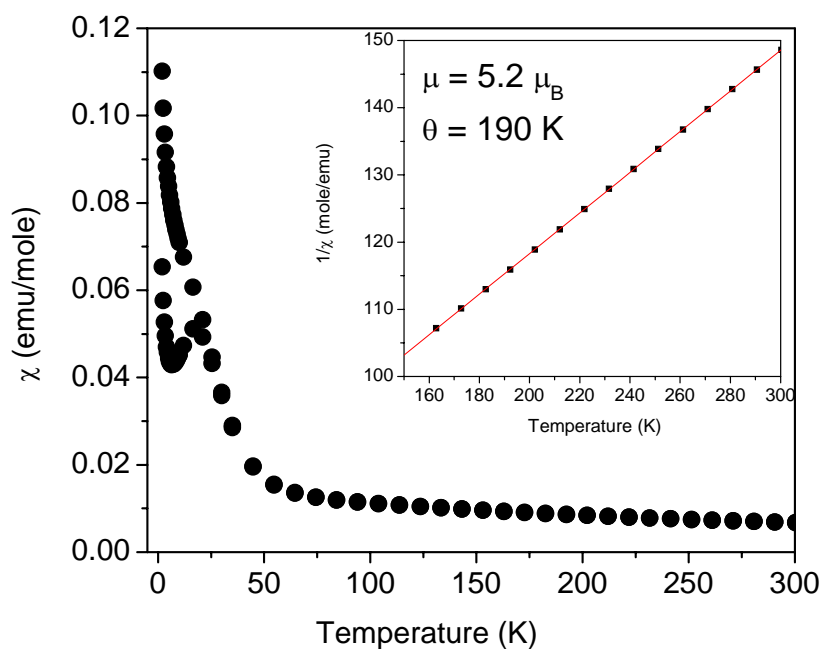


Figure A.3.3. Susceptibility versus temperature for $\text{Fe}_{0.62}\text{La}_2\text{Ti}_3\text{O}_{10}$. The inset shows the reciprocal susceptibility versus temperature with the linear fit from which a magnetic moment and a Weiss constant were extracted.

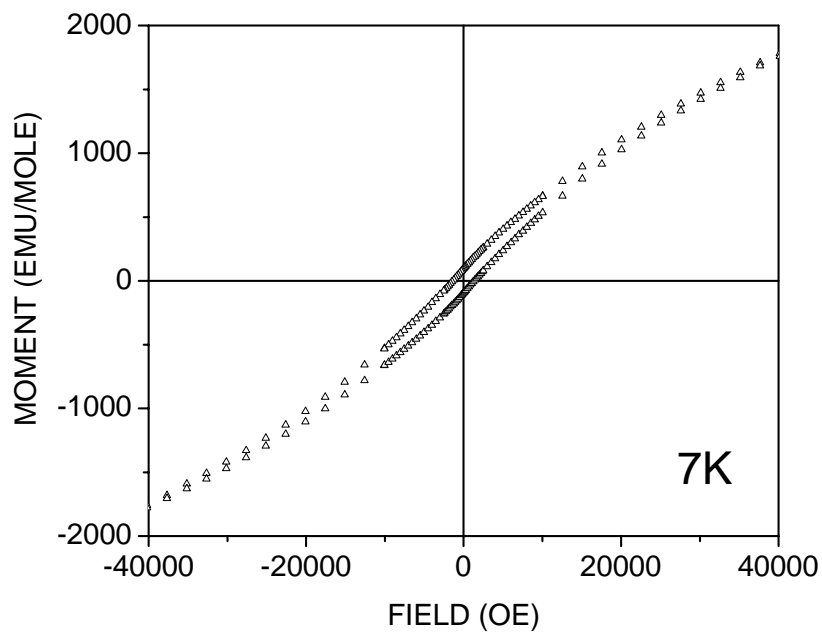


Figure A.3.4. Hysteresis loop for $\text{Fe}_{0.62}\text{La}_2\text{Ti}_3\text{O}_{10}$ at 7K.

A.3.4 Discussion

The reaction to form $(\text{FeCl})\text{La}_2\text{Ti}_3\text{O}_{10}$ does not occur. Elemental analysis and magnetic data are consistent with $\text{Fe}_{0.62}\text{La}_2\text{Ti}_3\text{O}_{10}$. It is known that trihalides of first row transition metals are not stable towards their dihalide counterparts.^[3] In vacuum conditions, it is reasonable to assume that iron trichloride decomposed to the dichloride and released chlorine gas.^[3] Upon ion exchange, the layered structure of the parent is maintained, with a contraction of the cell along the c axis. The magnetic behavior of this compound suggests ferromagnetic interactions going on below 25 K. The magnetic moment is in agreement with Fe^{2+} not with Fe^{3+} .

It would be interesting to do the same reaction with FeCl_2 to see if the same results are obtained. Byeon *et al.*, tried this reaction using an eutectic mixture $\text{KCl} + \text{FeCl}_2$, and they claim to have seen iron oxide impurities in the sample.^[4]

A.3.5 References

- [1] a) Kodenkandath, T. A.; Lalena, J. N.; Zhou, W. L.; Falster, A. U.; Carpenter, E. E.; Sangrerio, C.; Simmons, W. B., O'Connor, C. J. and Wiley, J. B *J. Am. Chem. Soc.* **1999**, *121*, 46; b) Viciu, L.; Golub, V. O.; Wiley, J. B. *J. Solid State Chemistry* **2003**, *175*, 88; c) Viciu, L.; Koenig, J.; Spinu, L.; Zhou, W. L.; Wiley, J. B. *Chem. Mater.* **2003**, *7*, 1480.
- [2] Toda, K.; Watanabe, J.; Sato, M., *Mat. Res. Bul.* **1996** *31*, 1427.
- [3] R. Colton and J. H. Canterford, *Halides of Transition Elements*, Wiley – Interscience, John Wiley & Sons Ltd., **1969**.

[4] Hyeon, K. A. and Byeon, S. H., *Chem. Mater.* **1999**, *11*, 352.

Vita

The author was born in Vasilati, Calarasi District, Romania in November 1972. She graduated from “Dante Alighieri” high school, Bucharest, in June 1990. In 1990, she began an undergraduate major in brewery. In 1992, she began undergraduate study in Physics and Physical Chemistry at the University of Bucharest, Romania. She received her BS degree in 1997, and joined the MS program at the same University. While completing her MS degree, she worked in a pesticide control facility. She received her MS degree in 1998, and was hired as a researcher at the Institute of Physical Chemistry in the Romanian Academy, where she worked in Prof. Speranta Tanasescu’s Thermodynamics Laboratory. In the summer of 1999, she went to the Technical University of Denmark, Copenhagen, for a PhD Summer School for the Petroleum Industry. In the fall of 2000, she came to the University of New Orleans, and in the spring of 2001 joined Professor John B. Wiley’s Research Group.